CRANFIELD UNIVERSITY

CRANFIELD HEALTH

PhD THESIS

Academic Year 2004-2008

Milena Varejka

Reconfigurable microfluidic platform in ice

Supervisors:

Sergey Piletsky

Igor Meglinsky

Anthony Turner

April 2008

. Abstract

Microfluidic devices are popular tools in the biotechnology industry where they provide smaller reagent requirements, high speed of analysis and the possibility for automation.

The aim of the project is to make a flexible biocompatible microfluidic platform adapted to different specific applications, mainly analytical and separations which parameters and configuration can be changed multiple times by changing corresponding computer programme. The current project has been supported by Vice Chancellor Trans-Campus Iinitiative.

Channels and various design geometries can easily and rapidly be marked on ice with a CO_2 laser. Within seconds a microchannel pattern of features as small as 100 µm were obtained. The channels and design cavity dimensions are governed by the ratio of laser power by the beam velocity. The channels created in ice stay open for a duration which depend on their geometry and therefore on the ratio of the laser beam power by the beam velocity. Microchannels were created with a power/velocity ratio between 0.4 and 20 W/m. In this range of settings, the channels were 300 µm wide and stayed open for 2 s. After that they refreeze and the micropattern disappears in the ice bulk.

Transport inside the channel can be obtained by the laser marking process alone. It is caused by the sheer surface tension within the melted area because of the temperature gradient within. The transport observed inside the channels was of the order of 1 mm/s in the laser experimental conditions (1.25 W and 100 mm/s). The temperature increase in the channel depends on the ratio of the laser power over velocity. High temperatures above 50°C can be achieved inside ice cavities. The experimental data were compared to theoretical values of the cavities dimensions and temperatures.

A valve adapted for a microfluidic in ice functioning upon freezing/melting promoted by laser scanning was tested. The opening of the area depends only on the power and the speed of the laser while the closing time by freezing depends on the cooler devices set temperature. A laser-assisted zone melting technique for the preconcentration of analytes demonstrated on Meldola's Blue as a model analyte was performed. A travelling melting zone of 1.5 mm x 1.5 mm was scanned at 6% power and 150 mm/sec with 25 scans over an area of 7.5 mm x 1.5 mm. An increase in concentration in end part of the melting zone was monitored after three successive travels.

Channels created in conductive frozen solution can be conductive if linked to an electrical power supply. Electrophoresic transport and electroseparation of Rhodamine B and Bromocresol Green in ice capillaries were demonstrated for analytes separation with a power supply (electrical conditions 100 V, 0.1 mA and 3 W).

The experimental results were in agreement with theoretical modelling and provide proof for the feasibility of the proposed concept of reconfigurable microfluidic device developed in ice and supported by scanning computer-controlled IR laser.

. Acknowledgements

I am extremely thankful for the opportunity I had in doing this PhD in Silsoe. I would like to thank all the people who have helped me on this specific project and I would particularly like to thank my supervisor Sergey Piletsky, without whom this whole experience would not have been possible, for his patience and of course his very nice meals.

I am now very much looking forward to my next adventure in life but whatever I do I will always remember those days in Silsoe.

. Table of Contents

. ABSTRACT I

. ACKNOWLEDGEMENTS III

. TABLE OF CONTENTS IV

. LIST OF FIGURES VII

. LIST OF TABLES XIV

. NOMENCLATURE XV

1. OUTLINE 1

2. LITERATURE REVIEW 3

2.1. MICROFLUIDICS 3

2.1.1. Definition 3

2.1.2. Fluid flow in microfluid devices 3

2.1.3. Historical background of the development of microfluidic systems 4

2.1.4. Applications, advantages and disadvantages of microfluidic devices 5

2.1.5. Components of microfluidic devices 6

2.1.6. Materials used in microsystems fabrication 13

2.1.7. Techniques used to fabricate microfluidics 15

2.2. ORDINARY WATER ICE 23

2.2.1. Water 23

2.2.2. Hydrogen bonding and proton ordering. 23

2.2.3. Water crystallisation 24

2.2.4. Hexagonal Ice (Ice Ih) 26

2.2.5. Cubic ice (Ice Ic) 27

2.3. AIM AND OBJECTIVES 28

3. MARKING OF OPEN CHANNELS IN ICE WITH A CO_2 LASER 29

3.1. LASER USES ON ICE IN THE LITERATURE 29

3.2. LASER-ICE INTERACTIONS 31
3.2.1. Marking of open channels *32*
3.2.2. Marking of closed channels/cavities *43*
3.3. METHODS 47
3.3.1. The freezing unit *47*
3.3.2. Freezing of samples *48*
3.3.3. Set up for marking channels *50*
3.3.4. Transport of liquid inside open channels *52*
3.3.5. Temperature and resistance measurements *54*
3.4. RESULTS 56
3.4.1. The freezing unit *56*
3.4.2. Freezing of samples *57*
3.4.3. Laser marking on ice *58*
3.4.4. Transport of liquid inside open channels. *62*
3.4.5. Temperature measurements *65*
3.4.6. Measures of the electrical resistance between two electrodes frozen in a conductive solution while scanning channels across them. *75*
3.4.7. Glass failure *80*
3.5. CONCLUSIONS 82
4. CREATION OF A MICROFLUIDIC DEVICE IN ICE 85
4.1. INTRODUCTION 85
4.2. LITERATURE 85
4.2.1. Opening of a valve made of ice *85*
4.2.2. Preconcentration *86*
4.3. METHODS 87
4.3.1. Opening of a valve made of ice *87*
4.3.2. Spectroscopy detection of a dye in ice capillaries *89*
4.3.3. Preconcentration *91*
4.4. RESULTS AND DISCUSSION 92
4.4.1. Opening of a valve made of ice *92*

4.4.2. Spectrophotometry 95
4.4.3. Preconcentration 99
4.5. CONCLUSIONS 102

5. ELECTROPHORESIS IN CHANNELS IN ICE 103

5.1. LITERATURE REVIEW 103
5.1.1. Electrophoresis separation 104
5.1.2. CE on microchips 105
5.1.3. Instrumentation 106
5.1.4. Ice as a separation substrate 108
5.2. MATERIALS AND METHODS 108
5.2.1. Capillary T-junctions in Perspex 110
5.2.2. Cassettes 111
5.2.3. Gels, polymer and solution frozen inside the cassettes 115
5.2.4. Dye electrophoresis 117
5.2.5. Dye separation 118
5.2.6. Separation in channels created by laser (no current applied) 121
5.3. RESULTS 121
5.3.1. Cassettes 121
5.3.2. T-junction 123
5.3.3. Electrophoresis in various frozen media 129
5.3.4. Dye electrophoresis 131
5.3.5. Dye separation 133
5.3.6. Mixture of dye separation 135
5.3.7. Long path channel 136
5.3.8. Mobility of dye in the channel when no current was applied 137
5.4. CONCLUSION 138

6. CONCLUSIONS AND SUGGESTIONS FOR FUTURE WORK 139

7. REFERENCES 141

. List of Figures

Figure 1: Principe of a valve-less diffuser pump. Diffuser/nozzle elements make the overall flow unidirectional (Olssen *et al.*, 1995). 8

Figure 2: EHD pump driven by induction pumping relying on a conductivity gradient and an electric field. 11

Figure 3: Electoosmotic flow: an externally applied electrical field causes motion of counter ions accumulated at the negatively-charged channel surface, dragging the bulk fluid. 13

Figure 4: The photolithographic process 16

Figure 5: Isotropic etching (left) and anisotropic etching (right) 17

Figure 6: Micromoulding in capillaries. A PDMS mould is placed on a substrate forming a network of microchannels in which a precursor in injected. After curing and removal of the PDMS, the microchannel structure is created on the substrate. 18

Figure 7: Microtransfer moulding: a prepolymer is poured into a PDMS mould which is then placed on top of a substrate. After curing and removal of the PDMS a microchannel structure remains on the substrate. 19

Figure 8: Solvent assisted micromoulding: A thin film of polymer is coated onto a substrate. A solvent-coated PDMS mould is then brought into contact with the polymer. After dissolution of the polymer by the solvent and removal of the mould, the microstructure is created in the polymer as a raised pattern. 20

Figure 9: Replica moulding: a PDMS mould is filled with a polymeric precursor. After curing the polymer is separated from the mould showing the microchannel structure.. 21

Figure 10: Proton-ordered (left) and proton-disordered (right) networks of water molecules. Hydrogen = blue), oxygen = red, bonds within a water molecule = violet, hydrogen bonds = light blue. 24

Figure 11: Phase diagram showing the various forms of ice existing over a range of pressures and temperatures. 25

Figure 12: The structure of hexagonal ice, Ih. The sets of layers are numbered 1 and 2 with darker colours towards the rear of the structure. Red lines show O-H-O links. 26

Figure 13: Top view of the Ice Ih structure. Red dots on some atoms mark a B layer with O-H-O links pointing up to the next B layer. Other atoms are in an A layer and have O-H-O links pointing down to the next A layer. 27

Figure 14: Cubic ice structure 28

Figure 15: Reflection, absorption and transmission of the laser irradiation by a material. A part of the incident radiation is reflected from the surface of the material, a part is absorbed by the material and the remainder passes through the material as the transmitted beam. 33

Figure 16: Left: marking of a linear object. The laser follows the contour of the object. Right: marking of a filled object. The laser follows lines inside the object. Arrows show the direction of the laser. 36

Figure 17: Schematic view of the marking of a channel on ice. The moving laser beam heats the ice creating a channel 37

Figure 18: Cross sectional area of a channel marked in ice with the laser beam 37

Figure 19: Forces acting on the melted area created by the laser beam (Steen, 2005) .. 42

Figure 20: Schematic view of the laser beam passing through a cover glass slide. 43

Figure 21: Heat flow (in red) through the glass slide from the glass surface heated by the laser towards the ice. 44

Figure 22: Schematic view of the laser scanning system 51

Figure 23: Set up for the marking of channels on ice with a computer assisted CO_2 laser. 53

Figure 24: Marking of a channel between a reservoir filled with Meldola's blue and an empty reservoir. The laser drags the dye in the channel towards the empty reservoir. 53

Figure 25: A thermocouple is frozen inside the ice for temperature measurements. 54

Figure 26: Circuit for the measurement of the electrical resistance in the channels drawn on the frozen solution... 56

Figure 27: The change in resistance of a 10 mM HCl solution upon freezing for a cooler device at three different set temperatures (-10, -15 and -20 ºC). 57

Figure 28: Channels marked with a CO_2 laser beam at 3% of total power and a 5 mm/s velocity (5 scans). 59

Figure 29: Cavities of decreasing diameters (from 1.5 to 0.3 mm) marked with a CO_2 laser beam at 4 % total power and a 100 mm/s velocity (25 times) using a spot marking style... 61

Figure 30: Pattern scanned in the ice with CO_2 laser beam of 100 mm/s velocity. 5mm long channels: 3% of total power (20 scans), 0.5 mm diameter dots: 1% of total power (10000 scans). 61

Figure 31: Microchannels formed in ice by repetitive scanning: empty channels (top) and filled with dye solution (bottom) marked with a laser beam at 5% and a 100 mm/s velocity (100 scans). 63

Figure 32: Temperature profile measured by a frozen thermocouple (black) and theoretical temperature profile (blue) following a single scan of one channel marked by a CO_2 laser beam at 100 mm/s and 6 % of total power. 66

Figure 33: Peak temperatures reached after a single channel was marked with 10 scans at 100 mm/sec over a range of laser power from 4 to 20% (laser Intensity range from 10 to 50 J/m per scan) measured with a thermocouple compared to the theoretical temperature peak expected in the channel (pink) with standard error bars. 68

Figure 34: Temperature increase measured by a frozen thermocouple upon continuous scanning of ten adjusted channels scanned on the ice surface under which the thermocouple is frozen. Scans were made with a CO_2 laser beam of 100 mm/s velocity and at 2, 3, 4, 5 and 6% total power (intensities of 5, 7.5, 10, 12.5 and 15 J/m). 69

Figure 35: Continuous scanning of a square area of 6 mm × 6 mm with a CO_2 laser beam at 100 mm/sec and 3, 4, 5 and 6 % power (intensities from 7.5, 10, 12.5 and 15 W/m) 71

Figure 36: Temperature changes measured by a frozen thermocouple following a single scan of one channel marked by a CO_2 laser beam at 100 mm/s and 10 % of total power.. 72

Figure 37: Temperature increase measured by a frozen thermocouple upon continuous scanning of ten adjusted channel scanned in ice covered with a cover glass. The CO_2 laser beam velocity was 100 mm/s and its power was set at 5, 10 and 15% total power (standard error bars). 74

Figure 38: Variation of resistance of ice while scanning 15 channels, 1 scan each, with a CO_2 laser beam at 100 mm/s and at 4, 5, 6 and 7% power: intensities:10, 12.5, 15 and 17.5 J/m and standard deviation of up to 500 Ω. 76

Figure 39: Variation in the electrical resistance of ice (ΔR) when a channel was marked with a laser beam at 100 mm/s and 3 and 4% of total power (intensities of 7.5 J/m and 10 J/m) every 30 s for 5min. 78

Figure 40: Variation of resistance of ice while scanning 15 channels, 1 scan each, with a CO_2 laser beam at 100 mm/s and at 5, 10 and 15% power: intensities: 12.5, 25 and 37.5 J/m. Standard deviation of up to 500 Ω. 80

Figure 41: Melting of a 1 mm ice area between two channels. 88

Figure 42: Spectrophotometer set up. 89

Figure 43: Illumination of a 2 mm diameter area by the laser beam upon freezing of the surrounding area... 91

Figure 44: Schematic diagram of the progression of the molten zone in the sample by laser illumination. 92

Figure 45: Melting time of a 1mm wide ice section separating two channels with standard deviation bars. 93

Figure 46: Laser power versus the inverse of the time of opening. 94

Figure 47: Absorbance calibration for Meldola's Blue solutions (at 570 nm) performed using Qmicro-R200-7-UV/VIS-BX reflection probe and the USB2000 spectrophotometer. 96

Figure 48: Absorbance of Meldola's Blue dye drops inside channels marked in ice at 570 nm. Measurements were performed with the Qmicro-R200-7-UV/VIS-BX reflection probe and the USB2000 spectrophotometer. 97

Figure 49: Changes in ice absorbance at 570 nm during freezing. 98

Figure 50: Linear expansion measured during freezing of water inside dishes............ 99

Figure 51: Change in concentration of dye in the melted area during freezing of the surrounding zone (standard deviation bars).. 100

Figure 52: Experimental (squares) with standard deviation bars and theoretical (pink) concentrations of dye in the final part of the travelling melting zone after 1, 2 and 3 cycles in ice... 101

Figure 53: Schematic view of an electrophoretic separation system on a micro-chip. 107

Figure 54: Design of the millimetre T-junction using Winmark software 110

Figure 55: Design of the micro capillary T-junction using Winmark software........... 111

Figure 56: Schematic representation (top view) of Cassette A.................................. 112

Figure 57: Schematic representation of the Cassette B 113

Figure 58: Design of Cassette C mould using Winmark software.............................. 114

Figure 59: Schematic representation of Cassette C 115

Figure 60: Electrophoresis design.. 118

Figure 61: Experimental set-up for dye electrophoresis... 119

Figure 62: Long path separation channels 120

Figure 63: Experimental set-up for long path separation.. 120

Figure 64: Rhodamine B structure.. 124

Figure 65: T-Junction drilled in Perspex 124

Figure 66: Injection of Rhodamine B dye.. 125

Figure 67: After application of a voltage between the electrodes the dye moves to the cathode.. 125

Figure 68: Capillary T-junction in Perspex. 126

Figure 69: Injection of Rhodamine B into the dye channel.. 127

Figure 70: After appliance of voltage between the electrodes the dye moves to the anode. 127

Figure 71: Sequence of pictures taken with a CCD camera under the illumination of a UV lamp showing the flow of Rhodamine B in the microcapillary junction when a voltage of 500 V was applied between the electrodes. 128

Figure 72: Changes is current passing through the channels created in frozen HCl frozen solution, at 50 V, when 5 channels were scanned (150 mm/s, 8 %, 50 scans). 129

Figure 73: Meldola's Blue structure 132

Figure 74: Microfluidic set up created for investigation of mobility of Meldola’s Blue in ice capillaries scanned by the laser (8 %, 150 mm/s, 50 scans) 132

Figure 75: Rhodamine B load 133

Figure 76: Flow of Rhodamine B inside the separation channel. Image made after letting the channel freeze for 1 minute. 134

Figure 77: Electrophoresis result when the separation channel was scanned in both directions. 134

Figure 78: Electroseparation of Rhodamine B and Bromocresol Green. 135

Figure 79: Bromocresol Green structure 136

Figure 80: Successive images taken with a CCD camera in the dark under the illumination of a UV light during the scanning of an S-shaped channel in which Rhodamine B flows 137

. List of Tables

Table 1: Comparison between the theoretical average maximum temperatures reached when 10 channels 2 cm long were scanned continuously with a laser power of 3, 4, 5 and 6%. 70

Table 2: Volume and time of freezing of Cassettes A, B and C 122

. Nomenclature

AMPSA	Acrylamidomethylpropansulfuric Acid
APS	Ammonium Persulphate
CCD	Charge-Coupled Device
CE	Capillary Electrophoresis
CD	Compact Disc
DNA	Deoxyribonucleic Acid
dNTP	Deoxynucleoside Triphosphate
EHD	Electrohydrodynamic
EDTA	Etylenediaminetetraacetic Acid
EOF	Electroosmotic Flow
HCl	hydrochloric acid
IR	Infrared
LB	Luria-Bertani
MAA	Metacrylate Acid Acrylamide
µTAS	Miniaturized Total Analysis System
PEEK	Polyaryletheretherketone
PCR	Polymerase Chain Reaction
PDMS	Poly(dimethylsiloxane)
PZT	Lead Zirconate Titanate
TEMED	NNNN Tetramethylethylendiamine
TAE	Tris-glacial Acetic acid-EDTA
USB	Universal Serial Bus
UV	Ultraviolet

1. Outline

Microelectronic integrated circuit chips technology has been applied to miniaturised analysis devices for various biological applications since 1990. Research has developed state of the art micromachining and microelectromechanical fabrication technologies for efficient microfluidic devices. Those techniques however usually do not make reconfigurable devices while industrial design of new applications would beneficite from reconfigurability of the devices.

The aim of the project is to make a flexible biocompatible microfluidic platform adapted to different specific applications which parameters and configuration can be changed multiple times by changing corresponding computer programme.

In a novel approach, this microfluidic platform was made in ice with a software controlled CO_2 laser. This thesis presents the work that has been done to develop this new, challenging but promising platform.

The thesis starts with a review on conventional microfluidic devices and the techniques used for their fabrication and follows with discussion of ice properties which make them suitable for application in reconfigurable microfluidic devices. The experiments describe freezing and laser processing of ice during the marking of simple geometries in ice. The relation between the laser parameters and the dimensions of the created channels marked, the temperature reached inside the geometries and the time of opening and closing are presented. Work follows with study of the transport properties in the ice channels.

In chapter 2 complimentary technology related to the creation of valves in ice is presented. Here we describe valve functioning upon freezing/melting promoted by laser scanning. We also discuss in chapter 2 use of laser-assisted zone melting technique for the preconcentration of analytes.

Freezing can be applied also for immobilisation of biological molecules and even cells which can be used for separation and development of assays.

Chapter 4 presents the application of ice microfluidic platform in capillary electrophoresis.

2. Literature review

2.1. Microfluidics

2.1.1. Definition

The demand for smaller and increasingly integrated microsystems, also called micro total analysis systems (µTAS) or "labs on a chip" has been growing over recent decades. Microfluidic devices are one large area of investigation of microsystems.

By definition, microfluidic devices handle fluids in microlitre amounts. Typical dimensions are within 1 to 5 cm^2 for a microfluidic chip, 10 to 100 mm for he width of a microchannel and 0.01 to 10 mL for volumes handled (Whitesides, 2006).

2.1.2. Fluid flow in microfluid devices

The fluid flow regime depends on the Reynolds number, Re, which is the ratio of the inertial forces to the viscous forces:

$$\mathrm{Re} = \frac{\rho v d}{\mu} \qquad \textbf{Equation 1}$$

where ρ is the density of the fluid (kg/m^3), v is the mean fluid velocity (m/s), d is the channel diameter and μ the dynamic viscosity of the channel ($N.s/m^2$). When Re << 1, the flow is laminar and very smooth. When Re > 10^3, the flow is turbulent and mainly characterised by vortices (Kundu, 2007).

Flow within microstructures typically have Reynolds numbers of 10^{-3} to 10^{-5} and are characterised by a laminar flow. Contrary to fluid dynamic in larger scales devices, in microfluidic devices viscous forces dominate, turbulence is non-existent.

Surface tension can be an important driving force and mixing is slow and occurs through diffusion (Purcell, 1977). Mixing in short microchannels can be improved by various techniques such as through the application of external voltages (Aubry *et al*, 2004), ultrasonic waves (Yang *et al*, 1999), by slanted walls at a T intersection (Johnson *et al*, 2002) and the separation of the main fluid stream into smaller ones, altered so as to offer increased boundary surfaces (Koch *et al*, 1998), among other techniques.

2.1.3. Historical background of the development of microfluidic systems

The history of microfluidic device technology was reviewed by Reyes *et al.* (2002). The first microfluidic device was a miniaturised gas chromatograph developed at Stanford University in 1975, which used integrated circuit processing technology. It consisted of a 5 cm diameter silicon wafer with an open-tubular capillary column, two sample injection valves and a thermal conductivity detector. This device was the first step towards smaller, lighter and more portable devices. This gas chromatograph was able to separate a simple mixture of compounds in a matter of seconds (Terry *et al.*, 1979). Despite its good performances and its small size, no further research on miniaturised gas chromatographs was initiated until the 90s. However researchers investigated and developed micropumps, microvalves and microchemical sensors. Progress in molecular biology also stimulated the development of capillary electrophoresis for the separation and analysis of DNA and proteins, as well as other macromolecule mixtures. T-junctions were also created in the late 80s as the first capillary injection tools.

In 1990, Manz *et al.* presented a miniaturised open-tubular liquid chromatograph on a silicon wafer. Manz is also the creator of the novel concept of the micro total analysis system (μTAS). A μTAS contains pre-treatment, separation and detection devices all on one chip. He widely promoted μTAS as offering many components within a single chip of reduced size and since the first μTAS, new microfabrication processes, separation, detection and analysis methods have been developed and have found new applications.

2.1.4. Applications, advantages and disadvantages of microfluidic devices

Microfluidic devices have been used in fundamental research as well as in wide practical applications in biomedical science, genomics, forensics, toxicology, immunology, environmental studies, chemistry or biochemistry). They can be used for rapid DNA sequencing (Woolley & Mathies, 1995), PCR (Waters *et al.* 1998), detection of pathogens (Abbott & Skaife, 2004) or environmental contaminants (Van den Berg *et al*., 1993), clinical analysis of blood (Lauks, 1998), sample preparation (Li & Harrisson, 1997), micro-scale organic synthesis (Konrad *et al*., 1997) or even in the development of biomimetic systems (Runyon *et al*., 2004), among other examples.

Microfluidic devices have widespread applications because of their many benefits. They are small, light, portable, have low manufacturing, usage and disposal costs, analysis times are reduced, as are he consumption of reagents and analytes, smaller sample volumes limit the exposure of the operators to biohazardous samples and higher separation efficiencies are usually achieved. In addition, physiological studies are now possible thanks to microfluidic devices because they can reproduce *in* *vivo* capillaries sizes or microenvironment and allow studies which would be not otherwise be possible with normal scale devices, hence their wide applications in biochemistry, biology and medicine.

Microfluidic devices present few disadvantages, however their size can actually present some difficulties. Detection can be become more challenging, the devices are susceptible of blockages from particles and they are more sensitive to the adsorption of species on the surface of the capillaries.

2.1.5. Components of microfluidic devices

In a µTAS, the microfluidic unit is connected to a sampling unit, a detector unit and an electronic unit. The main components of the microfluidic unit are injectors, channels, pumps, valves, switches, reactors and storage containers.

Various types of valves and pumps are presented in the following sections.

2.1.5.1. Valves

As major fluid handling tools, valves are used in most microfluidic devices and have been the object of various studies. Micro valves offer various advantages over traditional valves: rapid response time, lower power consumption, smaller dead volume and improved fatigue properties (Gravesen *et al.*, 1993).

Van den Berg & Lammerink (1999) classified valves depending on the type and direction of the restriction made to the flow. In most valves the flow is stopped when a restriction is made to the channel. This restriction can either be perpendicular to the flow, parallel to the flow or a mixture of both. In a very different type of valve the flow is stopped by the formation of a frozen part inside the channel. The latter type does not require a moving part and avoids any leakage around the valve, which can occur in micromachined valves.

Micromachined valves can also be segregated in two categories: passive valves (or check valves), which do not require mechanical actuation and active valves, which do. Cantilever valves, diaphragm valves, diffuser/nozzle valves are typical passive valve types. Actuation of active valves is generally piezoelectric, thermopneumatic, electrostatic or electromagnetic (Koch & Ewans, 2000).

2.1.5.2. Micropumps

Transport in microfluidic devices can either be achieved due to passive mechanisms such as surface tension, by utilising valves or through pumping (Laser & Santiago, 2004**)**.

Two kinds of micropumps have been developed: mechanical micropumps and non-mechanical or continuous flow micropumps.

Most of the mechanical micropumps consist of a pressure chamber closed by a flexible diaphragm driven by an actuator and inlet and outlet valves. The fluid pumping process is generated by the 2-phase cycle of the moving diaphragm: during the supply phase of the pump cycle, fluid enters the pump chamber on underpressure through the inlet; during the pump phase, the fluid leaves the chamber on overpressure through the outlet valve. The inlet valve prevents unwanted flow in it's the reverse direction, so that the output flow is unidirectional. The outlet flow is generated in a series of discrete pulses, the volume of which depend on the diaphragm stroke volume during the pump cycle (Wois, 2004).

Most inlets and outlets valves of mechanical pumps are check valves. However pumps without valves (sometimes called diffuser pumps) have also been developed (Olssen *et al*., 1995) to avoid the risk of valves becoming blocked by small particles, resulting in pumping failure. They use flow rectifying diffuser/nozzle elements, which create a unidirectional flow, as depicted in Figure 1. Valve-less pumps are not sensitive to valve blocking and allow pumping of fluids containing small particles.

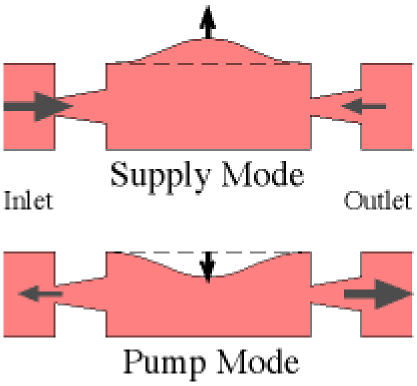

Figure 1: Principe of a valve-less diffuser pump. Diffuser/nozzle elements make the overall flow unidirectional (Olssen *et al.*, 1995).

There are four main types of actuation for mechanical micropumps. Piezoelectric actuation was used in the first micropump developed in the late 70s by Spencer (1978). But it was ten years later with Van Lintel *et al.* (1988) and Smits (1990) publications on piezoelectric actuations than research on micropumps really started. In piezoelectric actuation the valves and the pump diaphragm are coated with a piezoelectric material such as Lead Zirconate Titanate (PZT), which is readily available. Piezoelectric materials move when excited by an electrical current and induce the displacement of the pump diaphragm and valves. Piezoelectric actuation provides a comparatively high stroke volume and a fast mechanical response. However this requires a high voltage (minimum 100V) and the mounting procedure of the piezoelectric materials on the valves and the diaphragm can be problematic.

A second type of actuation, thermopneumatic actuation, was developed by Van de Pol *et al.* in 1990. The displacement of the pump diaphragm is generated by the extension of an air-filled chamber with an integrated resistive heater mounted on top of the diaphragm. The voltages used for thermopneumatic pumps are much lower than those used for piezoelectric actuation, making this pump much more adaptable to microfluidic devices containing electrochemical sensors.

More recently an electrostatically actuated pump has been developed by Zengerle *et al.* (1995). It is constructed of a capacitor, consisting of an electrode mounted on the pump diaphragm, which is electrostatically attracted to a fixed counter electrode when high voltage is applied between the pair of electrodes. When the capacitor discharges, the diaphragm returns to its initial position. The capacitance between the pump diaphragm and a counterelectrode of the same diameter, d, separated by a distance s, is:

$$C = \frac{\varepsilon \pi d^2}{4s}$$ **Equation 2**

Although the pump diaphragm typically bows during the pump operation, the generated force during electrostatic actuation is proportional to the square of the applied voltage and inversely proportional to the square of the distance between the electrodes. At the beginning of pump operation, when the electrodes are parallel, the electrostatic force between the two electrodes is:

$$F = \frac{1}{2}\frac{\partial C}{\partial s}V^2 = -\frac{\varepsilon \pi d^2}{8s^2}V^2$$ **Equation 3**

where ε is the permittivity of the medium separating the electrodes and V the potential difference between them (Griffiths, 1999). Electrostatically actuated pumps can achieve a higher output frequency than piezoelectric and thermopneumatic actuated pumps, which results in a smoother flow. However they require high voltages (200V) and achieve small actuator strokes compared to piezoelectric and thermopneumatic pumps (Judy *et al*, 1991; Bourouina *et al*, 1997).

Micropumps using electromagnetic actuation have also been made, although more rarely (Dario *et al.*, 1995). A permanent magnet is attached to the pump diaphragm and is moved by an external coil, causing the pump diaphragm displacement. Voltage requirements are comparable to those of thermopneumatic actuators, however electromagnetic actuation offers a slightly faster mechanical response.

A second type of micropump, which does not require mechanical moving parts, has been developed. Unlike mechanical pumps, continuous flow micropumps provide a steady output flow. Their use and performance can however be limited by the properties of the pumped fluid, such that, in most cases, gas transport is not possible.

The mode of operation of electrohydrodynamic pumps relies on the interaction of electrostatic forces with ions in a dielectric fluid. The electric force, Fe, that results from an applied electric field E, is given by:

$$Fe = qE + P.\nabla E - \frac{1}{2}E^2\nabla\varepsilon + \frac{1}{2}\nabla\left[E^2\left(\frac{\partial\varepsilon}{\partial\rho}\right)_T\rho\right] \qquad \textbf{Equation 4}$$

where q is the charge density, ε the fluid permittivity, ρ the fluid density, T the fluid temperature and P the polarization vector (Melcher, 1981). One type of electrohydrodynamic (EHD) micropump was developed by Richter *et al.*, in 1991. It consisted of two gold electrodes mounted on silicon chips placed into a channel. Ions were injected from the electrodes to the fluid when a high voltage was applied between the electrodes. The ions migrated in the electric field, which induced fluid transport. The mode of operation of this type of pump relies on the injection of ions, which generally takes place at a metal/liquid interface and involves the electrochemical formation and movement of charged particles. Another type of EHD pump (see Figure 2) relies on inductive pumping (Bart *et al.*, 1990), where charges are induced at a fluid-fluid or fluid-solid boundary layer in the electric field, due to a non-uniformity in the electrical conductivity of the fluid. The latter can be caused by a non-uniform temperature distribution or the non-homogeneity of the fluid, e.g. two phase fluid.

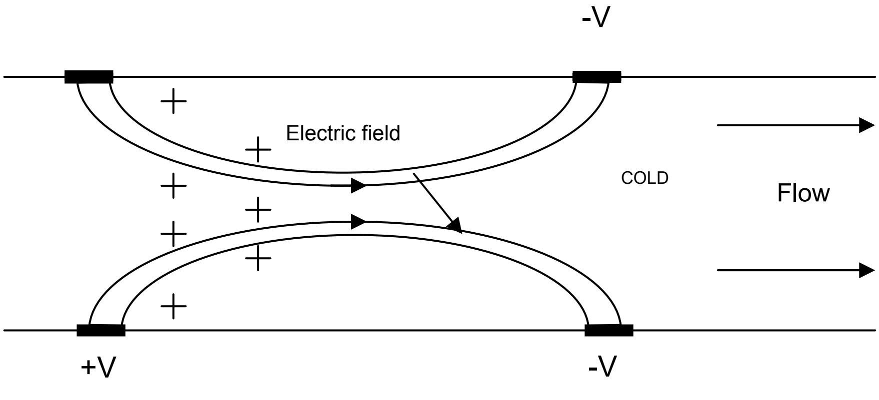

Figure 2: EHD pump driven by induction pumping relying on a conductivity gradient and an electric field.

The use of EHD pumps is strictly limited by the ionisation process (which depends on the electrode composition) the fluid electrical properties and the voltage applied.

Electroosmotic force micropumps rely on the presence of immobile surface charges in glass capillaries. At neutral pH, the surface of glass (silicate groups) is negatively charged and attracts mobile, positively-charged counterions, present in the fluid, forming an electrical double layer. The thickness of the double layer is the Debye shielding length, λ_D of the fluid, given by:

$$\lambda_D = \sqrt{\frac{\varepsilon k T}{q^2 \sum_i z_i n_{\infty,i}}}$$

Equation 5

where ε is the permittivity of the fluid, T the temperature of the fluid, z_i the valence number, n the number density of the ionic species, i, in solution, k the Boltzmann constant and q the electron charge. When an electric field is applied parallel to the channels a portion of the mobile counterions in the liquid phase of the electric double layer can be set into motion and induce the overall fluid flow (Adamson & Gast, 1997). During electroosmotic pumping, dispersion is minimised and the fluid typically shows a very flat velocity profile (Scales & Tail, 2004). Basic electroosmotic pumps consist of microchannels and electrodes submerged within reservoirs located at the ends of the channels (Dasgupta & Liu, 1994; McKnight *et al.*, 2001).

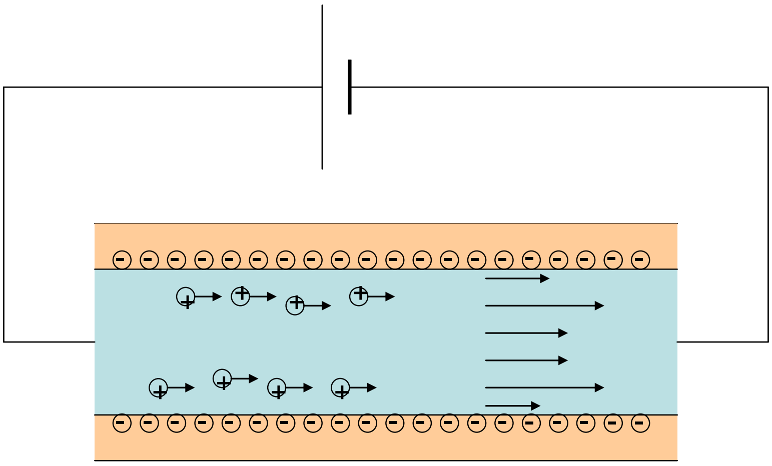

Figure 3: Electoosmotic flow: an externally applied electrical field causes motion of counter ions accumulated at the negatively-charged channel surface, dragging the bulk fluid.

2.1.6. Materials used in microsystems fabrication

A wide range of materials have been used for the fabrication of microfluidic systems (Qin *et al.,* 1999). The first microfluidic devices were made in silicon and glass, since microfluidics fabrication techniques derived from technology used within the microelectronics industry (Manz *et al*, 1991). Silicon is chemically and thermally stable and channels can be fabricated in this material by etching or photolithography. However silcon wafers are expensive, brittle and opaque in the UV and visible regions and is therefore not suitable for devices relying on optical sensors for detection (Shoji & Eshasi, 1994). Glass was an early replacement for silicon, being less expensive, transparent, negatively charged, and a good support for electroosmotic flow (Yao *et al*., 2003). Glass wafers are available in different composition and sizes. Fused silica wafers, made of pure amorphous silicon dioxide, can withstand high temperatures and have very low autofluoresence. Borosilicate wafers (such as Pyrex) are less expensive than fused silica but cannot be exposed to high temperatures and have higher autofluoresence (Stjernstrom & Roeraade, 1998). Both silicon and glass processing require high voltages and temperatures as well as a cleanroom environment. Manufacturers of commercial mass production microfluidic devices looked for easier and cheaper alternatives.

Polymers are inexpensive which allows for the manufacture of disposable devices. They also offer interesting properties for microfluidic devices. Rigid elastomeric materials have good structural rigidity and strength and enable the fabrication of small and rigid microfluidic devices. Channels can be formed in polymers by moulding and various soft lithography processes and sealing of discrete parts can be achieved thermally or with adhesives. However, their surface chemistry is more complex than that of silicon or glass. They are often incompatible with organic solvents and generally cannot be used at high temperatures (McDonald, 2000). The most popular polymers in which microfluidics can be fabricated are poly(methylmethacrylate) (Schulz *et al.*, 2000) polycarbonate (Shen & Lin, 2002) and poly(dimethylsiloxane) (PDMS) (McDonald *et al.*, 2000). PDMS can be easily and quickly moulded into a microfluidic device but suffers from limitations due to its chemistry (organic solvents and small organic analytes are not compatible with PDMS devices and can cause the polymer to dissolve), its elasticity (certain geometries cannot be maintained in PDMS), its low thermal conductivity (leading to heating in the device and high permeability to gases. PDMS is still ideal for a range of applications where the device needs to be bent or sealed to other materials and is also ideal for uses with aqueous fluids. Other interesting compounds are Teflon®-based polymers. They are inert to most solvents and chemicals and offer great potential for biomedical microfluidics when used with corrosive fluids (Lee *et al.*, 1998).

2.1.7. Techniques used to fabricate microfluidics

The first fabrication processes used for the manufacture of microfluidic devices derived from processes used in the microelectronics industry: the devices were fabricated by photolithography or by etching in silicon and glass. These techniques were expensive and time-consuming and were soon replaced by cheaper and quicker methods, such as laser ablation or injection moulding and soft lithography, which were made possible by the use of new materials such as polymers. The speed of fabrication, the size of the microfluidic device, its geometry and the components needing to be fabricated are the main aspects to be considered when choosing one or other technique.

2.1.7.1. Photolithography

The first microfluidic devices were fabricated by photolithography (Moreau, 1988). Developed for microelecronics, this method can be applied on silicon and glass to fabricate networks of channels. It consists of the exposure, through a suitable mask, of a surface coated with a sensitive photoresist, to ultraviolet light. The photoresist is modified by exposure to light and typically becomes soluble in a developer, whereas unexposed regions remain insoluble (negative-working resist). The developed regions are washed away leaving the pattern of the mask on the surface, as shown in Figure 4. This method enables good control over the shape and size of the patterns, which can be created simultaneously over an entire surface. Patterns smaller than 100 nm however cannot be formed. Photolithography also requires planar surfaces and extremely clean operating conditions (Brittain *et al*., 1998).

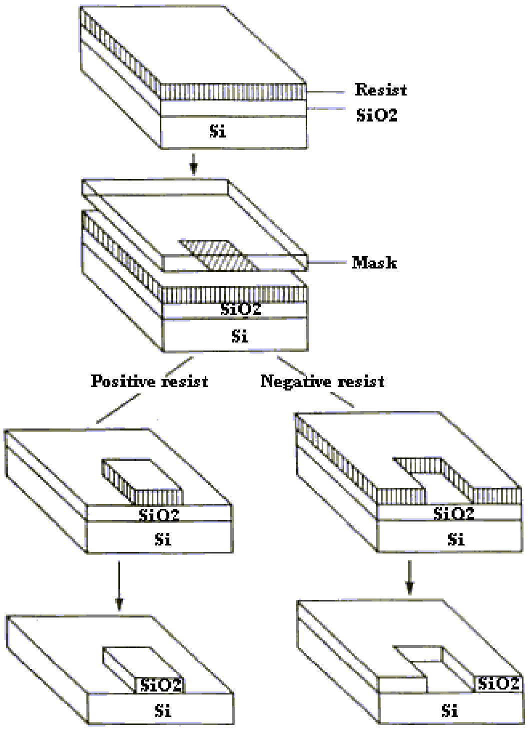

Figure 4: The photolithographic process

2.1.7.2. Etching techniques

Etching techniques derived from microelectronics technologies have also been used to fabricate microfluidics. They consist of exposing the surface, delimited by a pattern, to an etching solution (wet etching) or to high-energy ions (dry etching). Etching can be isotropic or anisotropic as shown in Figure 5. Isotropic etching etches in all directions equally; leading to undercutting and a rounded etch profile. Anisotropic etching is directional and is more common in dry etching.

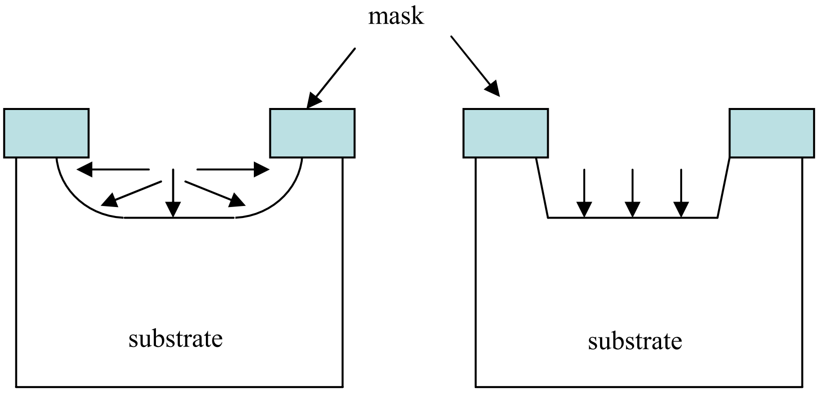

Figure 5: Isotropic etching (left) and anisotropic etching (right)

Wet etching requires minimal equipment. Silicon wet etching can be performed with solutions of hydrofluoric acid and nitric acid which results in an isotropic etch (Robbins & Schawarz, 1960) or with solutions of potassium hydroxide, tetramethylammonium hydroxide and ethylenediaminepyrocatechol, giving an anisotropic etch (Sze, 1988).

Dry etching is a more expensive technique but can give very deep and narrow structures. Xenon difluoride is a dry isotropic etchant of silicon (Chu *et al*, 1997).

2.1.7.3. Soft lithography

Soft lithography techniques were developed by Xia & Whitesides (1998) to allow the fabrication for smaller patterns These techniques rely on the use of elastomeric pattern-transfer elements, usually made of PDMS, hence their collective name of "soft lithography" methods. Unlike photolithography, these methods do not require a clean room when producing most patterns and can be used on curved surfaces (Brittain *et al.,* 1998). The next section gives a brief description of some soft lithography techniques.

Kim *et al*. (1995) developed micromoulding in capillaries, where a pattern-transfer element, fabricated in PDMS and containing a network of capillaries, was placed on the substrate and a polymeric precursor was injected at one end of the microchannels. The precursor was drawn into the channels by capillary action and then cured by heating or by exposure to UV radiation. The pattern-transfer element was then removed, leaving the newly-formed polymeric structure on the substrate, as shown in Figure 6.

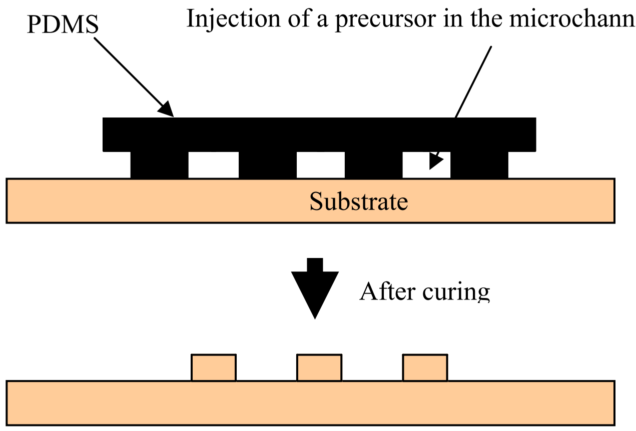

Figure 6: Micromoulding in capillaries. A PDMS mould is placed on a substrate forming a network of microchannels in which a precursor in injected. After curing and removal of the PDMS, the microchannel structure is created on the substrate.

Microtransfer moulding was first performed by Zhao *et al*., .1996. The technique consists in pouring a polymeric precursor into the pattern-transfer element, which is then placed on top of the substrate. The prepolymer is cured and when the pattern-transfer element is removed the polymeric structure remains on the substrate (see Figure 7).

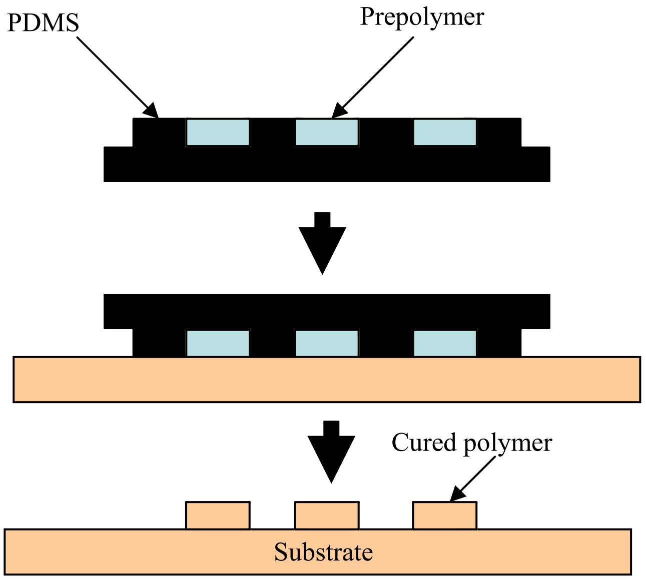

Figure 7: Microtransfer moulding: a prepolymer is poured into a PDMS mould which is then placed on top of a substrate. After curing and removal of the PDMS a microchannel structure remains on the substrate.

In solvent-assisted micromoulding (King *et a*l., 1995), the substrate surface is coated with a layer of polymer, while the pattern-transfer element is coated with a solvent which dissolves the polymer when the pattern-transfer element is placed on top of the substrate. The dissolved polymer flows and fills the pattern-transfer element. The pattern-transfer element is then removed, leaving the pattern on the substrate.

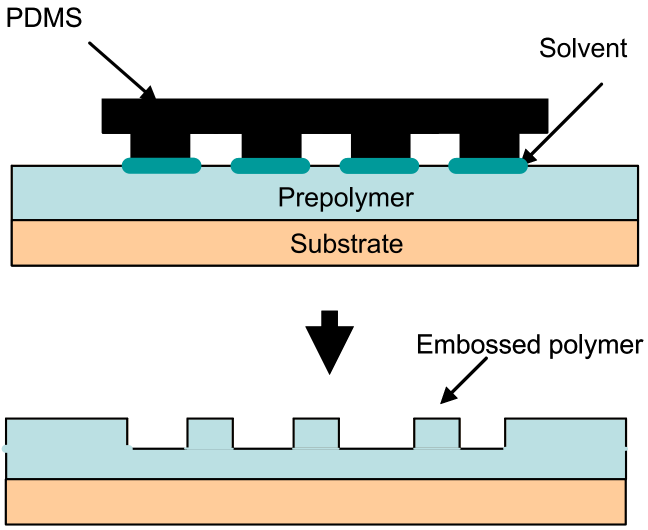

Figure 8: Solvent assisted micromoulding: A thin film of polymer is coated onto a substrate. A solvent-coated PDMS mould is then brought into contact with the polymer. After dissolution of the polymer by the solvent and removal of the mould, the microstructure is created in the polymer as a raised pattern.

In replica moulding (Xia *et al*, 1996), the pattern-transfer element is filled with a polymeric precursor such as polyurethane, which is cured by heating or irradiation with UV light and then separated from the mould. This results in the formation of a polymeric replica of the PDMS mould (see Figure 9).

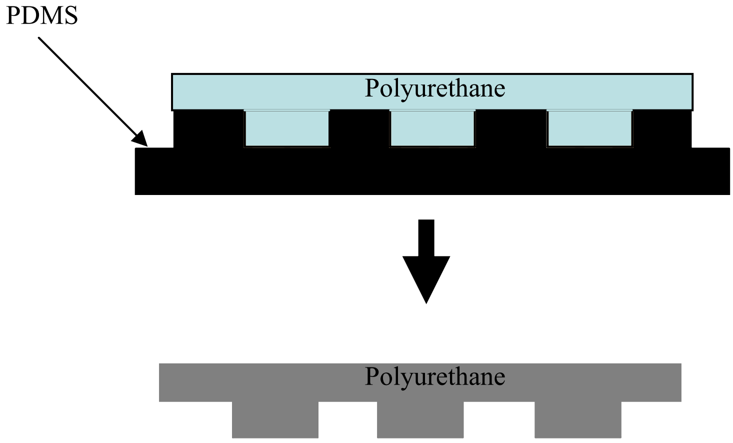

Figure 9: Replica moulding: a PDMS mould is filled with a polymeric precursor. After curing the polymer is separated from the mould showing the microchannel structure.

2.1.7.4. Hot embossing

Hot embossing is a low-cost technique that imprints microstructures in plastic materials. This is the widespread and commercially used technique to make CDs. It consists of pressing a heated thermoplastic film under pressure firmly into a mould in an evacuated chamber. The plastic fills the mould and replicates the microstructures. The set-up is then cooled and the plastic material is removed from the mould. Low flow rates ensure the replication of features as small as 25 nm (Heckele *et al.*, 1998).

2.1.7.5. Injection moulding

The macroscopic injection moulding process can also be adapted to the manufacture of microfluidic devices. This consists of injecting a polymer inside a mould cavity which is heated above the glass transition temperature of the polymer. The polymer fills the mould cavity, is cooled down and then removed from the mould. This technique can generate microstructures with features as small as 0.5 µm. It can also create fibre-reinforced metal components and those made of metal-ceramic compounds (Heckele & Schomburg, 2004).

2.1.7.6. Laser ablation

Laser ablation refers to the removal of material induced by a high energy laser beam. The phenomenon was first observed in 1973 (Emmony *et al.*). The beam breaks the covalent bonds between the substrate molecules and produces a shock wave which removes the decomposed materials (Roberts *et al.*, 1997). The emissions of the laser beam emitted can range from deep ultraviolet, as in the case of Excimer lasers, the wavelength range of which spans from 150 to 330 nm, to the infrared, as exemplified by the CO_2 laser, operating at a of wavelength 10600 nm. Polymers can also be doped with dyes that exhibit a peak in absorbance at the laser beam wavelength to enhance the efficiency of the ablation process.

Laser ablation is a rapid process. Microfluidic devices are created by tracking the focused laser beam over the substrate. This can be achieved either with a fixed laser and the substrate mounted on a x-y moving stage or with a fixed substrate and a x-y moving laser beam. The laser contains steering and imaging optics, such as mirrors, apertures and focusing lens, designed to direct and focus the beam onto the substrate surface. Dimensions as small as 6 µm, can be created in polymers, glass, ceramics and metal. The main parameters which determine the dimensions of the feature of the microfluidicdevice that can be created depend on the laser fluence (energy per unit area), the size of the focused laser spot, the scanning velocity, the number of repetitions and the nature of the substrate. If the laser fluence is too low, no ablation will occur. The number of repetitions and the scanning velocity affect the roughness and the depth of the ablated area. However the depth obtained is limited by the depth of focus of the laser, since the laser fluence decreases when the laser beam is out of focus. When deeper structures are needed, the focus should be readjusted between repetitions (Waddell, 2006).

2.2. *Ordinary water ice*

2.2.1. Water

Life on earth depends on the unusual properties of water (Luck, 1985). In total at least 41 anomalies of water have been named such as: non-ideal vapour, high dielectric constant, and changes in various properties between hot and cold water, a low density (temperature of maximum density is 277 K) and the actual structures of water and ice (Chaplin, 2001).

2.2.2. Hydrogen bonding and proton ordering.

The hydrogen atoms in a water molecule are about 108° apart. The positively charged portion of one water molecule is attracted to the negatively charged portion of a neighbour. This attraction, termed hydrogen bonding, gives water many of its unique properties.

There are two hypothetical networks of water molecules (see Figure 10). On the left hand side, the bonds are proton-ordered: hydrogen atoms are bonded to oxygen atoms in a regular pattern. On the right hand side, the bonds are proton-disordered: hydrogen atoms are bonded to oxygen atoms in a random fashion, although there is a hydrogen atom between every pair of adjacent oxygen atoms. Proton-ordered networks form at temperatures below -80 to -100^{0}C.

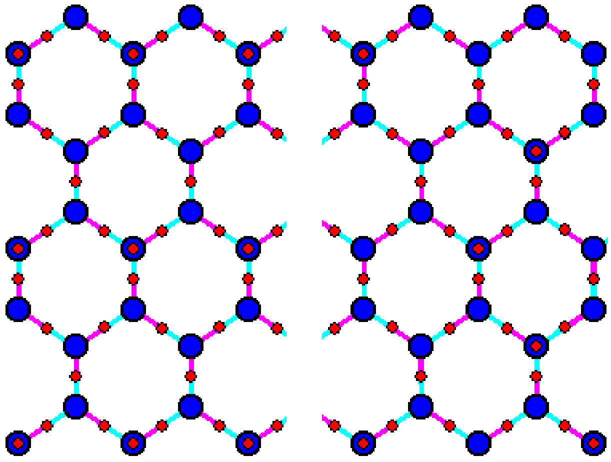

Figure 10: Proton-ordered (left) and proton-disordered (right) networks of water molecules. Hydrogen = blue), oxygen = red, bonds within a water molecule = violet, hydrogen bonds = light blue.

2.2.3. Water crystallisation

Freezing of water is a crystallisation process (Leloux, 1999). It begins with the generation of a sufficient driving force enabling nucleation of molecules in order to create a crystal lattice. Further addition of molecules or coagulation/aggregation with other nuclei of crystal lattice occurs during respectively secondary nucleation and crystal growth.

Supersaturation is a thermodynamically metastable state of a liquid being supercooled, or cooled below its freezing point. It can create a settling of molecular clusters either heavier or lighter than the surrounding solution and a reduction in viscosity and/or diffusivity, leading to the formation of clusters. The freezing point of ice is decreased if small solutes are present in solution at high concentration. If macromolecules are added in solution, many small ice crystal are created instead of macroscopic ice crystals

The structure of ice is a loose three-dimensional array of regular tetrahedra with oxygen in the centre of each tetrahedron and hydrogen atoms at the four corners. The hydrogen atoms are not exactly midway between the oxygen atoms (Pauling, 1935). Roughly one sixth of the hydrogen bonds of ice are broken when ice melts, which explain why the structure of ice at 0 °C occupies a larger volume than the same mass of liquid water at that temperature.

Ice exhibits a large number of polymorphs depending on the temperature and pressure as shown in Figure 11. Ice on earth is Ice I, which exists in two forms: hexagonal ice and cubic ice.

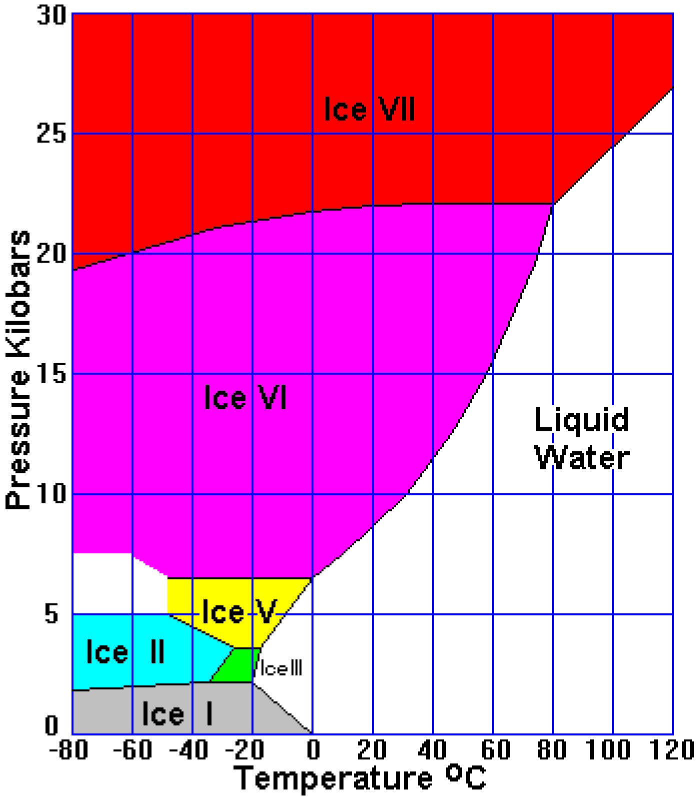

Figure 11: Phase diagram showing the various forms of ice existing over a range of pressures and temperatures.

2.2.4. Hexagonal Ice (Ice Ih)

At 0.1 MPa and 273 K water crystallises into a hexagonal polymorph of ice Ih, which is the form of all natural snow and ice on earth, as evidenced by the six-fold symmetry in snow flakes. Ice Ih has tetrahedrally coordinated water molecules and disordered protons. The H_2O molecular dimensions are unlikely to be distorted by the static or dynamical disorder in the ice structure (Katrusiak, 1996).

Ordinary ice consists of two interpenetrating lattices with a hexagonal close packed stacking arrangement.

The structure of ice Ih is shown in Figure 13. The Ih structure has a relatively low density, with a distance between the oxygen atoms of 4.5 Å.

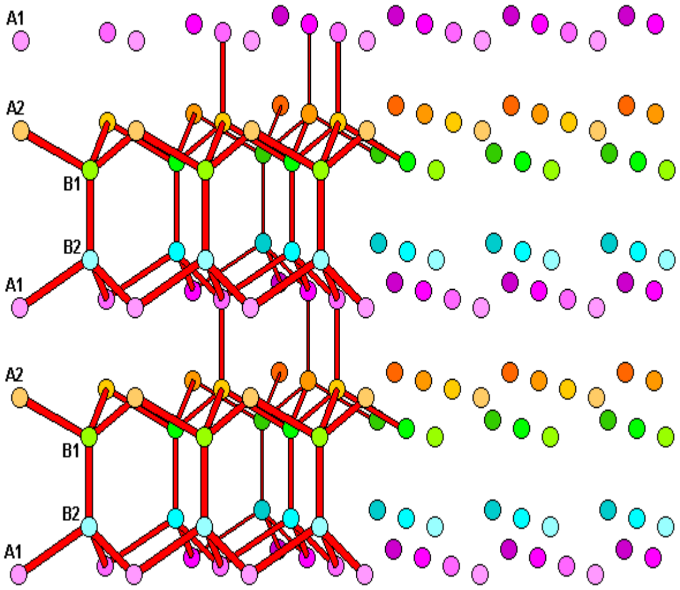

Figure 12: The structure of hexagonal ice, Ih. The sets of layers are numbered 1 and 2 with darker colours towards the rear of the structure. Red lines show O-H-O links.

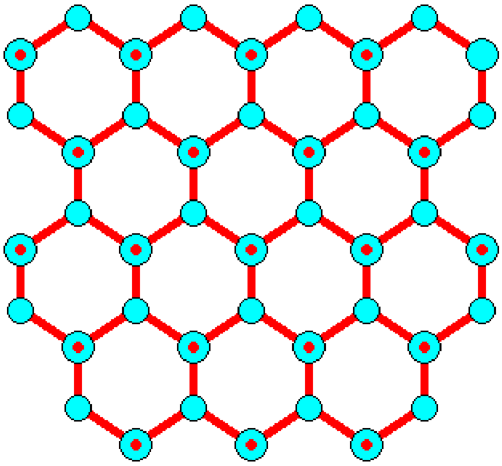

Figure 13: Top view of the Ice Ih structure. Red dots on some atoms mark a B layer with O-H-O links pointing up to the next B layer. Other atoms are in an A layer and have O-H-O links pointing down to the next A layer.

2.2.5. Cubic ice (Ice Ic)

Cubic ice is a metastable form of ice that can be formed, by condensation of water vapour, at ambient pressure only at very low temperature (less than -80°C) or by reducing the pressure. In cubic ice, oxygen atoms have a cubic packing arrangement. Figure 14 shows the structure of the cubic ice.

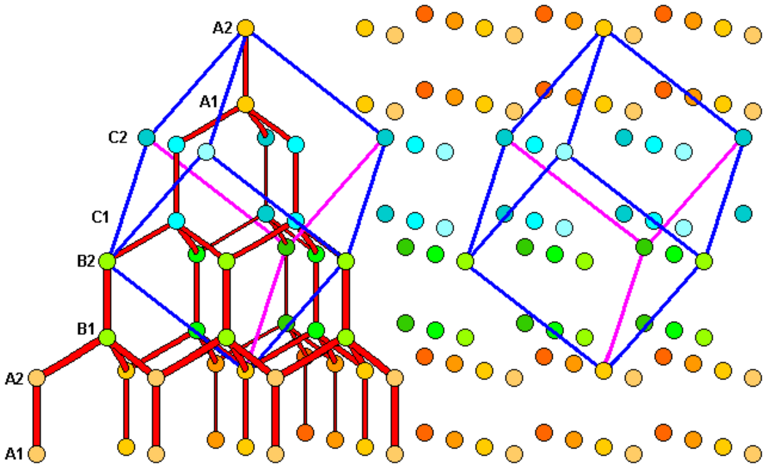

Figure 14: Cubic ice structure

Ice Ic has almost exactly the same density as Ice Ih. Ice Ih does not change to Ice Ic at very low temperatures but Ice Ic readily reverts to Ice Ih when warmed above -80°C. Ice Ic may form in extremely high clouds and some halo features not readily explainable in terms of hexagonal ice have been attributed to Ice Ic. The Ic structure is more dense (with the distances between the oxygen atoms about 3.4 Å)

2.3. Aim and objectives

The aim of this thesis is to demonstrate that a microfluidic device can be fabricated in ice with a laser.

The objectives of the thesis are: firstly to study the laser-ice interactions during the marking of channels in ice (section 3); secondly to show that microchannels made in ice can be effective components of a microfluidic device (section 4) and finally to investigate the applications of microfluidic channels created in ice (section 5).

3. Marking of open channels in ice with a CO_2 laser

3.1. *Laser uses on ice in the literature*

The beginning of The Empire Strikes Back, episode V of Star Wars, released in 1980, featured a laser cannon that carved into ice. What was only the fruit of the imagination of George Lucas became reality only a decade later.

The first laser (light amplification by stimulated emission of radiation) was created in the late 50s out of a ruby crystal (Maiman, 1960). A Laser is a coherent, convergent and monochromatic beam of electromagnetic radiation with wavelength ranging from UV to Infrared (IR). Since the 60s lasers have found a wide range of applications in engineering (Ion, 2005), medicine (Wolbarsht, 1991) and electronics (Steen, 2005).

One of its applications is laser ablation. This consists of the removal of material from a surface with a laser beam of high power by vaporising the material. It was first observed by Guo *et al*. in 1995 on a block of graphite. Laser ablation is now a common technique used for the removal of paints or coatings (McLean *et al*., 1997).

In 1973, a CO_2 laser of 50 W was used to cut ice of up to 3 cm width. The cuts had an average width of 30 mm (Clark *et al*.) however this idea was not explored until the 90s. In 1991, samples for ice core analysis were cut quickly and cleanly with a CO_2 laser of 15 W (Zeller *et al*.). The cut were 2 mm wide.

In parallel, patents were filled in North America for laser induced ice removal from surfaces such as plane wings (Vega & Vega, 1990) or electrical power lines or building (Long, 1999). The CO_2 laser was preferred for both applications because the beam emitted would vaporize ice without affecting the surface on which ice was found since the CO_2 laser beam penetration depth is only up to 2 mm. Also, the high absorption coefficient if ice at the laser wavelength (10650 nm) (Bass, 1995) makes the device energy efficient, .

In 2001, laser ablation was a new tool for investigating ice cores. The laser enabled the vaporisation of small cavities in ice, which offered a lower risk of contamination and better spatial resolution compared to conventional methods (Reinhardt *et al.*). The laser operated at a wavelength in the UV and its beam could be focused to small spots with the radiation being absorbed strongly within the material.

In 2006, Jennison & Gibala presented a laser ice etching system using a CO_2 laser. This system aimed to make ice cubes as well as to mark designs on the ice cubes formed. The formation of the design was due to explosive evaporation: when the laser beam contacted the surface of the ice cube, ice was immediately vapourised, leaving the mark of the design on the ice.

The idea of making microfluidic devices in ice with a CO_2 laser, investigated in this thesis, relies on the same principle as laser ablation. The laser beam is used as a tool to melt or vaporise a predetermined design area.

The following chapter presents the method of marking microchannels in ice with a CO_2 laser, the optimum laser set up for this application and experimental results showing how the channels parameters are affected by the laser power and beam velocity.

3.2. Laser-ice interactions

The literature on laser processing is very abundant for materials such as metals, polymers or ceramics but does not exist for ice. This section presents a simple model of the laser-ice interactions inspired by the existing models for others materials, which takes into account the properties of ice and the experimental observations.

In all the existing models on laser processing, the thermal properties of the materials interacting with the laser are assumed to be constant with temperature. This assumption, for the purpose of simplification of the model, is also made here. Models also assume that the energy provided by the laser beam is entirely used for the melting or vaporisation process; possible heat conduction in the material is neglected (Steen, 2005). For this assumption to be valid the penetration depth of the laser should be similar to or larger than the thermal diffusivity depth $\sqrt{(\alpha t)}$ where α is the thermal diffusivity ($\alpha = k/\rho c_p$) and t is the time of scanning of a single microvector ($t = d_b/v$) where d_b is the beam diameter and v the beam velocity (Duley, 2004). This condition shows that the smallest dimensions achievable depend on the material properties and the beam velocity. This assumption was also made in the laser/ice model presented below and will be verified in the experimental section.

The main parameters considered where the laser is concerned were the power and the marking velocity. In the first section, the interaction of the laser with an uncovered ice surface (when the channels and patterns created in ice are open) is considered. In the second section, the model is extended to the situation where a cover glass covers the ice surface (closed channels).

3.2.1. Marking of open channels

3.2.1.1. The laser beam

The reflectivity R of the material is the ratio between the reflected intensity and the irradiated intensity, the transmissivity T is the ratio between the transmitted intensity by the irradiated intensity and the absorptivity A is the ratio between the absorbed intensity and the irradiated intensity (see Figure 19). A, R and T are related by the equation:

$$A + R + T = 1$$ **Equation 6**

The transmissivity is also related to the absorption coefficient, a, of the materials by the Bert-Lambert law:

$$T = \frac{e^{-ad}}{1 - R}$$ **Equation 7**

where d is the thickness of the material.

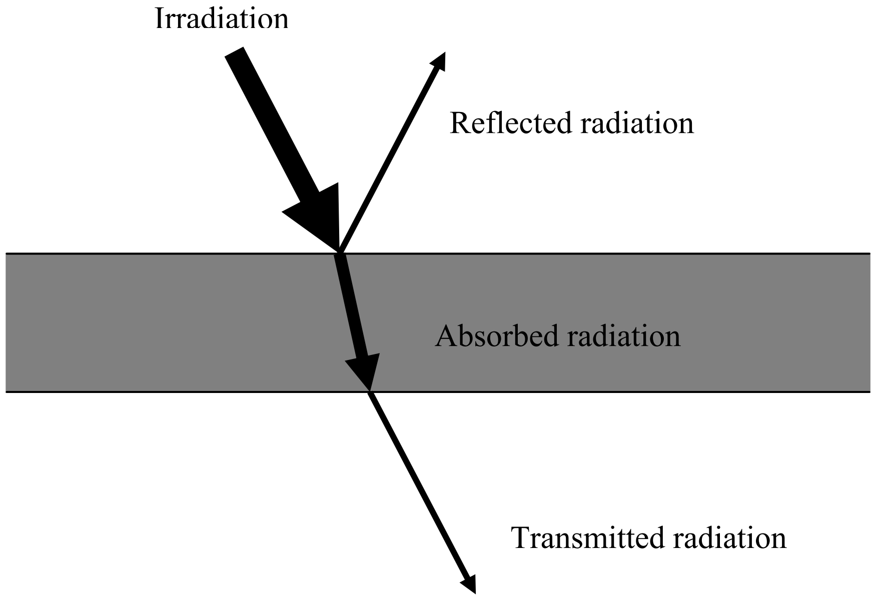

Figure 15: Reflection, absorption and transmission of the laser irradiation by a material. A part of the incident radiation is reflected from the surface of the material, a part is absorbed by the material and the remainder passes through the material as the transmitted beam.

For opaque materials, no light is transmitted. The absorption coefficient, a, is high and T = 0, therefore the absorptivity of the material A is given by:

$$A = 1 - R$$ **Equation 8**

At 10650 nm, ice at 100 K has a reflectivity of 0.5% and an absorption coefficient of 2.0×10^{2} cm^{-1} (Bertie *et al.*, 1968) and water has a reflectivity of 0.8% (Irvine & Pollack, 1968) and an absorption coefficient of 7.0×10^{2} cm^{-1}(Brass, 1995). The very small reflectivity and large absorption coefficient of water and ice means that A ≈ 1. All the energy of the laser is absorbed by ice and water.

3.2.1.2. Relation between the laser intensity and the melted cross-sectional area of a channel

The energy required to melt a design in one scan is related to the power of the laser beam as follows:

$$W = \frac{Q}{t} \qquad \textbf{Equation 9}$$

where W is the power, Q the energy and t the time of scanning.

The threshold power P* is the limit value below which melting does not occur was expressed in Duley (1999) as:

$$P^* = \pi k d_b (T_m - T_0) \qquad \textbf{Equation 10}$$

where k is the thermal conductivity of ice, d_b the beam diameter, T_m the melting temperature and T_0 the initial ice temperature. With d_b = 118 µm, T_m-T_0 = 6°C, k= 2.26 W/mK, the threshold power has a value of 0.025 W. A very small laser power can melt the ice.

The total heat used to melt the design created in ice is given by:

$$Q = \rho_{ice} V_{design} (c_{pice} \Delta T_1 + \lambda + c_{psolution} \Delta T_2) \qquad \textbf{Equation 11}$$

where ρ_{ice} is the ice density, V_{design} is the volume of the design in ice, λ is the latent heat of fusion, c_{pice} and $c_{psolution}$ are respectively the ice and solution heat capacity and ΔT_1 and ΔT_2 are respectively the temperature of heating in ice and in solution. The temperature of fusion of ice is 0^0C, ΔT_1 equals to $-T_{ice}$ and ΔT_2 equals to T_{water}, the final temperature of the melted solution.

In the applications of a CO_2 laser on ice described in section 3, the laser vaporised the ice. For microfluidic applications, channels should not to be created by vaporisation but by melting of the channel contents which would then allow a continuous flow to occur inside them. Therefore T_{water} should not exceed 100^0C.

When a linear object is marked by the laser (see Figure 16), the time of marking is the ratio between the length l_{design} of the object and the beam velocity. After substituting Q and t, equation 9 becomes:

$$W = \frac{V_{design}}{l_{design}} \rho_{ice} v \left(c_{pice} \Delta T_1 + \lambda + c_{psolution} \Delta T_2 \right)$$ **Equation 12**

where the ratios V_{design} by l_{design} equals to the cross sectional area melted in ice A_{design}:

$$\frac{V_{design}}{l_{design}} = A_{design}$$ **Equation 13**

When a filled object is marked by the laser (see Figure 16), the lines scanned by the laser are scanned at velocity v while the galvanometer moves from one line to the next with the velocity v' independent of v. The time of scanning can be approximated to $(v + v') \times l_{design}$. When the marking velocity is chosen such as $v = v'$, the time of marking was $2vl_{design}$. The relation between the power of the laser and the velocity of the beam for a filled object verifies equation 12 with a coefficient 1/2. However, the beam path l_{design} can be difficult to estimate for certain object geometries and since the time of marking can be easily measured, equation 9 should be applied.

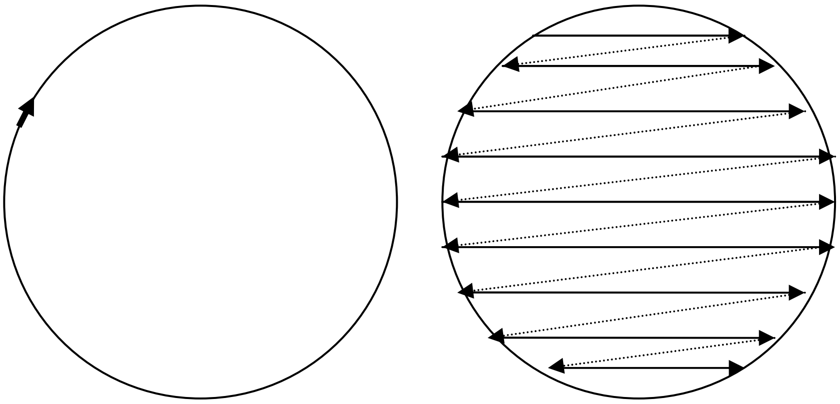

Figure 16: Left: marking of a linear object. The laser follows the contour of the object. Right: marking of a filled object. The laser follows lines inside the object. Arrows show the direction of the laser.

The following equation shows that the ratio of the power of the laser by the beam velocity is constant for a given design. This ratio is the laser intensity I:

$$I = \frac{W}{v} = \frac{Q}{l_{design}} = A_{design}\rho_{ice}(c_{pice}\Delta T_1 + \lambda + c_{psolution}\Delta T_2) \qquad \textbf{Equation 14}$$

In different models, the cross section of a cut by the laser was either modelled as rectangular (Zhou & Mahdavian, 2003) or circular (Ion, 2005). Experiments in ice showed that the widths of channels varied with the laser beam power and the velocity, the cross-sectional area of the channel created around the point of the beam where it hits the ice surface was here modelled as semi-circular as shown in Figure 17 and in cross section in Figure 18.

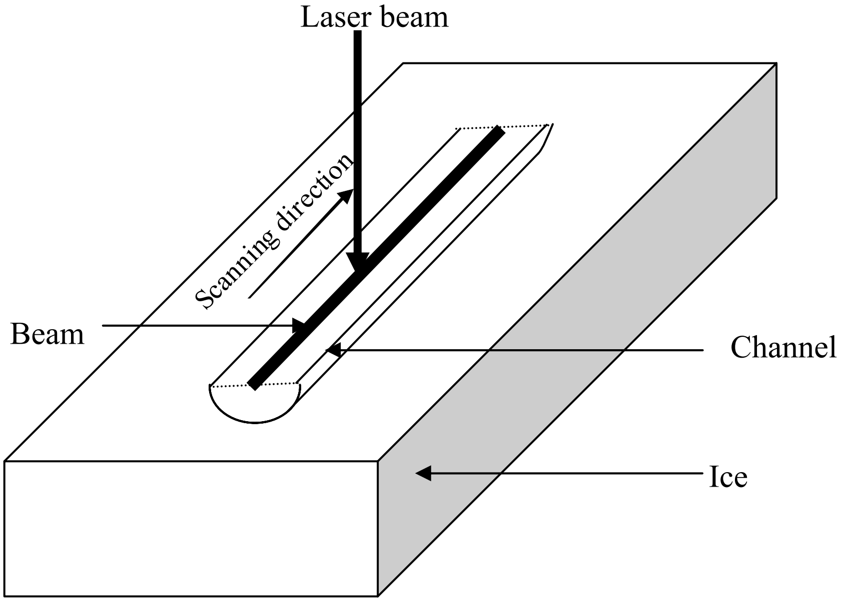

Figure 17: Schematic view of the marking of a channel on ice. The moving laser beam heats the ice creating a channel.

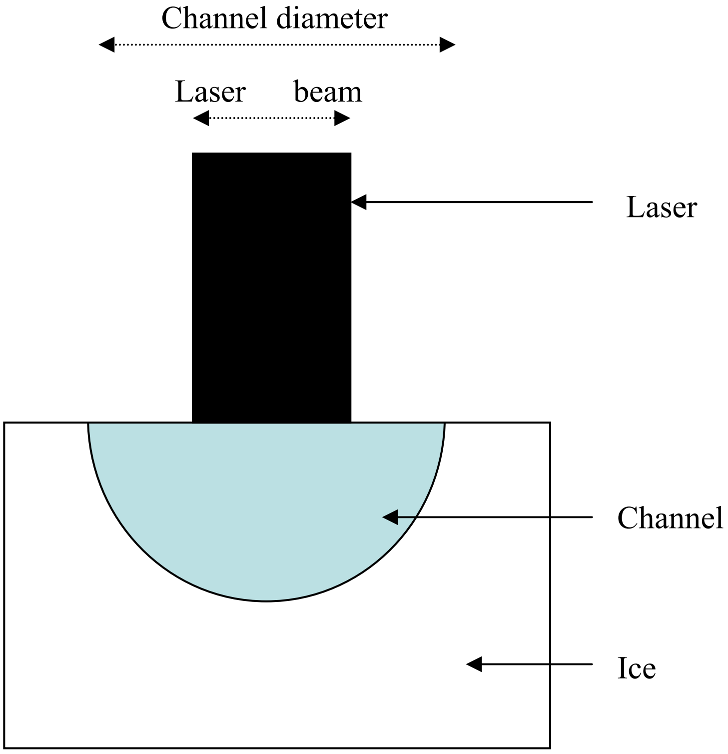

Figure 18: Cross sectional area of a channel marked in ice with the laser beam

The melted channel has a radius $r_{channel}$ and is related to the laser intensity as follows:

$$r_{channel} = \sqrt{\frac{2I}{\pi\rho_{ice}(c_{pice}\Delta T_1 + \lambda + c_{psolution}\Delta T_2)}}$$ **Equation 15**

Most of the experiments were designed in frozen water or highly diluted solutions. For ice/water, c_{pice} = 2.1 KJ/KgK, λ = 334 KJ/Kg and $c_{psolution}$ = 4.2 KJ/KgK. Since $T_{ice} = -6^0$C, the heat term coming from the ice heat capacity can be neglected. When marking channel the temperature increase recorded was below 10^0C and the term coming from the heat capacity of water can also be neglected. The latent heat is the most significant term of heat in the previous equation which can be simplified to:

$$r_{channel} = \sqrt{\frac{2I}{\pi\rho_{ice}\lambda}}$$ **Equation 16**

3.2.1.3. Temperature inside a channel after a single scan

The temperature profile in a material after a single scan was derived by Ashby and Easterling in 1982. The peak temperature after a single scan is reached at a point of a distance r from the laser beam at a time:

$$t = \frac{r^2}{4\alpha}$$ **Equation 17**

where α is the thermal diffusivity.

For thick materials, in which the thickness is larger than the diffusivity depth, the difference between the value of the peak temperature and the initial temperatures T_0 is given by the following equation:

$$T_p - T_o = \frac{2}{\pi e}\frac{I}{\rho c_p r^2}$$ **Equation 18**

After scanning, the cooling of the material at a distance r from the laser beam with time is given by:

$$T - T_0 = \frac{I}{2\pi kt} e^{-\frac{r^2}{4\alpha t}} \qquad \textbf{Equation 19}$$

For thin materials, in which the thickness d is smaller than the diffusivity depth, the peak temperature and the cooling equations are:

$$T_p - T_0 = \frac{1}{\sqrt{2\pi e}} \frac{I}{\rho c_p dr} \qquad \textbf{Equation 20}$$

$$T - T_0 = \frac{I}{2d\sqrt{\pi k \rho c_p t}} e^{-\frac{r^2}{4\alpha t}} \qquad \textbf{Equation 21}$$

3.2.1.4. Temperature inside a channel after repeated scanning

When n scans are repeated at a time intervals τ, such as $\tau > r^2/4\alpha$, the equations become:

For thick materials:

$$T_p - T_o = \frac{2}{\pi e} \frac{I}{\rho c_p r^2} + \frac{nI}{2\pi k \tau} e^{-\frac{r^2}{4\alpha\tau}} \qquad \textbf{Equation 22}$$

$$T - T_0 = \frac{I}{2\pi kt} e^{-\frac{r^2}{4\alpha t}} + \frac{nI}{2\pi k \tau} e^{-\frac{r^2}{4\alpha\tau}} \qquad \textbf{Equation 23}$$

And for thin materials:

$$T_p - T_0 = \frac{1}{\sqrt{2\pi e}} \frac{I}{\rho c_p dr} + \frac{nI}{2d\sqrt{\pi k \rho c_p \tau}} e^{-\frac{r^2}{4\alpha\tau}} \qquad \textbf{Equation 24}$$

$$T - T_0 = \frac{I}{2d\sqrt{\pi k \rho c_p t}} e^{-\frac{r^2}{4\alpha t}} + \frac{nI}{2d\sqrt{\pi k \rho c_p \tau}} e^{-\frac{r^2}{4\alpha\tau}} \qquad \textbf{Equation 25}$$

3.2.1.5. Maximum temperature inside the channel

When scanning is continued with constant laser power and beam velocity, the heat flow becomes steady and the temperature reaches a maximum value. The expression of maximum temperature reached inside a solid heated by a point source moving at a constant speed v was derived by Rosenthal (1946) as follow:

$$T_{\max} = T_{ice} + \frac{W}{A\rho c_p v} = T_{ice} + \frac{I}{A\rho c_p} \qquad \textbf{Equation 26}$$

where A is the heated area. When the heated area is a channel of length l and radius r, the area A = 2lr.

3.2.1.6. Evaporation of the channel content

For high laser intensities, the design of the channel in ice is achieved by evaporation instead of melting. Evaporation can happened after a single scan or after repeated scanning. The critical value of the intensity at which the ice will sublime can be found using the temperature expressions given above.

Also the energy required to sublime a volume V_{design} in ice is:

$$Q = \rho_{ice} V_{design} (c_{pice} \Delta T_1 + \lambda + c_{psolution} \Delta T_2 + \lambda_v) \qquad \textbf{Equation 27}$$

where λ_v is the latent heat of vaporisation.

For water, as earlier the ice heat capacities term can be neglected, however the water heat capacities cannot since the temperature increase in now equal to or exceeds 100°C.

The relation between the laser intensity and the radius of the evaporated channel of radius r created by one scan is:

$$r = \sqrt{\frac{2I}{\pi\rho_{ice}(\lambda + c_{psolution}\Delta T_2 + \lambda_v)}}$$ **Equation 28**

3.2.1.7. Keeping the channel open

After the design is marked on the ice surface, water cools down and refreezes unless the laser keeps scanning through the design at regular intervals. Freezing of samples is explained in section 3.3.1. The freezing of channels follows the same process with the only difference being that the geometry of the freezing area is semi-cylindrical with radius r. The first step is the cooling of the channel to 0°C and the second step is the solidification of water.

The cooling time has been estimated in the literature (Gurney & Lurie, 1923) in accordance with the temperature of the surrounding ice and the initial temperature of the melted ice.

Then the time of freezing of the cooled solution follows the Stefan solution for a cylinder of radius r as:

$$t = \frac{\lambda\rho}{2k\Delta T} r^2$$ **Equation 29**

3.2.1.8. Transport of liquid inside open channels

Transport phenomena inside the area melted by the laser beam were observed in metal laser welding (Hawkes *et al.*, 1983). Various forces created during laser welding act on the melted area (Figure 19). The flow of the melted area is primarily driven by a surface tension force resulting from the variation of surface tension with temperature.

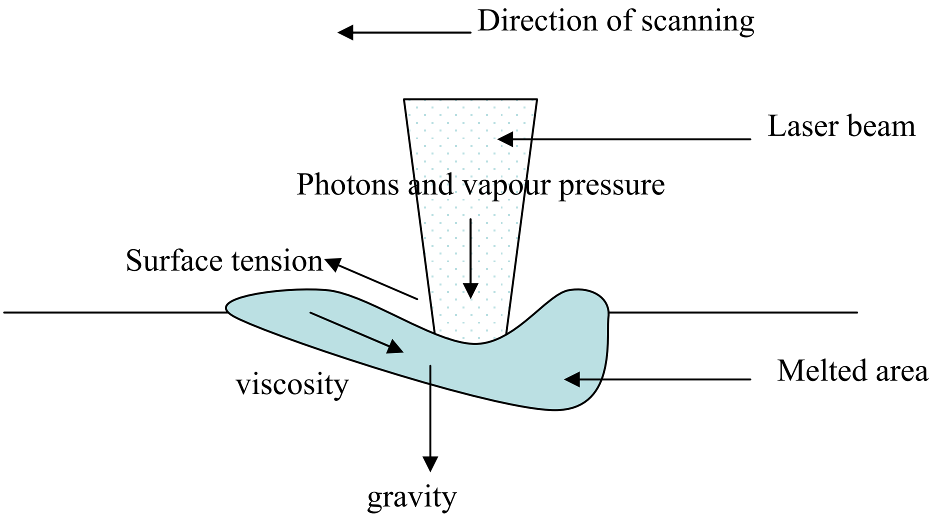

Figure 19: Forces acting on the melted area created by the laser beam (Steen, 2005).

The laser beam causes a thermal gradient in the melted area, which then undergoes a surface shear stress (dσ/dx) where σ is the surface tensions as follows (Steen, 2005):

$$\frac{\delta\sigma}{\delta x} = \frac{\delta\sigma}{\delta T}\frac{\delta T}{\delta x} \qquad \textbf{Equation 30}$$

The sheer stress τ due to viscosity acts in the opposite direction and is given by:

$$\tau = \eta \frac{dv}{dy} \qquad \textbf{Equation 31}$$

where η is the viscosity coefficient and dv/dy the velocity gradient perpendicular to the flow direction.

The gravitational pressure acting on a channel of height h is the product:

$$P_g = \rho g h$$ **Equation 32**

where ρ is the liquid density, g the gravitational acceleration of 9.8 m/s and h the height of the channel.

3.2.2. Marking of closed channels/cavities

To prevent evaporation during scanning, in some applications it can be beneficial to cover the ice surface with a glass slide (Figure 20).

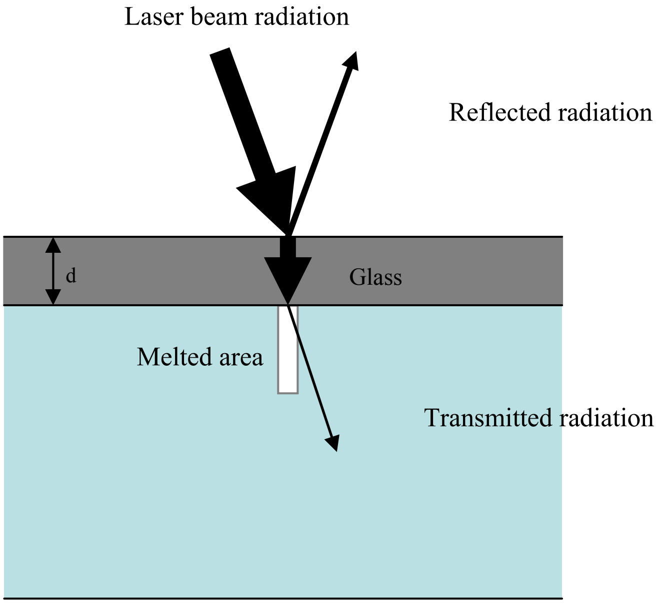

Figure 20: Schematic view of the laser beam passing through a cover glass slide.

The cover glass used in our experiments had a thickness d of 0.15 mm and a reflectivity R of 4%. The part of the laser beam energy entering the glass slide is therefore 0.96 W, where W is the laser beam power. The value of the cover glass absorption coefficient, a, was not provided by the manufacturer at the laser wavelength, however the relative data from the literature provides high values of absorption coefficients of other borosilicate glasses at 10600 nm (Sahba & Rockett, 1992) meaning that a significant part of the laser beam is absorbed by the cover glass. However the thickness (150 µm) of the cover glass is lower than the thermal diffusivity depth of the laser beam in glass (260 µm): when the laser heats the glass slide, heat is effectively conducted through the glass to the ice and enables melting as shown in Figure 21 where Tg is the outside glass slide temperature, Tg-c is the inside glass slide temperature and T_{ice} is the ice temperature.

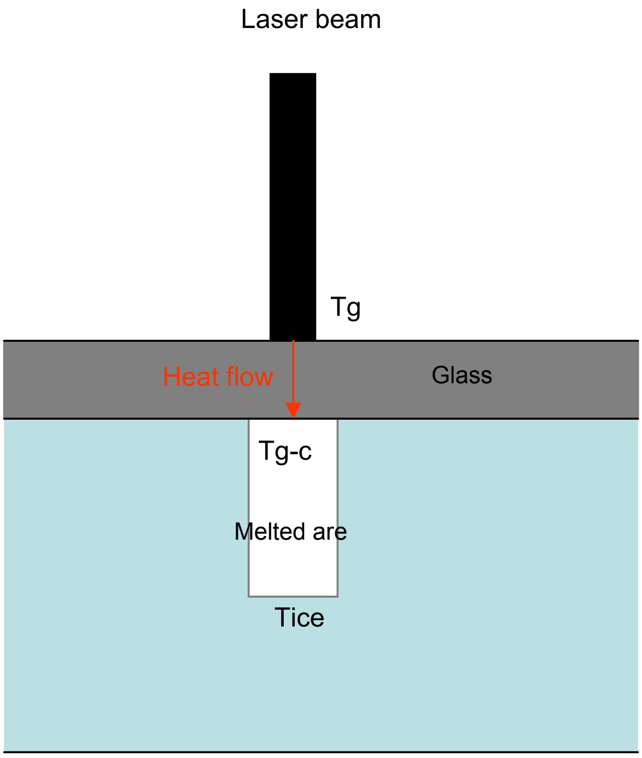

Figure 21: Heat flow (in red) through the glass slide from the glass surface heated by the laser towards the ice.

The power of the laser beam transmitted through the glass and the power of heat conducted through the glass are related to the energy Q required to melt the ice as follows:

$$W' = (1-R)e^{-ad}W + W_{heat} = \frac{Q}{t}$$ **Equation 33**

where W' is the power absorbed by the ice, W is the laser beam power, R is the reflection coefficient, a the absorption coefficient, d the glass thickness and W_{heat} is the heat flux with:

$$Q = \rho_{ice} V_{design}(c_{pice}\Delta T_1 + \lambda + c_{psolution}\Delta T_2)$$ **Equation 34**

as defined earlier.

Considering that the heat has melted the ice, the rate of heat flow conducted through glass and through the melted area of depth p is:

$$W_{heat} = -kA\frac{(T_{ice} - T_g)}{d+p} = -k_g A\frac{(T_{g/i} - T_g)}{d} = -k_w A\frac{(T_{ice} - T_{g/i})}{p}$$ **Equation 35**

where A is the area heated by the laser, T_{ice} is the ice temperature at the bottom of the channel, Tg is the temperature of the glass heated by the laser, Tg/I is the temperature at the ice/channel interface and k is the combined thermal conductivity of glass and the melted area, k_g and k_w are respectively the glass and water thermal conductivity.

The temperature variation inside the glass was shown to be a function of the laser beam intensity (see sections 3.2.1.3 and 3.2.1.4). The initial glass temperature will be the same as the initial ice temperature, therefore W_{heat} and the laser beam W are correlated. We can write:

$$W' = \beta W$$ **Equation 36**

where β is the correlation coefficient between W' and W.

When one scan is marked, the peak temperature of the glass (of thickness d) at the glass/channels interface can be calculated by the equation given by Ashby and Eterling (1982) for the case of a single scan on a thin material. Replacing Tg/I by its expression in Equation 35, the value of W_{heat} at peak temperature is:

$$W_{heat} = k_{water}\frac{A}{p}\frac{W(1-R)}{\sqrt{2e\pi v\rho_g c_{pg} d^3}} \qquad \textbf{Equation 37}$$

And the peak power at the ice interface W' is:

$$W' = (1-R)e^{-ad}W + k_{water}\frac{A}{p}\frac{(1-R)}{\sqrt{2e\pi v\rho_g c_{pg} d^3}}W \qquad \textbf{Equation 38}$$

For the known coefficient of correlation, the depth of the melted area is unknown and if the other parameters are known, it can be calculated as:

$$p = \frac{k_{water}A}{\beta-(1-R)e^{-ad}}\frac{(1-R)}{\sqrt{2e\pi v\rho_g c_{pg} d^3}} \qquad \textbf{Equation 39}$$

When the temperature has reached a stationary value (equation 20), the rate of heat flow is:

$$W_{heat} = \frac{k_{glass}k_{water}}{k_{glass}p + k_{water}d}\frac{(1-R)W}{\rho c_p v} \qquad \textbf{Equation 40}$$

where ρ is the glass density and c_p the heat capacity of glass. Both values were provided by the manufacturer (ρ= 2510 Kg/m^3 and c_p= 820 J/KgK).

The power at the ice interface becomes:

$$W' = (1-R)e^{-ad}W + \frac{k_{glass}k_{water}}{\rho c_p v(k_{glass}p + k_{water}d)}(1-R)W \qquad \textbf{Equation 41}$$

3.3. Methods

Equipment:

The liquid cooler was the LTD 20 G Grant (Cambridge, Cambridgeshire, UK). The laser 1-30 W IR CO_2 Fenix™ was supplied by SYNRAD (Mukilteo, WA, USA). The multimeter was the model 49T from Maplin (Rotherham, South Yorkshire, UK). The thermocouple was supplied by TME electronics (Worthing, West Sussex, UK). The Lock-In Amplifier Model SR 830 was supplied by Stanford Research Systems (Sunnyvale, CA, USA). The microscope/camera Digital Blue was supplied by Digital Blue (Heckmondwike, West Yorkshire, UK). The cover glasses were from Menzel-Glaser (Braunschweig, Germany).

Reagents:

Water was purified by reverse osmosis with the Elgastat B224 water purification unit (Elga Ltd, Marlow, Buckinghamshire, UK). Ethylene glycol and hydrochloric acid (HCl) were from Acros Organics (Loughborough, Leicestershire, UK). The platinum wires (product number 26720-1, 99.99 % purity) were from Aldrich (Gillingham, Dorset, UK). The quick set epoxy adhesive was from RS components Ltd (Corby, Northamptonshire, UK).

3.3.1. The freezing unit

A solution (usually water unless otherwise stated) was frozen inside reservoirs fixed on a flat cooling platform with flowing cooling liquid, consisting of an equi-volume mixture of water and ethylene glycol. The freezing unit worked in the temperature range of -30 to 100 ºC with a precision of ± 1 ºC. The freezing unit of 20 L capacity was cooled from room temperature to a set temperature (-10, -15 or -20 ºC). The following equation gives the theoretical cooling time of the unit in minutes when no liquid is in circulation:

$$t = \frac{V \Delta T c_p}{60W} \qquad \textbf{Equation 42}$$

where t is the time (min), V the volume of the cooling liquid (L), ΔT the temperature difference, c_p the volumetric liquid heat capacity (J/LK) and W the average cooling power of the unit (W).

3.3.2. Freezing of samples

The cassettes filled with solution were laid on top of the cooling platform and covered by a cover glass to isolate the solution from air.

The formation of an ice cube with one side in contact with a cooling platform and the other sides subject to natural convection was modelled and compared to experimental results by Kowalewski & Rebow (1999). The results showed that this complex problem is still not entirely understood and is very difficult to model accurately. In this particular case the area of the ice sample in contact with the cooling device was relatively large as compared to the side walls, in addition natural convection was ignored.

The overall thermal conductivity, density and heat capacity of the filled and covered cassettes are a combination of the properties of the cassette base, the solution and the cover glass:

$$\frac{1}{k} = (\frac{h_{base}}{k_{base}} + \frac{h_{solution}}{k_{solution}} + \frac{h_{glass}}{k_{glass}}) \times \frac{1}{h_{base} + h_{solution} + h_{glass}}$$ **Equation 43**

$$\rho = \frac{\rho_{base} h_{base} + \rho_{solution} h_{solution} + \rho_{glass} h_{glass}}{h_{base} + h_{solution} + h_{glass}}$$ **Equation 44**

$$c_p = \frac{\rho_{base} h_{base} c_{pbase} + \rho_{solution} h_{solution} c_{psolution} + \rho_{glass} h_{glass} c_{pglass}}{\rho_{base} h_{base} + \rho_{solution} h_{solution} + \rho_{glass} h_{glass}}$$ **Equation 45**

where h_{base}, $h_{solution}$ and h_{glass} are respectively the height of the base of the cassette, of the solution and of the glass cover, correspondingly, k_{base}, $k_{solution}$ and k_{glass} are respectively the thermal conductivity of the base of the cassette, of the solution and of the glass and ρ_{base}, $\rho_{solution}$ and ρ_{glass} are respectively the density of the base of the cassette, of the solution and of the glass and c_{pbase}, $c_{psolution}$ and c_{pglass} are respectively the heat capacity of the base of the cassette, of the solution and of the glass.

In most cases, the thickness of the base and the cover glass were very small compared to the height of the cassette. The thermal conductivity, density and heat capacity were then approximated to that of the solution.

The cassette height is relatively small compared to its surface area therefore the heat exchange in the cassette can be considered to be one-dimensional.

During freezing, the first step consists of lowering the temperature of the cassette-solution to 0 ºC. Over the temperature range of the cooling step, the thermal conductivity can be assumed to be constant and the temperature verifies the one dimensional heat equation:

$$\rho c_p \frac{\partial T}{\partial t} = k \frac{\partial^2 T}{\partial x^2}$$ **Equation 46**

where ρ is the density, c_p the heat capacity, k the thermal conductivity.

Equation 46 has been analytically solved and plotted (Gurney & Lurie, 1923) for various geometries. The height (h) of the cassettes is relatively small compared to the surface area. The plot of the solution of equation 46 in the case of slabs enables to estimate the time needed to cool a water solution from room temperature to 0 ºC.

The second step of freezing consists in the solidification of water into ice, it is the Stefan problem (1891). Stefan assumed a linear temperature profile which led to the expression between time and the ice thickness x as follows:

$$t = \frac{\lambda \rho_{ice}}{2k\Delta T} x^2$$ **Equation 47**

where k the thermal conductivity of ice, λ is the latent heat of fusion, ΔT is the temperature difference between the solution at 0 ºC and the cooling platform and ρ is the density of ice.

The time of freezing is the sum of the time of cooling and the time of solidification.

3.3.3. Set up for marking channels

The CO_2 laser used in this study was reliable, simple to use and cost effective. The laser marker generated a laser beam of wavelength 10650 nm with a maximum output power of 25 W. The laser marker was a self-contained system which consisted of a galvo-based marking head, internal cooling fans and power supplies. The light was focused by lenses into a small intense beam. The laser tube was a rigid box providing a very stable platform for the laser resonator. The laser was monitored through a PC via the Winmark software (USA).

As shown on Figure 22, the laser beam generated was delivered to *X* scanning mirror mounted at about 45° position. This deflected the beam at right angles. The beam was then reflected on a Y mirror onto the sample surface.

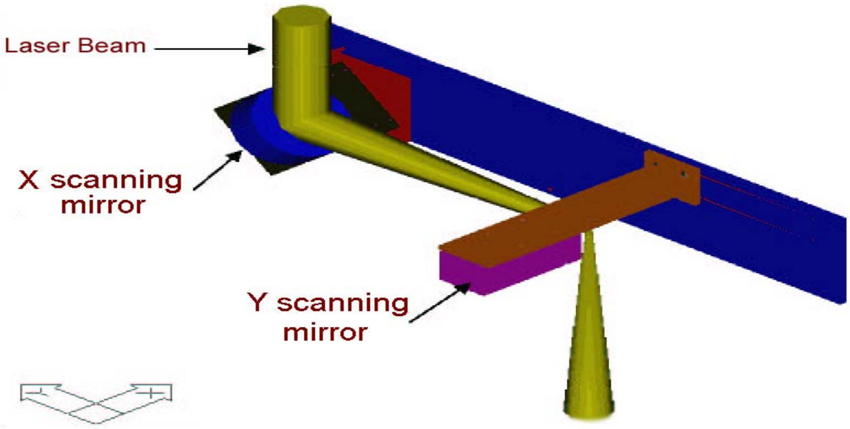

Figure 22: Schematic view of the laser scanning system

Samples were laid under the laser beam on a stage, the height of which could be adjusted with the rotation of a jack rotation wheel. A rotation of the wheel of 360° corresponded to a height increase of the stage of 15 mm. The focal length of the lens of the laser was 80 mm. The samples were positioned at the focal length. The focal length was tested when the laser beam could cut through a sheet of glossy paper at 20% power. When the height of the sample holder was higher or lower the laser beam did not cut the glossy paper but would only leave a mark on it. The top cooling fan exhaust of the laser was closed with tape in order to prevent warm air from melting the ice underneath the laser. The experimental room was cooled to 18°C.

The laser can mark vector objects made of a straight or curved path when the “vector marking” option is chosen (i.e. the beam moved along the vector). The laser can also mark filled objects when the ‘raster marking’ option is chosen. The beam switches on and off as it moves across the object and marks one pass, returns, moves down one step and marks another pass and so on until it has marked the whole object, as shown in Figure 16. The raster could move across the image horizontally, vertically or in both directions.

The design of the pattern to be marked could be imported or directly drawn into the Winmark software which controlled the laser. The number of passes, the power of the laser beam, the marking velocity (i.e. the microvector velocity), the resolution (number of microvectors per inch), the choice of a continuous marking or a spot marking and the choice of a unidirectional or bidirectional raster were inputted into the software. In all the cases the resolution chosen was 1000 microvectors per inch, the marking was continuous unless stated otherwise and when marking filled objects the marking was unidirectional. The only variables in the different marking were the power and the scanning velocity. When the sample was ready for marking, a simple click on the launch button on the software would start the marking process. The power input was in percentage of the maximum laser beam power (25 W) in 1% increments.

The experimental set-up can be seen in Figure 23.

3.3.4. Transport of liquid inside open channels

On order to test the transport of liquid in the open channels two apertures were created in ice, one of which was filled with a dye consisting of a solution of Meldolas’s Blue diluted at 0.8 g/L. The laser beam hitting the aperture would move the dye along the channel (see Figure 24).

In another experiment, 50 μL of dye were directly injected at the top end of the channel with a micropipette.

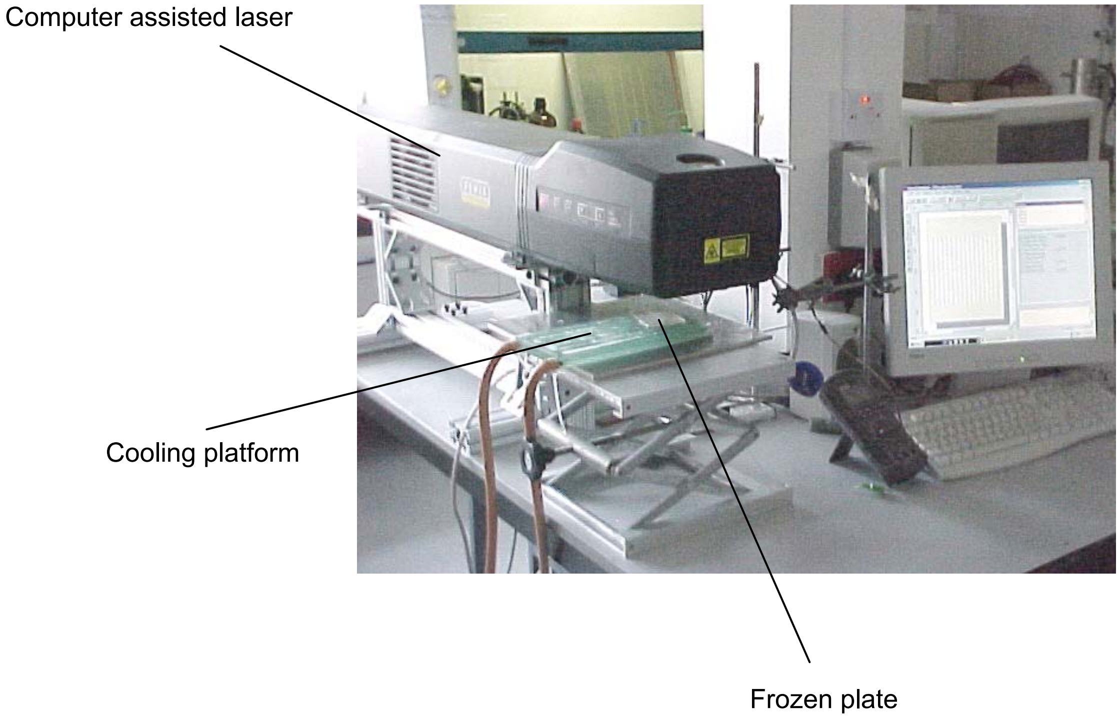

Figure 23: Set up for the marking of channels on ice with a computer assisted CO_2 laser.

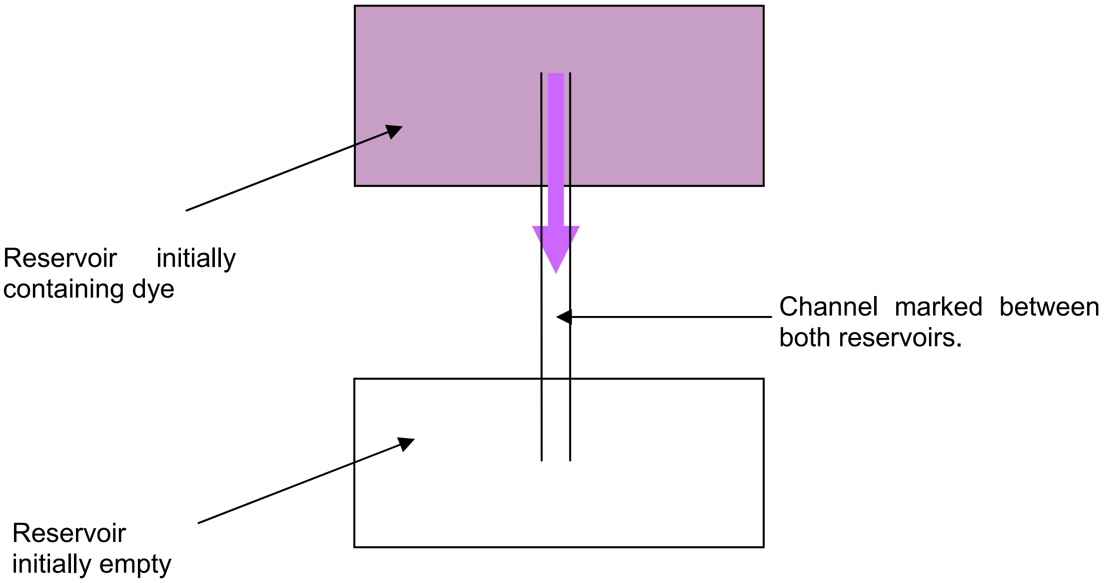

Figure 24: Marking of a channel between a reservoir filled with Meldola's blue and an empty reservoir. The laser drags the dye in the channel towards the empty reservoir.

3.3.5. Temperature and resistance measurements

The temperature and the electrical resistance inside the channels were measured in order to quantify the suitable laser conditions for the marking channels in ice as well as the time for which the channels are open.

3.3.5.1. Temperature measurements

A thermocouple (linked to a multimeter calibrated in degrees Celsius) was frozen inside the ice just under the surface (it can be estimated that the thermocouple was 0.5 mm under the surface). Channels were marked on the ice surface above the thermocouple.

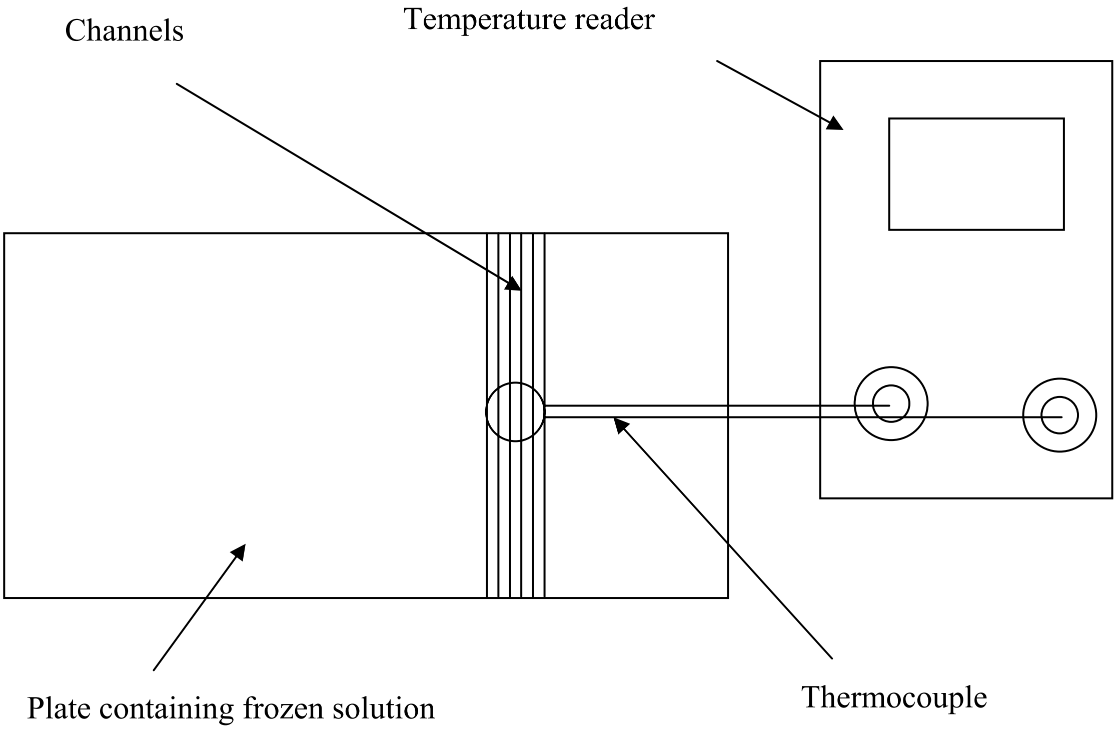

Figure 25: A thermocouple is frozen inside the ice for temperature measurements.

3.3.5.2. Resistance measurements

A conductive solution of 10 mM hydrochloric acid (HCl) was frozen inside a rectangular polypropylene cassette of dimensions 5.7 cm × 8.3 cm × 0.3 cm equipped with two platinum wires of 0.533 mm diameter, 9.5 cm long 1.5 cm apart. The wires were fixed to the cassette with epoxy glue and connected to a Lock-In Amplifier, with the following set up: alternating voltage of 100 mV and frequency of 100 kHz. An extra resistance of known value (r = 1 kΩ) was added in the circuit (see Figure 26) to allow calculation of the resistance between the wires from the voltage reading of the Lock-In from the following relation.

$$R = \left(\frac{V}{Vm} - 1\right) \times r \qquad \textbf{Equation 48}$$

where R is the solution resistance (Ω), V the input voltage of the Lock-In (V), Vm the voltage measured by the Lock-In (V) and r the series resistance added in the circuit (Ω).

The power dissipated in the channels by the Joules effect was related to the measured voltage as follow:

$$P = (V - Vm)\frac{Vm}{r} \qquad \textbf{Equation 49}$$

The Lock-In amplifier was linked to a PC and the measures taken by the Lock-In amplifier were recorded on the PC during freezing of the conductive solutions when the cooling device was set at various temperatures as well as during the marking of channels across the wires.

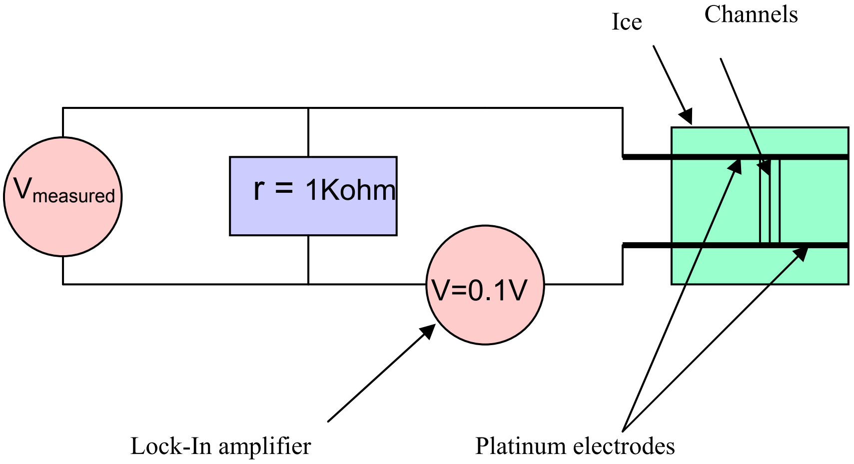

Figure 26: Circuit for the measurement of the electrical resistance in the channels drawn on the frozen solution

3.4. Results

3.4.1. The freezing unit

The freezing unit average power was 540 W. The heat capacity for a 50/50 water/glycerol mixture was 3800 J/LK. The estimated time to cool the mixture from 20 ºC to -10, -15 and -20 ºC were respectively calculated with Equation 42 as 70, 82 and 94 min. The cooling unit would therefore only be effective after one and half hours to 2 hours. Because of this time constraint, the freezing unit was continuously kept switched on.

3.4.2. Freezing of samples

The variation of electrical resistance in a 10 mM HCl solution, shown in Figure 27, were obtained from the recording of voltages by the Lock-In amplifier in the solution frozen at three different cooler device temperatures (-10, -15 or -20 ºC).

The resistance, which is inversely proportional to the conductivity, increased during freezing up to a plateau value of 4,500 Ω for the three temperatures tested. The solution froze quicker when the cooler temperature was lowest. Before reaching the plateau value, when the cooler temperature was set at -20 ºC or -15 ºC, the resistance reached a peak value and then slightly decreased after. The maximum resistance value should coincide with the phase transition point of the solution. In each following experiment the cooler was set at -20 ºC to obtain ice samples more quickly.

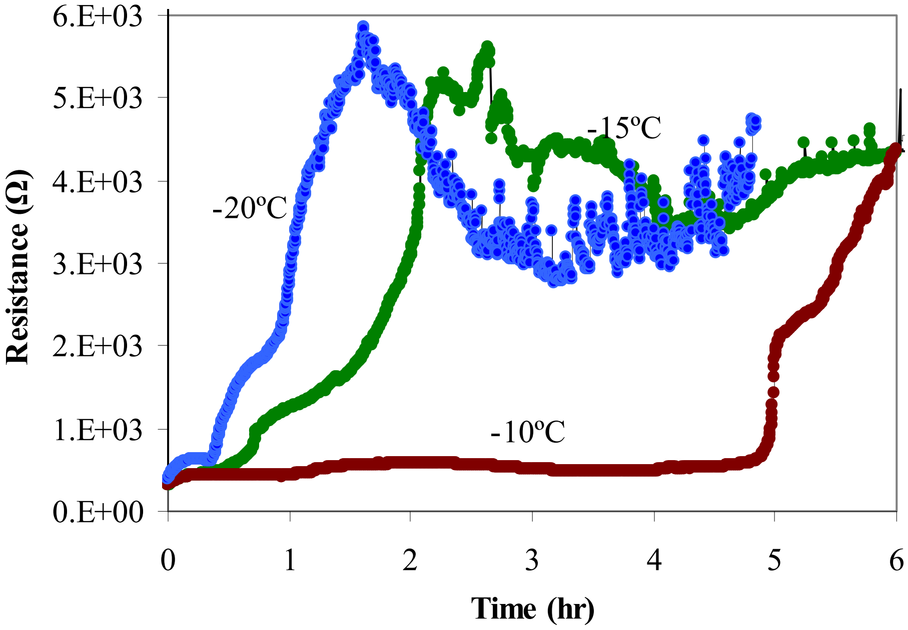

Figure 27: The change in resistance of a 10 mM HCl solution upon freezing for a cooler device at three different set temperatures (-10, -15 and -20 ºC).

Cassettes of various sizes, geometries and compositions were tested. The cassettes will be described in detail in the electrophoresis chapter. The larger the cassette, the higher the surface area available for heat exchange with the surrounding atmosphere through the sides and especially through the top of the cassette. This convection could be ignored for small cassettes where the estimation of the freezing time presented in section 3.3.2 was valid. However it cannot be ignored for larger cassettes. The geometry of the cassette also contributes to heat exchange with the surrounding atmosphere. Materials of small thermal conductivity were used in the design of the sides of the cassette while conductive materials of higher thermal conductivity were used for the bottom side of the cassette.

The best results (i.e. shortest time of freezing and good reproducibility of freezing time) were obtained with a cassette 2.4 cm × 2.4 cm made of a flat base in glass 1 mm thick having borders made of PDMS 2 mm thick of very low thermal conductivity (k = 0. 15 W/mK) and a cover glass on top 0.15 m thick. For these cassettes, the freezing process was quicker than for cassettes made entirely in Pyrex (thermal conductivity k = 1.1 W/mK).

3.4.3. Laser marking on ice

The 1-30 W IR CO_2 Fenix™ laser usually used for marking or cutting plastic, glass or metals enabled the marking of microchannels, cavities or more complex geometries in ice with the laser with good reproducibility (see Figure 28, Figure 29 and 16 taken with a Digital Blue camera with a 10 times enlargement lens).

Practically any type of geometric design of dimensions as small as 0.2 mm could be accurately created in the ice within minutes. The created design could be maintained in the ice during prolonged period of time by repeated scanning at some time intervals.

Figure 28 was taken after marking five channels with the laser set up at 3 % of the total power, a beam velocity of 5 mm/s with 5 scans (one scan every minute). The ice surface was uncovered to enable the channel to evaporate during the scanning so they would be open during picture taking.

The channels were 2 mm apart and it was estimated from the figure that they were 200 to 400 μm wide.

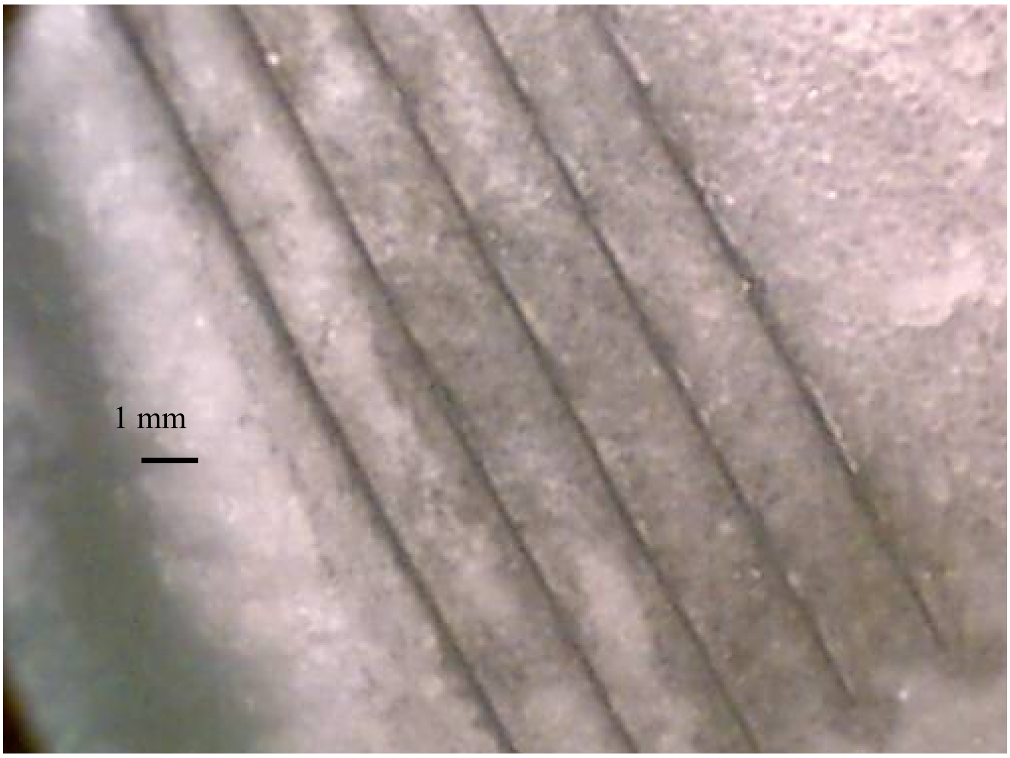

Figure 28: Channels marked with a CO_2 laser beam at 3% of total power and a 5 mm/s velocity (5 scans).

The value of the intensity of the laser for each scan was I = 150 J/m. From the value of laser intensity, the value of the radius r of the channels was calculated using Equation 16. The value found was 180 μm which agreed with the observation on Figure 28.

The laser-ice model will be valid only if the penetration depth r is greater that the thermal diffusivity depth $\sqrt{(kd_b/\rho c_p v)}$. The beam has a diameter of 116 μm, and for ice $k = 2.26$ W/mK, $\rho = 920$ Kg/m3 and $c_p = 2100$J/KgK. When v = 5mm/s, $\sqrt{(kd_b/\rho c_p v)} =$ 165 μm. The depth of the channel was larger that 180 μm and the condition of validity of the model was confirmed.

The ice thickness is relatively large compared to the thermal diffusivity depth, therefore ice can be considered a thick material and the value of the critical intensity above which evaporation occurs was calculated when the temperature in the channel of diameter r given by equation 16 for thick materials reaches 100°C. To evaporate a channel of 180 μm radius in one scan, the critical intensity value was found to be of 55 J/m.

Spots were just as easily marked in ice. Figure 29 showed cavities of diameters as small as 300 μm marked with the 1-30 W IR CO_2 Fenix™ laser. Figure 30 showed a pattern with spots and channels. The channels were marked with a laser beam at 3% of total power and a 100 mm/s velocity (20 scans), the cavities were marked with a laser beam at 1% of total power and a velocity of 100 mm/s (10000 scans).

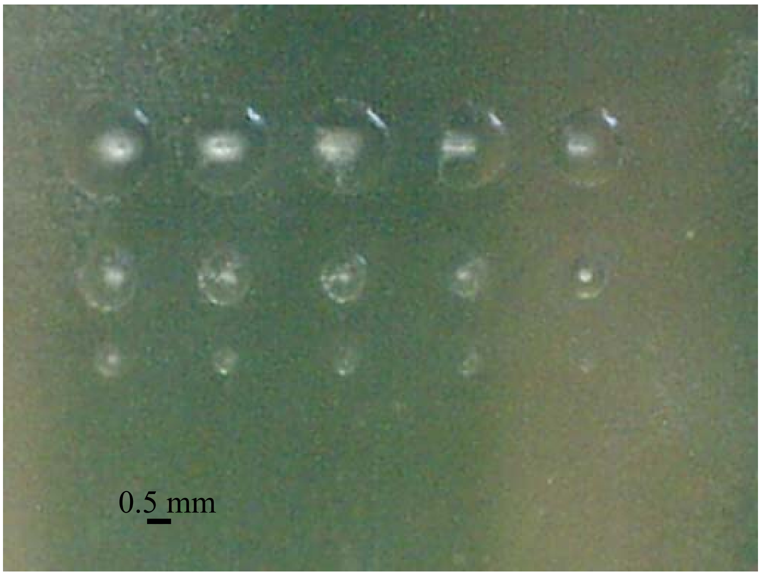

Figure 29: Cavities of decreasing diameters (from 1.5 to 0.3 mm) marked with a CO_2 laser beam at 4 % total power and a 100 mm/s velocity (25 times) using a spot marking style.

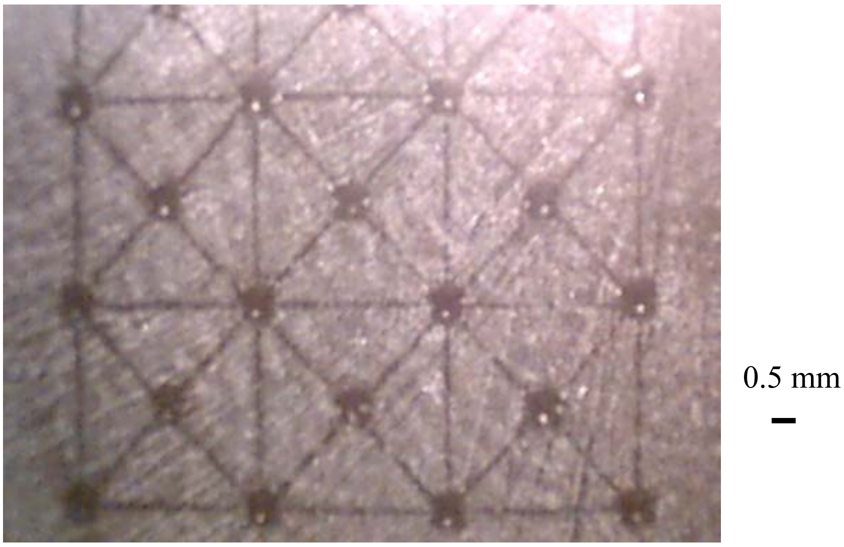

Figure 30: Pattern scanned in the ice with CO_2 laser beam of 100 mm/s velocity. 5mm long channels: 3% of total power (20 scans), 0.5 mm diameter dots: 1% of total power (10000 scans).

The literature was able to provide the experimental conditions for CO_2 laser processing in ice. Therefore trials of various power and velocity combination were necessary. Channels were marked with a single scan with a laser beam of velocity in a range between 100 and 200 mm/s. In all cases channels would become visible for powers above 2% and would become too large for powers above 8%. For the lower range of velocity, the channel would start to evaporate. Therefore the ranges 3-8 % for the power and 100-200 mm/s for the velocity were found to be optimal to mark non evaporated channels, which corresponds to a laser intensity range of 4-20 J/m. Similar intensity values could be achieved with other power and velocity settings for which this ratio was in the same range. The previous scanning velocities and power ranges were chosen because experiments could be monitored and controlled more easily when the marking was not instantaneous as it would be with higher velocities. It can be noted that in some particular cases when wide channels were necessary, higher laser intensities were also used.

Consecutively to those experiments, Meglinski *et al.* (2005) realised simulations of a simplified physical/optical model of ice marking with a CO_2 laser beam. He calculated the distribution of the power applied by unit area from which he deduced the optimum power and velocity which corroborate the optimum values found experimentally.

3.4.4. Transport of liquid inside open channels.

Liquid flow can be achieved through the channels created in ice with the laser as depictued in Figure 31. When the laser beam marked the channel in ice, the fluid inside the reservoir, or inputted directly in the channel with a micropipette, flowed inside the channel. The following picture shows a channel filled with Meldola's Blue dye. The channel started from a reservoir filled with Meldola's Blue and was marked with a laser beam at 5% power and a 100 mm/s velocity. After 100 scans the channel was filled with dye.

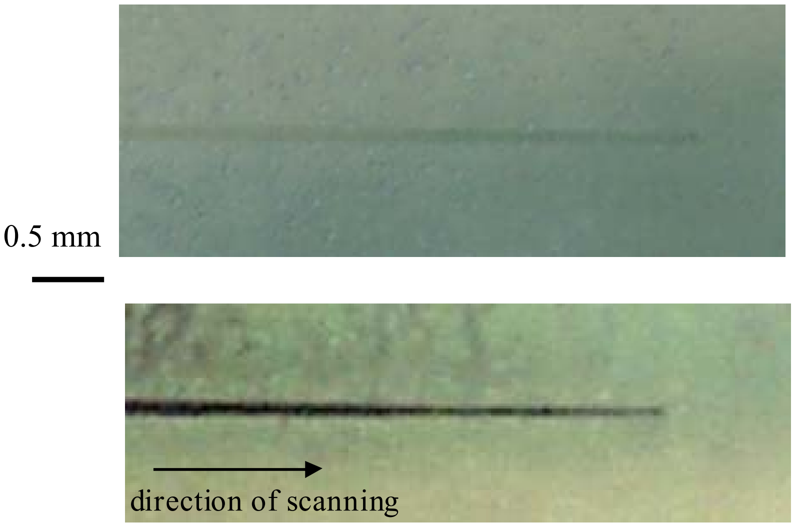

Figure 31: Microchannels formed in ice by repetitive scanning: empty channels (top) and filled with dye solution (bottom) marked with a laser beam at 5% and a 100 mm/s velocity (100 scans).

100 scans at 100 mm/s were necessary to move the dye along the whole channel. The velocity of the progression of the dye inside the channel can therefore be estimated to 1 mm/s. This value, although minimal, shows that transport inside the channel is possible by marking alone. However the flow was discontinuous: each scan makes the liquid advance further in the channel.

The physical properties of Melodola's Blue diluted at 0.8 g/L can be approximated to those of water. The variation of surface tension with temperature for water is $d\sigma/dT = 1.5\ 10^{-4}$ N/°C/m (Dean, 1999). The thermal gradient dT/dx is created when the laser beam hits the ice surface. After continuous scanning of one channel (5% power, 100 mm/s), the temperature increase in the scanned channel was 5 °C (see section 3.4.5.2). It can be assumed that the local temperature at the beam hit point on ice is far greater than the temperature recorded experimentally. However considering a 5 °C increase and the radius of the hot area of approximately 160 μm predicts dT/dx ~3.1×10^4 °C/m. The minimal surface shear stress acting in the melted channel has therefore a value of 4.6 N/m^2.

The highest viscosity coefficient of water is reached at 0 °C and has value of 1.8×10^{-3} Ns/m. The highest velocity of the liquid inside the fluid cannot exceed the beam marking velocity. Hence the maximal sheer stress caused by viscosity, in a channel of maximal height 0.4 mm and marked at 100 mm/s is 0.4 N/m^2.

The gravitational pressure acting on water inside the channel of same height was 3.9 N/m^2.

Therefore the surface sheer tension can cause the melted channel to flow. The real value can be expected to be even higher because of the high value of temperature at the beam hit point.

Flow depends on the Prandtl number, Pr = ν/d, where ν is the kinetic viscosity and d the thermal diffusivity. For materials of high Prandtl numbers (Pr >> 1) like ceramics or polymers, the motion of the melted area is retarded by the viscosity whereas for materials of low Prandtl number (Pr << 1) (e.g. metals), the viscosity has no effect on the melt motion (Tokarev & Kaplan, 1999). The Prandtl number of water is 9. This value explains that the motion of water inside the channel is limited by viscous friction. The Prandtl number (Chan *et al*, 1984) was also shown to dictate the aspect ratio (width divided by depth) of the channel created by the laser. The larger the Prandtl number, the more difficult thermal diffusion becomes and the higher is the aspect ratio. Water, with a Prandtl number close to unity, exhibits aspect ratio close to unity (hence channels of cylindrical shape).

3.4.5. Temperature measurements

The temperature created in the local scan area was measured as described in section 3.3.5.1. The thermocouple was frozen inside ice made of distilled water at -6°C. During the course of the experiments, the temperature of the bulk of ice remained constant.

3.4.5.1. Single scan inside an open channel

A thermocouple was frozen in the ice. After 6 s, a single channel was marked with a CO_2 laser beam at 100 mm/s and 6% power on the surface of the ice. The temperature profile recorded by the thermocouple is shown in Figure 32.

The thermal diffusivity depth of the laser beam scanned at 100 mm/s in ice is 27 μm and is negligible compared to the total thickness of the ice. The theoretical peak temperature and the temperature profile were therefore calculated with the equation 18 and 19, given for thick materials, and plotted against the measured temperature profile.

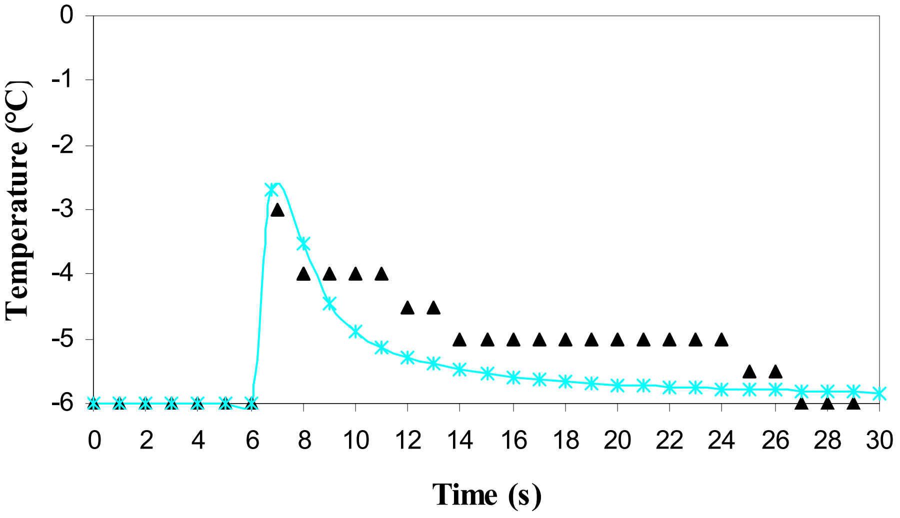

Figure 32: Temperature profile measured by a frozen thermocouple (black) and theoretical temperature profile (blue) following a single scan of one channel marked by a CO_2 laser beam at 100 mm/s and 6 % of total power.

The temperature increased by 3°C in a second after the scan. After that it decreased by 1°C in one second and by a further 2°C over 20 s.

When a scan is launched, there is a delay of 0.5 s between the launch ($t = 6$ s) and the actual start of the marking. The time at which the temperature increase is measured by the thermocouple which is at a distance $r = 0.5$ mm from the ice surface is $r^2/4\alpha$ where α is the diffusivity. The time was calculated to be 0.1 s. Also it took 0.3 s to mark the channel. The maximum temperature is reached approximately 0.9 s after the launch of the scan.

The intensity of the laser was 15 J/m. The solution was water. Therefore with the equations described in section 3.2.1.7, the theoretical refreeze time of a channel of opening radius of 180 µm was calculated as 0.7 s.

From the graph above, the channel can be assumed to be closed when the temperature measured falls below 4°C. After the temperature decreased past 4°C the temperature keep decreasing until it reached that of the surrounding ice.

The programmed repetition of scans every 0.7 s is required to maintain this channel open for these specific irradiation conditions.

3.4.5.2. Temperatures measured in open channels for various laser intensities

Figure 33 represents the experimental (black) and theoretical (pink) results for measuring the peak temperature reached inside a channel formed with 10 scans with a laser beam of 100 mm/s velocity and a power from 4 to 20 %.

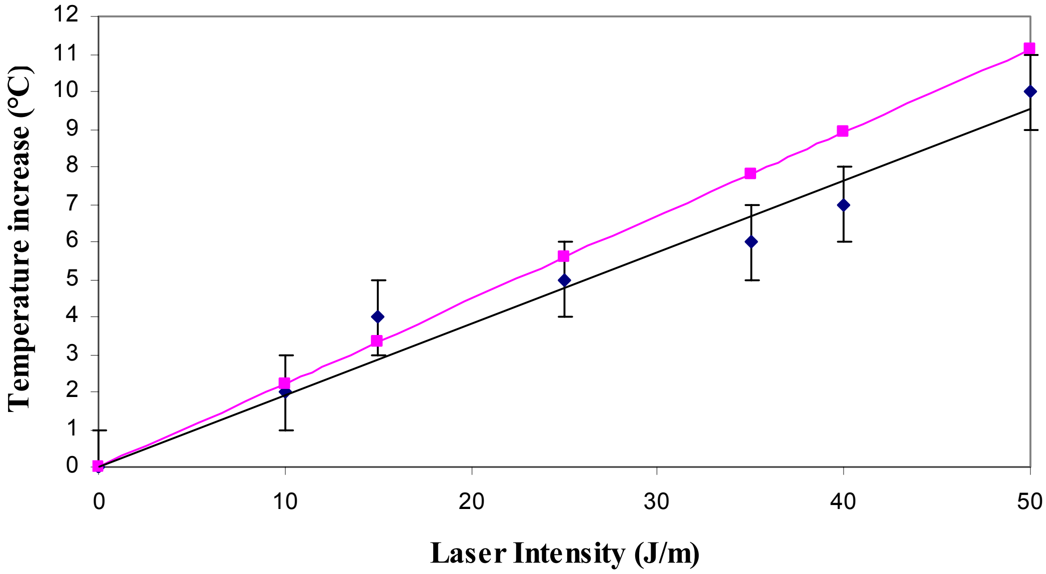

Figure 33: Peak temperatures reached after a single channel was marked with 10 scans at 100 mm/sec over a range of laser power from 4 to 20% (laser Intensity range from 10 to 50 J/m per scan) measured with a thermocouple compared to the theoretical temperature peak expected in the channel (pink) with standard error bars.

The temperature measured increased by 10 °C at the intensity of 50 J/m after 10 scans. This graph shows that the temperature inside the channel increases linearly with the laser intensity as does the theoretical peak temperature. At high intensities, more ice melts which lower the temperatures recorded compared to the theoretical peak temperature.

3.4.5.3. Continuous scanning of open channels

Figure 34 represents the temperature increase read by the frozen thermocouple when 10 channels were scanned repetitively for 8 minutes (30 scans of each of the 10 channels) on the ice area under which the thermocouple was frozen with a laser beam of 100 mm/s and 2 to 6% power. The intensity of the laser beam ranged from 5 to 15 J/m per scan. For powers above 3% (intensity of 7.5 J/m), the temperature increased linearly during the first 3 minutes of the scanning and reached a maximum temperature which was maintained for the duration of the scanning.

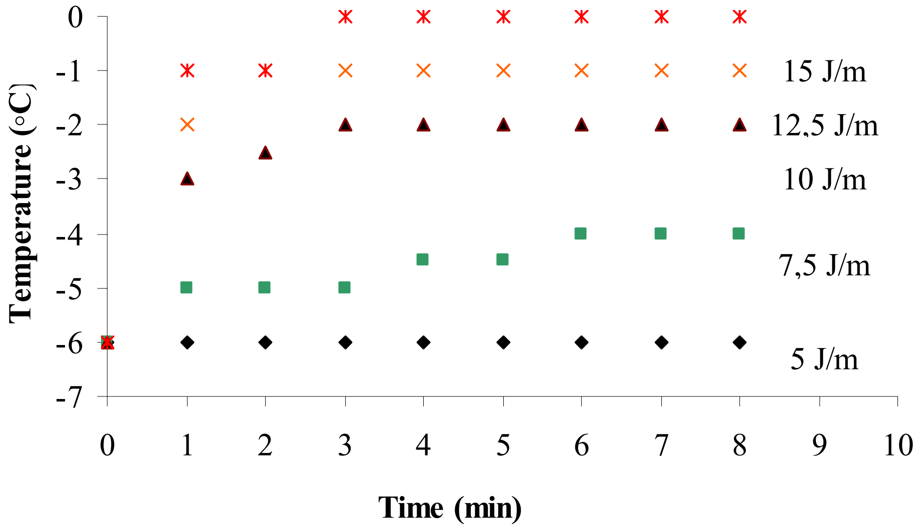

Figure 34: Temperature increase measured by a frozen thermocouple upon continuous scanning of ten adjusted channels scanned on the ice surface under which the thermocouple is frozen. Scans were made with a CO_2 laser beam of 100 mm/s velocity and at 2, 3, 4, 5 and 6% total power (intensities of 5, 7.5, 10, 12.5 and 15 J/m).

The theoretical maximum temperature obtained when channels were continuously marked above the thermocouple with a laser of power 3, 4, 5 and 6% of total power was calculated using equation 20 and is presented in the following table and compared with the experimental maximum temperatures measured with the thermocouple.

Table 1: Comparison between the theoretical average maximum temperatures reached when 10 channels 2 cm long were scanned continuously with a laser power of 3, 4, 5 and 6%.

Power (W)	3	4	5	6
Theoretical Tmax (°C)	-3.2	-2.3	-1.4	-0.5
Experimental Tmax (°C)	-4	-2	-1	0

The theoretical maximum temperature value appeared to be a good estimate of the maximum temperature reached for a continuous scanning of the channel.

3.4.5.4. Continuous scanning of a large open area

The repetitive scanning at increasing powers (from 3 to 6% of total power) of a 6 mm × 6 mm area was performed at 100 mm/s during 2 hours. The temperature was recorded throughout the experiment and the temperature variations are presented in Figure 35. After 2 hours, the measured temperature in the area had reached 50 °C. Little water was left on the thermocouple at the end of the experiment, due to evaporation.

Another experiment was undertaken as a preliminary to cell culture in ice. An area 0.36 mm^2 was scanned since higher temperatures could be achieved inside the melted area than in a single channel scanned at the same laser conditions. However if a single channel was scanned, the temperature would also increase with increasing power.

From the previous results, an increase of about one degree could be expected in a channel if the power was increased by 1%.

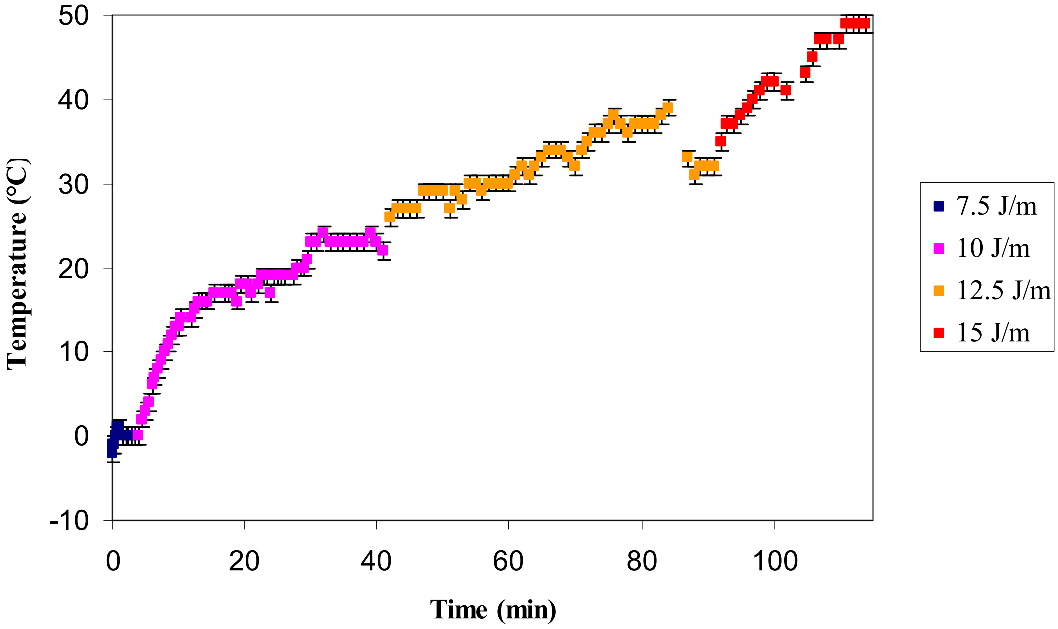

Figure 35: Continuous scanning of a square area of 6 mm × 6 mm with a CO_2 laser beam at 100 mm/sec and 3, 4, 5 and 6 % power (intensities from 7.5, 10, 12.5 and 15 W/m)

3.4.5.5. Single scan of a closed channel

The thermocouple was frozen inside ice made from water at -6 °C. After 6 s a single channel was marked with a CO_2 laser beam at 100 mm/s for various powers. The temperature profile is presented in Figure 36.

This temperature profile is fairly similar to that measured when one open channel was marked at 100 mm/s and 10% of total power. The peak temperature recorded was -3 °C, just as if an open channel was marked with a laser beam at 6% with the same velocity. The power absorbed by the ice was therefore 60% of the value of the laser beam power (β= 0.6).

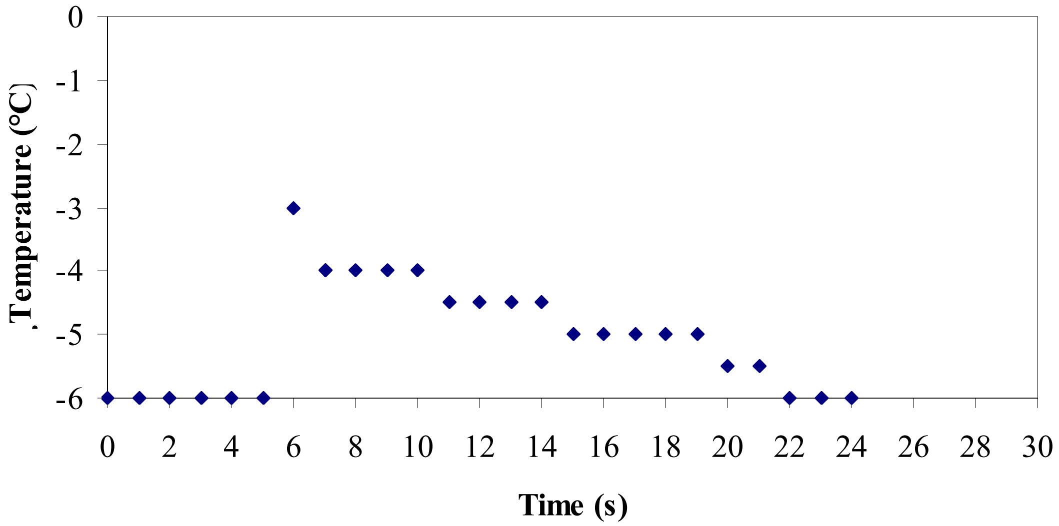

Figure 36: Temperature changes measured by a frozen thermocouple following a single scan of one channel marked by a CO_2 laser beam at 100 mm/s and 10 % of total power.

Equation 39 gave the relation between β and the depth of the melted area based on the peak temperature reached in the channel. Assuming that the transmitted power is equal to zero and for a channel, $A= 2r_bl$ where r_b is the beam radius and l the length of the channel, the depth of the channel was calculated in this case as 120 µm, which is slightly smaller than the depth estimated for an open channel (180 µm) marked at 6% power for a single scan.

The temperature drop is quicker for a closed channel rather than for an open channel. The channel temperature reached the ice temperature of -6°C after t_2 = 16 s instead of t_l = 21 s (Figure 32). The refreeze of the channel is quicker when the ice surface is covered with a cover glass as the cover glass isolates the ice from any natural air convection and also because the overall conductivity of a melted channel covered with a cover glass is higher than for an uncovered melted channel.

The open channel's thermal conductivity was k_l = 0.6 W/mK, its density was ρ_l = 1000 Kg/m3 and its heat capacity was cp_l = 4200 J/KgK. When the channel was covered, the overall properties of the channel could be calculated with equations 43, 44 and 45 became k_2=0.8 W/mK, ρ_2= 1700 Kg/m3 and cp_2=1900 J/KgK when the depth of the channel was taken as 170 μm. From the equation of cooling for ice after a scan (equation 19) for the same absorbed intensity and distance from the beam, the product of the time by the thermal conductivity and the product of the thermal diffusivity by the time should be constant:

$$k_1 t_1 = k_2 t_2$$ **Equation 50**

$$\frac{k_1 t_1}{\rho_1 c_{p1}} = \frac{k_2 t_2}{\rho_2 c_{p2}}$$ **Equation 51**

With he values calculated: k_l t_l- k_2 t_2=0.2 W/m ≈0 W/m while k_l $t_{l/}$ $\rho_l cp_l$- k_l $t_{l/}$ $\rho_l cp_l$= 10^{-6} $m^2 \approx 0$ m^2.

Covered channels made in ice refreeze more quickly than open channels.

3.4.5.6. Continuous scanning of closed channels

Figure 37 represents the temperature increase recorded by the frozen thermocouple when 10 channels were scanned repetitively for 8 minutes (30 scans of each channel) in covered ice, with a laser beam scan rate of 100 mm/s and at 5, 10 and 15% power. The temperature increased linearly during the first 2 minutes of the scanning and reached a maximum temperature which was maintained for the duration of the scanning.

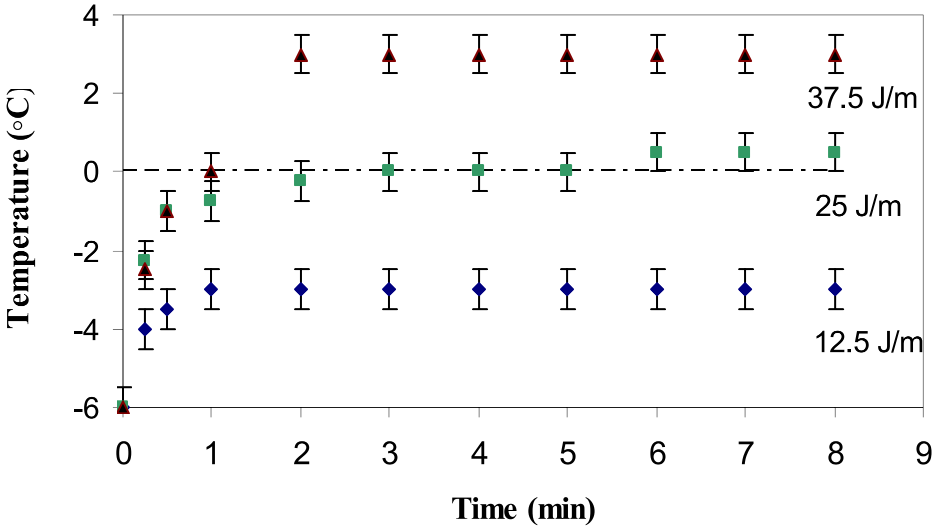

Figure 37: Temperature increase measured by a frozen thermocouple upon continuous scanning of ten adjusted channel scanned in ice covered with a cover glass. The CO_2 laser beam velocity was 100 mm/s and its power was set at 5, 10 and 15% total power (standard error bars).

The ice had an initial temperature of -6 °C. The maximum temperature reached -3 °C for marking at 5%, 0 °C when marking at 10% and 3 °C at 15%.

Just like the scanning of a single scan (section 3.4.5.5), the temperature reached when marking at 10% through the cover glass is similar to the temperature reached when marking open channels at 6%, for the same velocity (100 mm/s). Again the maximum temperature is reached more quickly within closed channels (2 min) than in open channels (3 min) (see Figure 34) due to the higher overall thermal conductivity and diffusivity of the covered channel compared to an open channel.

3.4.6. Measures of the electrical resistance between two electrodes frozen in a conductive solution while scanning channels across them.

3.4.6.1. Scanning of open channels

One channel 27 mm long was marked on a frozen 10 mM HCl solution, crossing the electrodes, using a laser beam velocity of 100 mm/s and at 4, 5, 6 and 7% of total power. The results did not show any significant differences between the different powers at which the laser beam was set; therefore 15 channels 0.5 mm apart from each others were marked in the frozen 10 mM HCl solution across the electrodes with a laser beam at 100 mm/s and 4, 5, 6 and 7% of total power.

The marking was launched at t = 0 s and the 15 channels were scanned in 20.6 s. The Lock-In Amplifier recorded the change in current during first 60 s. The resistance between the electrodes was then calculated. Figure 38 presents the variation in resistance which is the difference between the initial frozen solution resistance and the resistance at time t, versus time.

A decrease in resistance means that the media between the electrodes becomes more conductive and shows that the channels are open. An increase in resistance means that the media between the electrodes becomes less conductive and that the channels are refreezing. When no channels are scanned, the resistance of the ice kept increasing since the ice became denser with time.

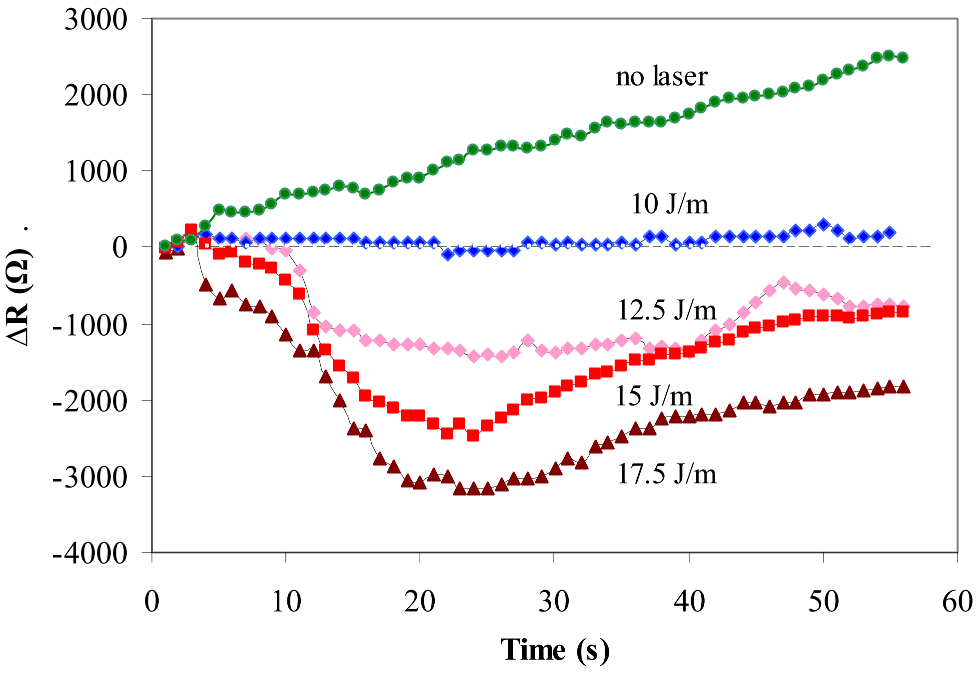

Figure 38: Variation of resistance of ice while scanning 15 channels, 1 scan each, with a CO_2 laser beam at 100 mm/s and at 4, 5, 6 and 7% power: intensities:10, 12.5, 15 and 17.5 J/m and standard deviation of up to 500 Ω.

When the channels were scanned at 4%, the resistance between the electrodes increased slightly (by up to 100 Ω) for the fist 20 s. The resistance decreases to 0 Ω at 25 s and started increasing again after that up to 300 Ω. The marking of channel did not counteract the lowering of resistance induced by ion depletion. The decrease in resistance observed at 25 s was very minimal; the ions in the channels became depleted.

When the channels were marked at 5%, the resistance between the channels also started to increase slightly (by 80 Ω), but after 5 s the resistance decreased to 1500 Ω. After that the resistance increased again. The marking of the channels initially increased the current passing between the electrodes. After 25 s, the resistance was increasing since the ions in the channels were depleting.

When the channels were marked with a laser of 6 and 7% power, the resistance between the electrodes started to decrease immediately. The resistance decreased up to 2500 Ω when the channels were marked at 6% and 3400 Ω when they were marked at 7%. After 25 s, the resistance increased again. The increase is relatively slow but it indicates the depletion of ions in the channels and the refreezing of the channels.

Since the marking of the channels take 20 s to be opened but the resistance decreases until 25 s for most powers, it can be assumed that the channels stay open for at least 5 s after they are open and current is passing through them.

For a single channel scanned at 100 mm/s at 4, 5, 6 and 7% (intensities of 10, 12.5, 15 and 17.5 J/m respectively) in ice made of a dilute (10 mM) HCl solution, the density and thermal properties of which can be approximated to those of water, the channel opening radii are respectively 143, 161, 176 and 190 μm. If the temperature difference between the channel and the surrounding ice reaches 3°C, the theoretical closing time of each channel is 0.5, 0.6, 0.7 and 0.8 s. Without an external electrical circuit applied, the channels should refreeze in less than 1 s after the end of the scanning. However because of the existing electrical circuit and the movement of ions in the channels, in this series of experiment the channels stay open longer (5 s).

The power dissipated in the channels by Joules heating was calculated using equation 49. For all the laser powers it was of the order of 1.5×10^{-7} W. This value is fairly insignificant however it could explain why the channels stay open slightly longer than when there is no current passing through them.

In the next experiment one channel was marked in the frozen 10 mM HCl solution, containing electrodes, with a laser beam with a velocity of 100 mm/s and at 2, 3 and 4 % of total power every 30 s for 5 min and compared with the resistance in non-marked ice. The marking was launched every thirty seconds and lasted 40 s. The Lock-In Amplifier recorded the change in current during the first 5 min. The resistance between the electrodes was calculated from the values of the current recorded. Figure 39 presents the variation in resistance, which is the difference between the initial frozen solution resistance and the resistance at time t, versus time.

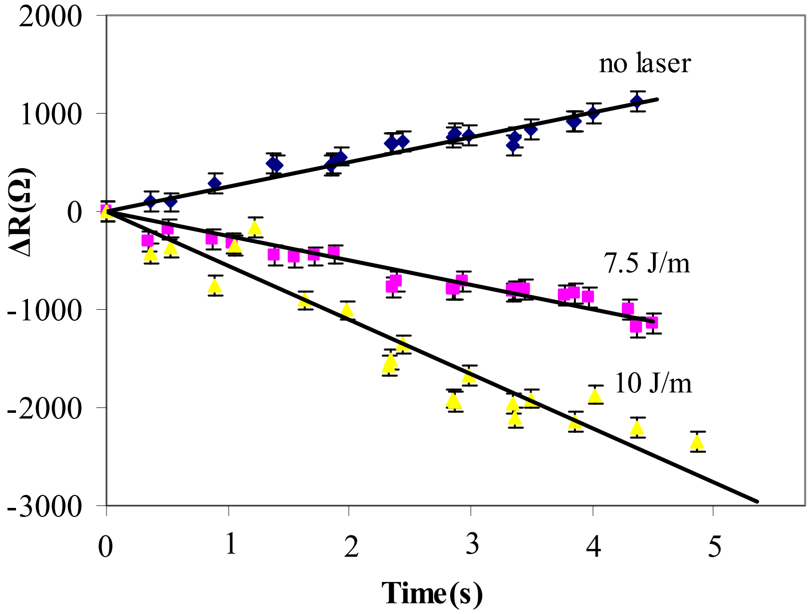

Figure 39: Variation in the electrical resistance of ice (ΔR) when a channel was marked with a laser beam at 100 mm/s and 3 and 4% of total power (intensities of 7.5 J/m and 10 J/m) every 30 s for 5min.

When no channel was marked, the resistance of the ice kept increasing with time. When a channel was marked every thirty seconds with a laser of 3 or 4% power, the resistance between the electrodes decreased linearly with time. The decrease was twice as important when the power was 4%. According to the results of the previous graph, in the presence of an external current a channel stays open for about 5 s. If marking is repeated, each successive freezing and opening of the channels puts more ions in solution and makes the channels conductive for longer.

3.4.6.2. Resistance measurements (closed channels)

15 channels, 27 mm long and 0.5 mm apart from each others were marked on the frozen 10 mM HCl solution across the electrodes with a laser beam at 100 mm/s and 5, 10 and 15% of total power. The marking was launched at t = 0 s and the 15 channels were scanned in 20.6 s. The Lock-In Amplifier recorded the change in current during first 60 s and the resistance between the electrodes was then calculated. Figure 40 presents the variation in resistance which is the difference between the initial frozen solution resistance and the resistance at time t, versus time.

It could be expected that the resistance results obtained for a closed channel marked at 10% would be similar to the one obtained when an open is marked at 6%, however the resistance decreases by 55000 Ω and not by 2500 Ω. When the scan stopped the resistance increased instantaneously and rapidly. Again this shows that the channel closes more quickly when it is covered than when open.

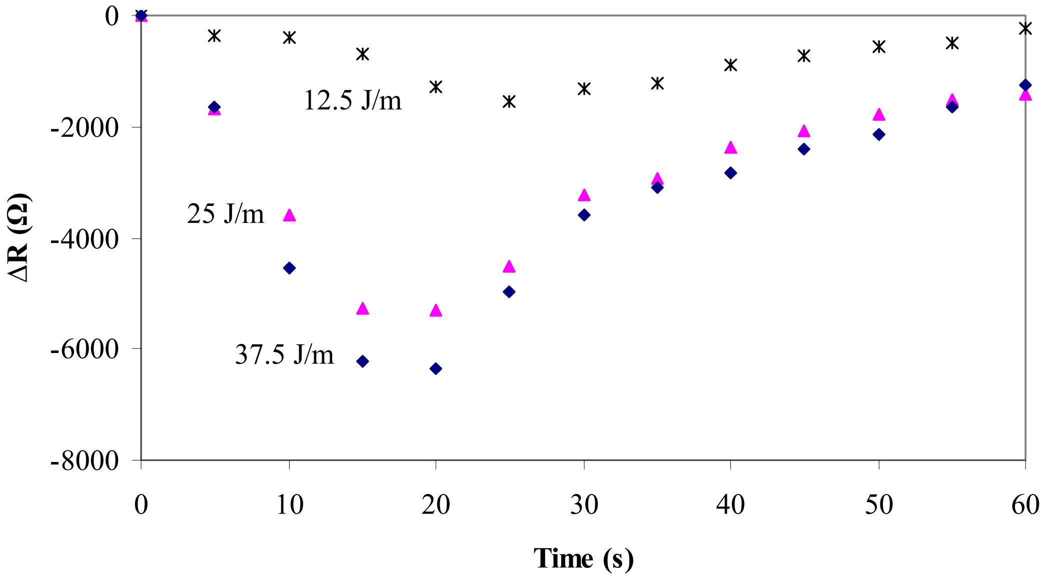

Figure 40: Variation of resistance of ice while scanning 15 channels, 1 scan each, with a CO_2 laser beam at 100 mm/s and at 5, 10 and 15% power: intensities: 12.5, 25 and 37.5 J/m. Standard deviation of up to 500 Ω.

3.4.7. Glass failure

One drawback of the cover glass is its potential fracture during laser scanning. This was observed after successive scanning, especially when scanning spots. Laser induced fracture is not entirely understood since there are many reasons why illumination by a laser beam can damage glass.

One cause of the damage is related to the changes in optical properties of the material, induced by the laser beam, and related to its non-linear refractive index. This index is generally small, but intense laser beams have been shown to be responsible for damages in glass. The critical power above which this damage occurs is given by:

$$Pc = \frac{3.77c\lambda^2}{32\pi^2 n_e}$$ **Equation 52**

where c is the speed of light (2.99×10^8 m/s), λ is the laser wavelength and n_e is the nonlinear refractive index (Hayden, 1995). Borosilicate glass has a non-linear index of of 1.7×10^{-13} esu (Fournier & Snitzer, 1974). The critical power of the CO_2 laser was then calculated as 2.3×10^9 W. The laser used in this application deliver powers lower than the critical power.

However glass heated by a laser beam can also experience thermal stress and can break when the temperature reached within the glass has attained its strain temperature. The strain temperature of the cover glass was 515°C.

From Equation 20 fracture will happen in one scan of laser beam in which the ratio of power to velocity exceeds 99 J/s (i.e. a power of 40% and a speed of 100 mm/s). For repeated scans this critical ratio can decrease to 75 J/s (i.e. power 30% and a speed of 100 mm/s).

For the laser conditions used to mark channels and holes in ice, no fracture should appear. However marking through glass leaves a slight mark on the cover glass, and when repeated, the mark can deepen and eventually break the cover glass which then needs to be replaced.

However it can also be useful to drill holes in the cover glass. In the electrophoresis chapter, 2 mm diameter discs were marked at 40% and 100 mm/s in the cover glass for the purposes of the experiment.

3.5. Conclusions

Channels and various design geometries can easily and rapidly be marked in ice with a CO_2 laser. Within seconds a microchannel pattern can be created. This is a major advantage over the traditional processes used in the fabrication of microfluidic devices, such as photolithography or soft lithography, which demand several lengthier steps to be carried out before obtaining the desired micropatterns.

The dimensions of the channels and cavities required by the micropattern design that can be made in ice with a laser are governed by the ratio of laser power to the beam velocity. Features with dimensions as small as 100 μm were obtained. These dimensions are similar to dimensions obtained with photolithography. However on other substrates laser ablation can result in channels of smaller dimensions: for instance channels 20 μm were marked in PET with a KrF excimer laser of wavelength 248 nm (Kim & Xu, 2003). The difference in dimensions between channels made in ice and channels made in solid substrates is linked to the rapid evaporation of water under laser processing. On the other hand, smaller channels in ice would refreeze very quickly once the marking was finished, which would present a disadvantage for the utilisation of the device.

The channels created in ice stay open for a duration which depend on their geometry and therefore on the ratio of the laser beam power by the beam velocity. After that they refreeze and the micropattern disappears in the ice bulk. This is a unique characteristic to microfluidic devices made in ice and it enables the redirection of flow and the creation of a reconfigurable device within minutes. In a conventional substrate, channels cannot be closed unless an external mean such as a valve or a jet of cryogen liquid and carbon dioxide at -65°C (Bevan & Mutton, 1995) is used to stop the flow inside the existing channel.

To keep ice channels open longer, larger channels can be marked with a laser of higher power/velocity ratio or by successive scanning of the channel. However this can be a drawback, since repeated laser scanning may be incompatible with or alter the microchannel analytes or their mode of operation: for instance DNA or cells present inside the channel would not be viable after laser scanning. In addition visualisation by fluorescence could be affected during the scan. This must be taken into account when using the device.

Microchannels were obtained with a power/velocity ratio between 0.4 and 20 W/m. In this range of settings, the channels were 300 µm wide and stayed open for 2 s. Laser processing in ice was not tested therefore those results cannot be compared to other data.

Transport inside the channel can be obtained by the laser marking process alone. This is caused by the sheer surface tension within the melted area due to the temperature gradient within. The transport observed inside the channels was of the order of 1 mm/s under the laser experimental conditions (1.25 W and 100 mm/s). This was observed in other substrates and is typical of laser operation, however it was never experimented on ice. In stainless steel, for which the Prandtl number is 0.078, velocities of the molten area as high as 14 cm/s with a laser used at power above 40 W were estimated by Cline & Anthony (1977). In conventional microchannels a wide range of flow velocity have been recorded from small values such as 50 µm/s (Santiago *et al.* 1998) or 10 mm/s (Meinhart et al, 1999) depending on the pump type and microchannel dimensions .

The temperature increase in the channel depends on the ratio of the laser power to the velocity. High temperatures (above 50 °C) can be achieved inside ice cavities. Chan *et al.* (1984) showed that temperature rise decreases with the Prandtl number. Up to 40°C temperature rise inside a laser ablated channel were also reported by Stuart *et al.* (1997) who used a Nd:YAG (neodymium-doped yttrium aluminium garnet) laser on enamel, a high Prandtl number substrate. Estimations of very high temperature increases (up to 1400°C) in stainless steel with a CO_2 laser (100W, 500 mm/s) were made by Cline & Anthony (1977).

Channels created in frozen solutions of electrolytes can be observed by conductivity measurements when linked to an electrical power supply. Therefore ice can be a good substrate for electrokinetically driven flow. Also channels stay open longer due to the resulting current.

Channels can be marked in ice through a cover glass. When marking channels at 100 mm/s in covered ice, the laser beam absorbed by the ice is about 60% of the laser power therefore the maximum temperature reached in a channel is similar to that obtained when the channels are open and marked with a laser beam of 40% lower power. The melting and freezing occur more quickly in closed channels rather than in open channels. One drawback of the marking of covered channels is the eventual failure of the cover glass. After a series of repeated scanning, replacement of the cover glass is necessary.

4. Creation of a microfluidic device in ice

4.1. Introduction

Microfluidic devices are self contained systems with injectors, preconcentrators, channels, valves, reactors, analysis processes and detectors.

In the previous chapter it was demonstrated that channels, cavities and various geometries could be easily and quickly created in ice with a CO_2 laser and kept open as long as needed with repeated scans with the laser at proper time intervals. Cavities and other features drilled in ice can be used as injectors, reactors or storage containers while the channels would link the different constituents of the device. In this section we will discuss a laser-operated valve system in ice as well as the possibility of an inline laser induced preconcentration technique in ice.

4.2. Literature

4.2.1. Opening of a valve made of ice

Successive freezing and melting can control and switch fluid flow inside capillaries. This non-invasive technique offers an alternative to the conventional micromachined valves described in section 2. In a first method, freezing of the content of microcfluidic channels was achieved with a fine jet of cryogen liquid and carbon dioxide at -65°C which instantaneously stopped the fluid flow and the electrical current in the channel (Bevan & Mutton, 1995). The melting duration depended on the freezing duration. Gui & Liu (2004) used a thermoelectric cooling device associated with a heat dissipater and an electric heater to freeze and melt the contents of the microfluidic channels involved.

4.2.2. Preconcentration

Microfluidic devices are very attractive tools for sample analysis because of the small sample requirements. Detection is usually performed with high sensitivity detection techniques; however preconcentration of the sample may be needed for some applications. There are various methods available to achieve concentration of samples involving electrophoresis, electroosomosis or filtration (Auroux *et al.*, 2002).

The slow melting and refreezing of a solid, containing impurities, in a narrow zone from one end of the sample to the other can result in the redistribution of those impurities and is known as a purification technique called zone refining or zone melting (Pfann & Olsen, 1952). It was first demonstrated on germanium crystals and can be used on metals, salts and organic or inorganic substances. It was demonstrated for the purification of water (Smith & Thomas, 1959) or ice (Oughton & Xu, 2001).

In 1979 laser beam scanning was used for a first time as a zone melting technique by Nobuo *et al.* and was applied for the purification of crystals frozen inside capillaries. Zone melting with a laser beam can be used for inline preconcentration of different analytes. The efficiency of the process is described by Equation 53 showing the final concentration C reached after one cycle as a function of the initial concentration C_0 (Pfann & Olsen, 1952):

$$C = C_0 \frac{1-(1-k)e^{-k}}{k}$$ **Equation 53**

where k is the distribution coefficient of the species, defined as the ratio of concentration in the solid to that in the liquid at equilibrium.

4.3. Methods

Equipment:

The liquid cooler was the LTD 20 G Grant (Cambridge, Cambridgshire, UK). The laser 1-30 W IR CO_2 Fenix was from Synrad (Mukilteo, WA, USA). The 100 μL capacity analytical syringe was from Scientific Glass Engineering (Melbourne, Australia). The 10 μL capacity analytical syringe was from Hamilton (Rhäzüns/Switzerland). The spectrophotometer USB2000 was from Ocean Optics (Dunedin, FL, USA). The deuterium/halogen light source was UV-VIS-NIR DH2000 from Mikropack (Ostfildern, Germany). The cover glasses were from Menzel-Glaser (Braunschweig, Germany). The micrcuvettes were from Kartell (Noviglio MI, Italy). The optical mirror was from Melles-Griot (Albuquerque, NM, USA). The disposable dishes were from Nunc (Roskilde, Denmark).

Reagents:

Water was purified by reverse osmosis with the Elgastat B224 water purification unit (Elga Ltd, Marlow, Buckinghamshire, UK). The Meldola's Blue dye was from Sigma-Aldrich (Gillingham, Dorset, UK).

4.3.1. Opening of a valve made of ice

It has been anticipated that scanning with a laser can open channels closed by freezing by the same principle as the freezing-melting valves techniques described in section 4.2.1. Channels can be opened with the laser and the channels refreeze and close when the laser is turned off (see chapter 3). In this section a series of experiments was conducted in which only a 1 mm wide area of the channel was closed with ice, in order to determine the time required to melt it and open the channel.

Reservoirs made using a border of PDMS between a glass slide and a cover glass (see Figure 41) were filled with water and fixed onto the cooling system. They were frozen with two tubes made in Polyaryletheretherketone (PEEK) of 1.61 mm external diameter aligned and 1 mm apart. The solution was frozen. The tubes were then removed leaving the mark of two channels in ice. An area of 0.5 mm diameter was scanned above the area separating the channels with the laser at 3, 4, 5 and 7% of total power and a 100 mm/s velocity. One channel was connected to a micropipette filled with Meldola’s Blue. The time required to melt the ice and to pass dye from one channel to the other was considered as the “opening” time for the channels and recorded for each power.

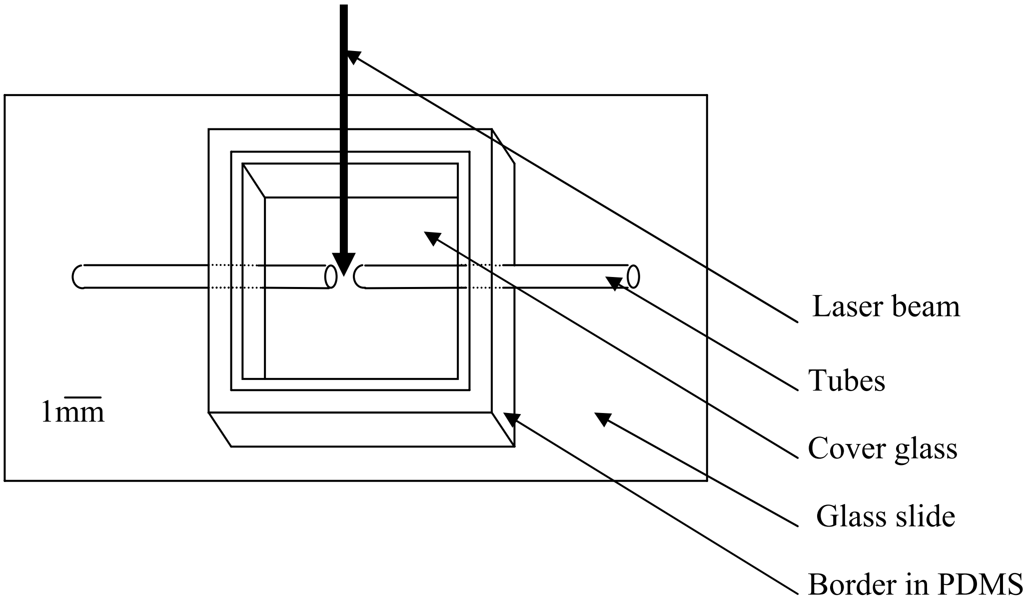

Figure 41: Melting of a 1 mm ice area between two channels.

4.3.2. Spectroscopy detection of a dye in ice capillaries

The concentration of analytes in ice channels and cavities was detected with a fibre optic reflection probe. The probe is linked at one end to the Ocean Optics USB2000 spectrophotometer connected to a Windows XP PC via USB and to the other end to a halogen light source (see Figure 42). As a model analyte we chose the dye Meldola's Blue.

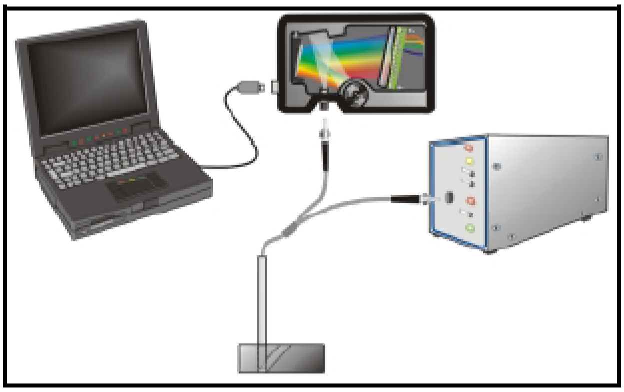

Figure 42: Spectrophotometer set up.

The measure of the absorbance at a given wavelength is the measure of how much light the sample absorbs at that wavelength. It is proportional to the concentration of the substance interacting with the light as given by the Beer-Lambert law:

$$A_\lambda = \varepsilon_\lambda c l \qquad \textbf{Equation 54}$$

where A_λ is the absorbance at wavelength λ, c is the concentration in moles per litre, l is the path length in centimetres, and ε_λ is the molar extinction coefficient of the absorbing species at wavelength λ.

To determine the absorbance of a sample with the USB spectrophotometer, a measure of the dark intensity, which is the intensity when the lights is switched off, must be taken as well as a measure of a reference sample intensity. When the sample intensity is recorded, OOIBase32 calculates the absorbance using the following equation:

$$A_\lambda = -\log\left(\frac{S_\lambda - D_\lambda}{R_\lambda - D_\lambda}\right) \quad \textbf{Equation 55}$$

where S_λ is the sample intensity at wavelength λ, D_λ is the dark intensity at wavelength λ and R_λ is the reference intensity at wavelength λ.

The set-up described in Figure 42 was used to demonstrate the ability to measure the concentration of aqueous solutions of Meldola's Blue. The probe was placed perpendicularly at 2 mm from the side of the mircrocuvettes containing solutions of Meldola's Blue of various concentrations. A mirror was placed behind the micro cuvettes to reflect the incident light. Water was used as control. The absorbance of the solution was calculated by the OOIBase32 software. The maximum absorbance at Meldola's peak wavelength (570 nm) was recorded for each concentration.

In capillaries the dye concentration was measured using the same set-up. Ice was frozen inside dishes 3.3 cm diameter and 1.5 cm high. The height of the liquid was 1 cm. A mirror was placed under the dishes. 4 channels were marked with the laser (30 scans each, 4 %, 100 mm/s) and 10 µL of Meldola's Blue was injected inside the channel with a Hamilton syringe. The optical probe was placed above the dye in the channel and absorbance measurements were taken. Water was used as control. The maximum absorbance at 570 nm was measured.

4.3.3. Preconcentration

4.3.3.1. Distribution coefficient of Meldola's blue

To determine the distribution coefficient k of Meldola's Blue, 2 mL of 0.015 g/L Meldola's Blue were frozen in a dish placed onto the cooling device while an area of 2 mm diameter was scanned continuously (4 %, 100mm/s, one scan every 30 seconds). The area illuminated was kept melted while the surrounding froze (Figure 43). The optical probe was placed above the dye in the illuminated area. The absorbance at 570 nm was measured. Water was used as control. Measurements of the absorbance in the area scanned were performed until the area surrounding the 2 mm disc was frozen.

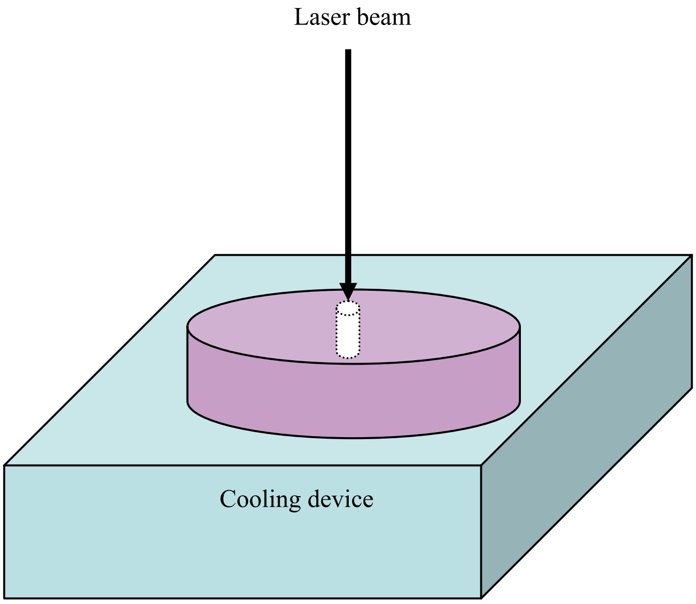

Figure 43: Illumination of a 2 mm diameter area by the laser beam upon freezing of the surrounding area.

4.3.3.2. Laser zone melting in a ice channel

2 mL of 0.015 g/L Meldola's Blue were frozen inside a Petri dish and placed on top of the cooling platform, while a travelling melting zone of 1.5 mm x 1.5 mm was

illuminated with the CO_2 laser at 6% power, 150 mm/s beam velocity and 25 scans. The travelling molten zone was scanned over an area of 7.5 mm x 1.5 mm. One cycle of travel of the molten zone in the area lasted 15 minutes.

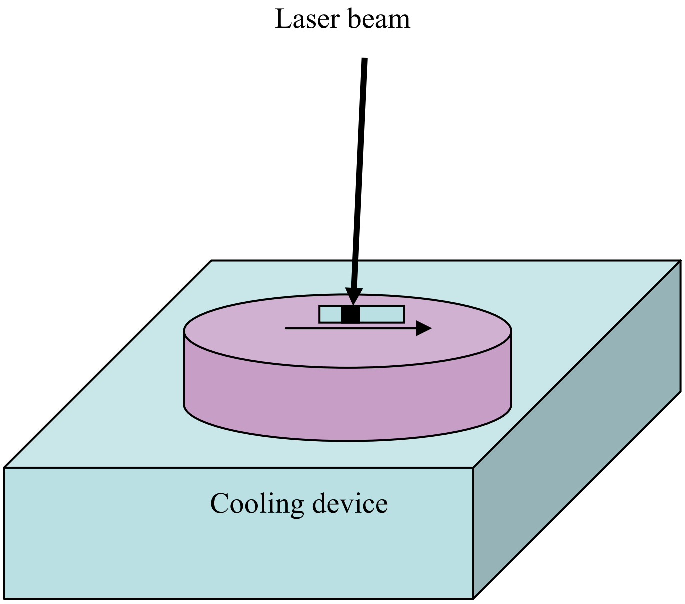

Figure 44: Schematic diagram of the progression of the molten zone in the sample by laser illumination.

4.4. Results and Discussion

4.4.1. Opening of a valve made of ice

The time at which the 1 mm wide ice area separating two channels melted was recorded for different laser powers. A spot 0.5mm diameter was marked between both channels with the CO_2 laser at 3, 4, 5, 6 and 7% of the total power and a 100 mm/s velocity. The time of opening was recorded and plotted against the laser power (Figure 45).

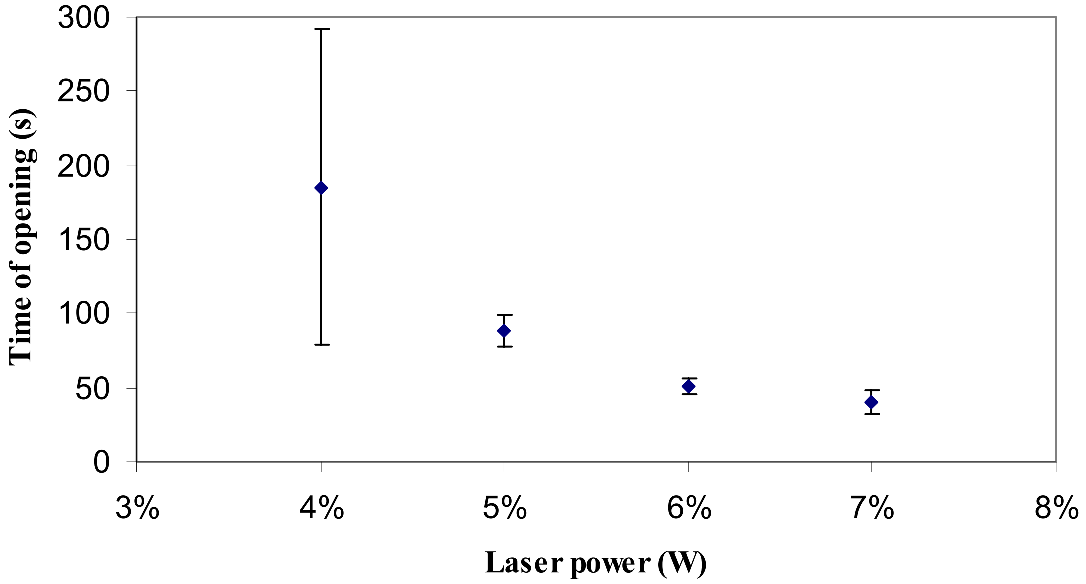

Figure 45: Melting time of a 1mm wide ice section separating two channels with standard deviation bars.

Laser powers above 3% were needed to melt the ice. The time of opening decreased from 185 s to 40 s when the laser power increased from 4 to 7%.

As shown in section 3.2.1.2, the power of the laser beam is related to the energy Q absorbed by the ice to melt over time. The power was then plotted against the inverse of time for the values measured (Figure 46).

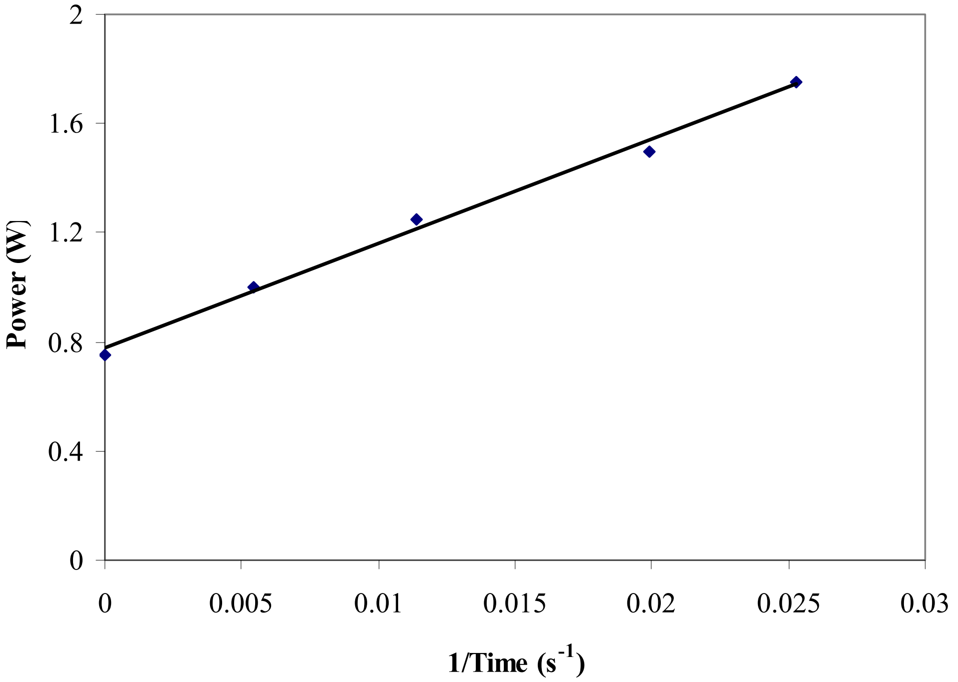

Figure 46: Laser power versus the inverse of the time of opening.

The plot of the power versus the inverse of the melting time can be approximated to a straight line (R^2 = 0.994). The slop of the plot of the power of the laser beam can therefore be estimatived as $\frac{Q}{\beta}$ where β is the coefficient between the laser power and the power absorbed by the ice (see section 3.2.2). From the value of the slope, β was calculated as 0.66, which coincides with the value calculated in 3.4.5.5.

The dye contained in one of the channel flowed through the opened cavity when the ice area separating the channels was melted. After the laser beam stopped illuminating the area, the gap refroze in two minutes. The time of refreeze was independent of the laser power and velocity of marking of the cavity since it only depends on the cavity dimensions.

The opening-closing times can be substantially shortened for smaller channel dimensions in microfluidic devices. This technique can be a useful tool for opening channels in a microfluidic device. The opening of the area depends only on the power and the speed of the laser.

4.4.2. Spectrophotometry

4.4.2.1. Calibration plot of Meldola’s Blue in solution

Concentrations of Meldola’s Blue inside the ice were measured with a fibre optic probe. A calibration plot of the absorbance of Meldola’s Blue in solution was established for the USB spectrophotometer used with the reflection optical probe. The absorbance peak at Meldola’s peak wavelength (570 nm) was recorded for various concentrations (Figure 47).

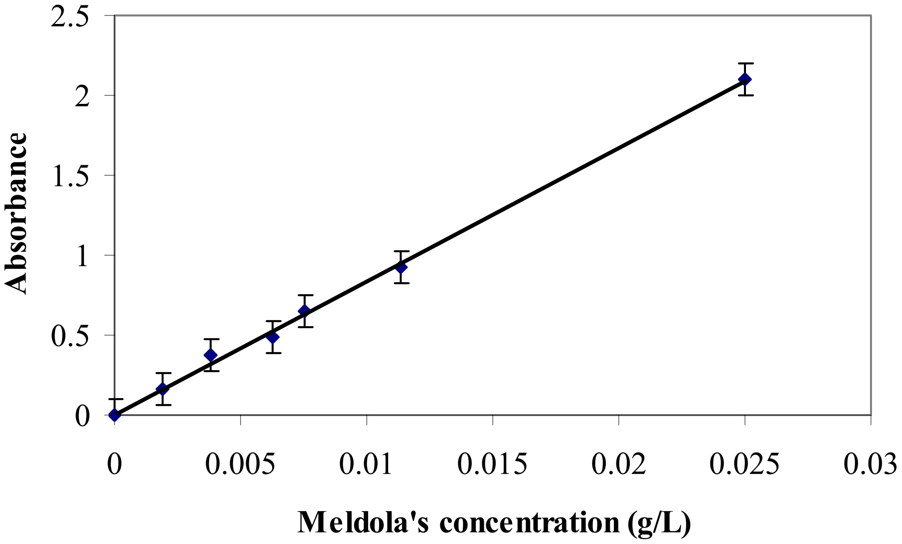

Figure 47: Absorbance calibration for Meldola's Blue solutions (at 570 nm) performed using Qmicro-R200-7-UV/VIS-BX reflection probe and the USB2000 spectrophotometer.

The measurements were compared with the maximum absorbance measured at 570 nm with a traditional spectrophotometer. The results are similar (within 10%) showing that the probe can be used effectively to measure the absorbance. The reflective probe is very sensitive and some stray light may cause the slight difference. Performing the experiments under the same conditions assures the repeatability of the measurements and the adequacy of the calibration plot for further use.

4.4.2.2. Absorbance of Meldola's Blue in ice channels

The purpose of the reflection probe is to detect dye in ice, a calibration of absorbance of the frozen dye at various concentrations inside the ice channels was therefore established. The measurements of the maximum absorbance measured at 570 nm by the reflection probe when 10 µL drops of dye were injected inside ice channels are shown in Figure 48.

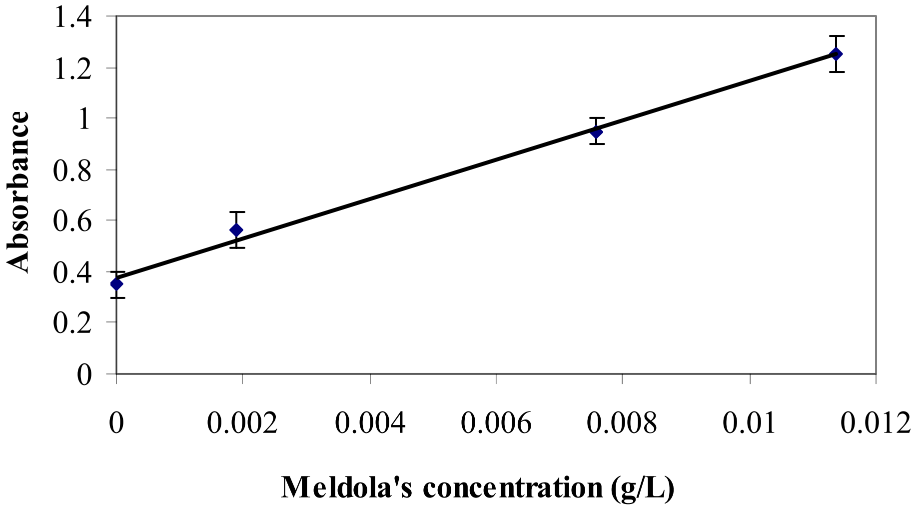

Figure 48: Absorbance of Meldola’s Blue dye drops inside channels marked in ice at 570 nm. Measurements were performed with the Qmicro-R200-7-UV/VIS-BX reflection probe and the USB2000 spectrophotometer.

The slope of this graph is within 5% of the slope of the calibration plot shown in Figure 47. The absorbance measure in the absence of Meldola’s Blue had a value of 0.4. From the values of the absorption coefficient given by Johari (1981), the absorbance of ice at this wavelength should be in the range of 0.02. In order to understand why the initial absorbance was not equal to zero, measures of the absorbance of water during freezing were undertaken in the same conditions with the reflective probe. The results are shown in Figure 49.

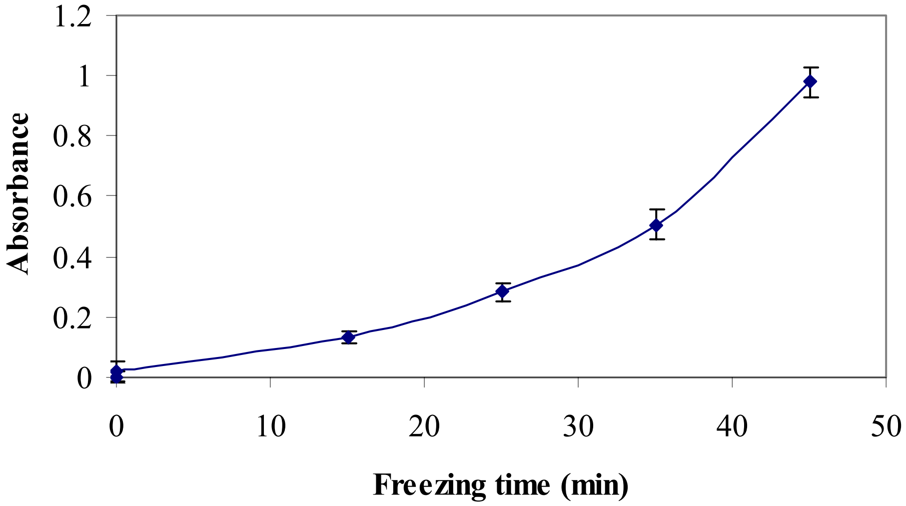

Figure 49: Changes in ice absorbance at 570 nm during freezing.

Ice crystallisation and increased strength of the hydrogen bonds are responsible for an increase in the absorbance at 570 nm observed during the freezing process. In the liquid state, water molecules vibrate but as rigid ice crystals form those vibrations are more and more restricted, resulting in a higher absorbance of solid ice by comparison with the absorbance spectrum of liquid water (Ewing *et al.*, 2003).

The linear expansion was also monitored during freezing. The results are shown in Figure 50.

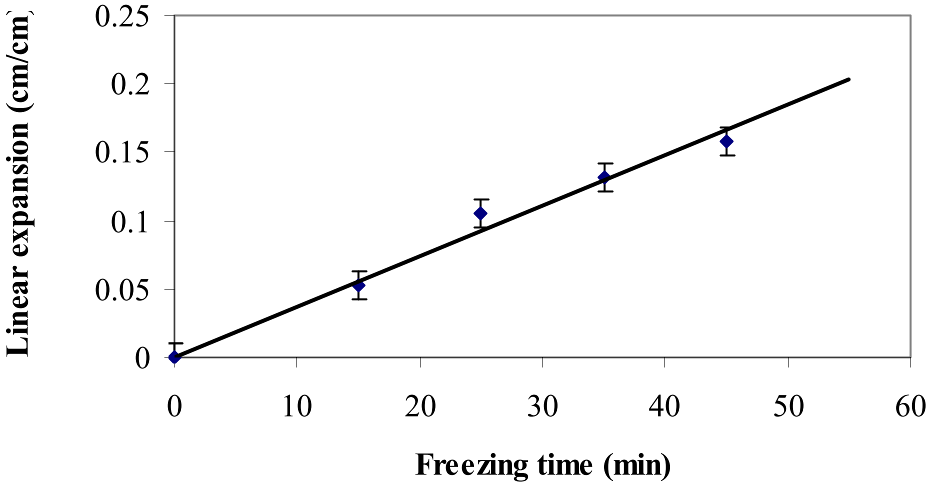

Figure 50: Linear expansion measured during freezing of water inside dishes.

The measures shown in Figure 48 were taken on samples frozen after 30 min, the thickness of ice had increased by 0.12 cm and the absorbance by 0.2%. The linear expansion of ice upon freezing cannot explain the high values of absorbance measured in ice with the reflection probe when no Meldola's Blue was present. However for samples analysed at the same freezing conditions, it was possible to accurately determine the concentration of dye in frozen solution with the absorbance calibration plot given in Figure 48.

4.4.3. Preconcentration

4.4.3.1. Distribution coefficient

The absorbance of Meldola's Blue in the melted area was measured upon freezing of the surrounding area which took 40 min. From the calibration plot of absorbance versus calibration realised for Meldola's Blue with the reflection probe

(Figure 47) the concentration in the melted area was calculated and was plotted in Figure 51:

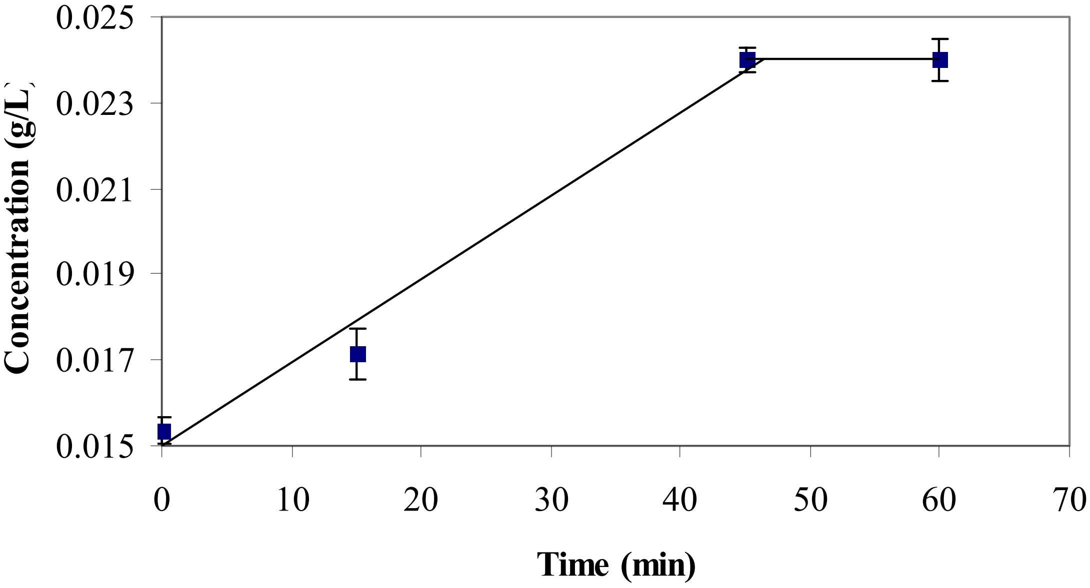

Figure 51: Change in concentration of dye in the melted area during freezing of the surrounding zone (standard deviation bars).

The concentration in the melted area increased with time until it reached the value of 0.023 g/L. The area illuminated was 2 mm diameter while the dish was 3.3 cm diameter. The solution was 1 cm high. The distribution coefficient of Meldola's Blue was then calculated as 0.6.

4.4.3.2. Laser zone melting in a ice channel

A travelling melting zone of 1.5 mm x 1.5 mm was scanned at 6% power and 150 mm/sec with 25 scans over an area of 7.5 mm x 1.5 mm. One cycle of travel of the melting zone in the area took 15 minutes. In the last region of the melting zone travel the absorbance at 570 nm was measured after each cycle. The concentration at the end of each cycle was deduced and was plotted in Figure 52 together with the theoretical values calculated with Equation 53 with a value of k of 0.6.

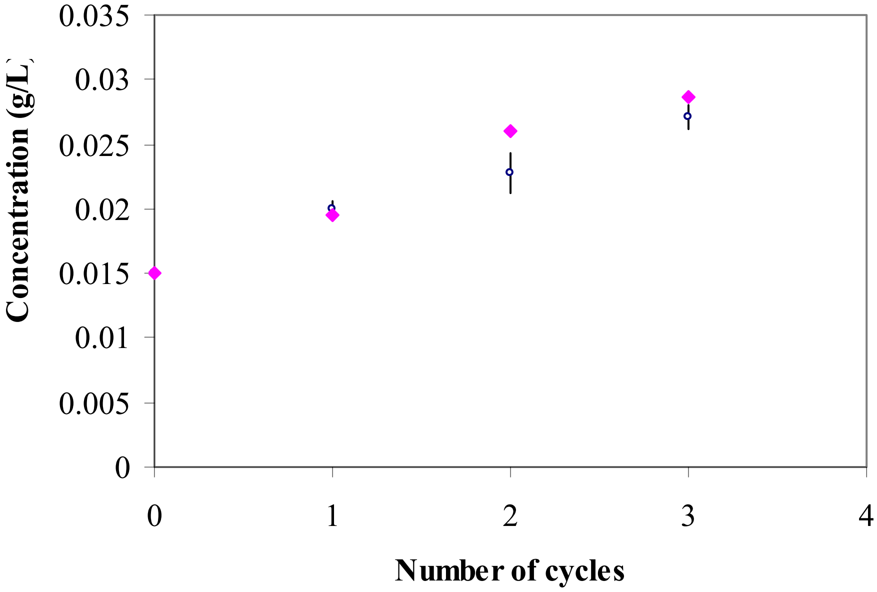

Figure 52: Experimental (squares) with standard deviation bars and theoretical (pink) concentrations of dye in the final part of the travelling melting zone after 1, 2 and 3 cycles in ice.

The results show that the concentration of dye in solution increased linearly with the number of cycles. The difference between the experimental and the theoretical concentration values was within 10 %.

This experiment shows that the concentration of Meldola's Blue increased during laser zone melting. The laser coupled with freezing can be used for preconcentrating samples inline in a microfluidic device created in ice.

4.5. Conclusions

The freezing and melting of ice can be used as a valve technique for microfluidic systems. The opening of the area depends only on the power and the speed of the laser while the closing time by freezing depends on the cooler devices set temperature. This non-micromachined valve can be used on an ice microfluidic device. However compared to the non-intrusive ice valves of Bevan & Mutton (1995) or Gui & Liu (2004) the laser beam can be damaging to the content of the channel (e.g. cells, or DNA). This method could however be employed in laser resistant material microchannels such as the one developed by Laptewicz & Bauer (1985) made of graphite in a polymer matrix.

The preconcentration of analytes in ice microfluidic devices by laser-assisted zone melting has been demonstrated using Meldola's Blue as a model analyte. It consists of concentrating the analyte molecules at the end of the travelling melt zone and is achieved after successive cycles of zone travelling in ice. This technique can be used in an ice microfluidic device for inline sample preconcentration for both sensing and separation purposes. This purification and concentration method is however slow and necessities numerous cycles of scans of the travelling zone and can be a drawback for a fast utilisation of the device.

5. Electrophoresis in channels in ice

5.1. Literature review

Electrophoresis is a separation technique which is based on the differential velocities of charged ions in an electric field. It was discovered by Reuss in 1807 when he observed the migration of water towards the cathodes through clay particles. In 1870 Helmoltz related the flow parameters of electrokinetic transport to the electric field. There are two main types of electrophoresis techniques: electrophoresis in free solution and electrophoresis on a support media.

Moving boundary electrophoresis in free solution was tested by Tiselius in 1937 on a protein mixture in a buffer solution which under an electric field flowed in a direction determined by the current and at a rate determined by their charge and mobility. His work was rewarded with a Nobel price in 1948. Hannig (1982) developed the free flow electrophoresis technique in which a continuous stream of buffer flows perpendicular to the electrical field for the separation and identification of parasites. This technique is very effective and can separate particles with minimal differences in their surface charges.

Electrophoresis on a support was developed as a way of monitoring the progression of the mixture and to visualise the separated components. This principle is called zone electrophoresis. Kunkel & Tiselius developed a filter-paper electrophoresis method in 1952. Agarose gel is another common support of zone electrophoresis (Hjerten, 1961) used in biochemistry and molecular biology for the separation of DNA molecules in which the shorter DNA fragments move faster than longer ones.

Convection in the electrophoretic media or adsorptive interactions between the solute and the support can take place and create zone broadening. Zone electrophoresis was then developed in microcapillaries to increase heat dissipation through the surface of the capillaries and minimize zone broadening (Jorgenson & Lukacs, 1981). Capillary electrophoresis (CE) is carried out in 20 to 30 cm long columns with an internal diameter of 50 to 200 μm. The separation can be detected with the instrumentation already developed for high performance liquid chromatography. Microchip CE can be used for the analysis of nucleic acids and proteins, genotyping and DNA sequencing. These techniques have considerably accelerated the sequencing of the human genome (Luckey *et al*, 1990). The analyses are very rapid: less than a minute for oligonucleotides (Effenhauser *et al*, 1994) to 20 min for DNA sequencing (Liu *et al*, 1999).

5.1.1. Electrophoresis separation

The velocity v of an ion migrating in the electrical field E (V/m) is given by the expression:

$$v = \mu_e E \qquad \textbf{Equation 56}$$

where μ_e is the electrophoretic mobility (m^2/Vs).

The ion inside the applied current is subject to an electric force F_e and the frictional force F_f. The electrical force can be expressed by:

$$F_e = qE \qquad \textbf{Equation 57}$$

where q is the charge of the ion (C) while the frictional force for a spherical ion of radius r can be expressed by:

$$F_f = 6\pi\eta r v \qquad \textbf{Equation 58}$$

where η is the viscosity (Ns/m^2).

The ion moves in the field with a constant velocity, therefore the electric force and the frictional force acting on the ion have same value. The mobility is therefore given by:

$$\mu_e = \frac{q}{6\pi\eta r} \qquad \textbf{Equation 59}$$

Ions of high charge and of small size have high mobility.

In conventional capillaries, the motion of ion also arises from an electroosmotic flow within the capillary which depend strongly upon the composition of the capillary. The overall mobility of an ion is then:

$$\mu = \mu_e + \mu_{eof} \qquad \textbf{Equation 60}$$

where μ_{eof} is the electroosmotic mobility (m^2/Vs).

5.1.2. CE on microchips

In 1992, Manz *et al*. presented the first CE on a microchip where injection, sample manipulations and separation took place on the microfluidic device. Because of the short separation length, the microchip CE is quick (within minutes if not seconds) and without significant peak broadening. The other advantage of microchip CE is the micro amount of sample needed.

Glass and polymers are the two main types of substrates for capillary CE on microchips. In those substrates, the electrical field applied can be very high, of the order of KV/cm (Seiler *et al*, 1993). Microcapillaries have high electrical resistance, therefore the amount of heat generated by the high electrical field is modest and readily dissipated through the walls of the capillary. The use of high electrical currents in microchip CE also leads to shorter separation times and higher separation efficiency compared to traditional electrophoresis systems, since the efficiency of separation is highly dependant on the electrical field applied, as shown by the expression of the separation efficiency:

$$N = \frac{\mu E}{2D} \qquad \textbf{Equation 61}$$

where D is the diffusion coefficient of the migrating species.

The resolution of the separation is defined as the ratio of the distance between sample peaks (ΔL) and the standard deviation of the sample zone (σ):

$$R = \frac{\Delta L}{\sigma} \qquad \textbf{Equation 62}$$

5.1.3. Instrumentation

The length of the separation channel is limited by the sample plug length. If needed the size of the channel can be increased: serpentine capillaries as long as 50 cm were fabricated on chips as small as 1 cm^2 (Seiler *et al*, 1993).The depth of the capillaries is usually 15 to 40 µm and their width 60-200 µm (Jacobson *et al*, 1994). CE microfluidic designs can be as simple as a single microchannel to more complex arrays of microchannels (Woolley *et al*, 1997). The later can offer the analysis of a large number of samples simultaneously. The number of channels on one device can however be limited by the size of the substrate, the detection method and the channel geometries and requirements (Dolnik *et al.*, 2000).

Samples are loaded inside reservoirs and injected electrokinetically into an injection channel orthogonal to the separation channel as shown on Figure 53. A high voltage is then applied along the separation channel and it induces migration of the sample and separation to occur. The electrokinetic injection of sample controls the volume of sample injected in the separation channel (Harrison, 1992).

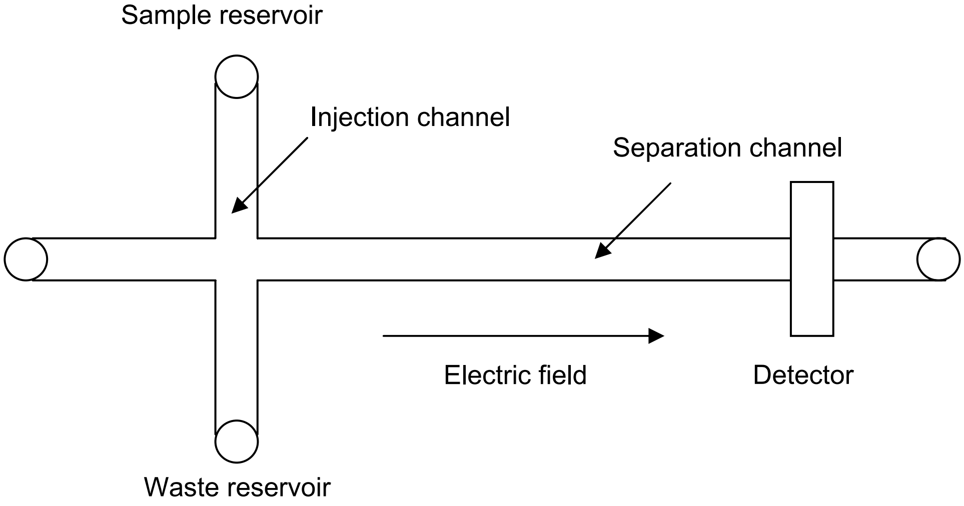

Figure 53: Schematic view of an electrophoretic separation system on a micro-chip

Detection is mainly achieved by laser-induced fluorescence, a detection method of high sensitivity. Laser-induced fluorescence can detect quantities as small as 10 yoctomoles (10×10^{-24} moles) (Da Yong *et al*, 1994). While its sensitivity is very high, the laser-induced fluorescence detection system is very large. Other detection systems were developed for capillary electrophoresis to address this issue: electrochemical detection (Gavin & Ewing, 1996) and mass spectrometry (Zhang *et al*, 1999).

5.1.4. Ice as a separation substrate

Electroseparation inside ice has been demonstrated by Piletsky *et al*. (2002). A glass capillary was filled with 10 mM HCl frozen at -20 °C. When a 10,000 V potential was applied, part of the capillary melted to let through a current of 0.2 µA. A mixture of amino acids and peptides was separated in the ice-filled capillary. Immunoglobulin can also interact with their corresponding antibodies whilst frozen inside ice (Piletsky *et al*., 2002).

These results clearly indicate that ice can work as a separation matrix and that ice capillaries could offer improved compatibility with proteins or nucleic acids compared to polymer microstructures. This leads to the idea of creating ice channels for separation and sensing by capillary electrophoresis. Channels can be created inside ice with a CO_2 laser as described above and refrozen and reformed as needed.

Attempts at electroseparation performed in channels made inside various frozen media (gels, polymers and solutions) are presented in this section. They were also compared with electroseparation in polymeric substrates under the same conditions.

5.2. Materials and Methods

Equipment:

The liquid cooler was the LTD 20 G Grant, (Cambridge, Cambridgshire, UK). The electrophoresis power supplies were the Consort 3000V-300mA E833 (Turnhout, Belgium and the EPS 301 from Amersham Biosciences, Little Chalfont Buckinghamshire, UK. The platinum electrodes (product number 26720-1, 99.99 % purity) were from Sigma-Aldrich (Gillingham, Dorset, UK). The laser 1-30 W IR CO_2

Fenix™ was from SYNRAD (Mukilteo, WA, USA). The 100 µL capacity analytical syringe was from Scientific Glass Engineering (Melbourne, Australia). The microscope/camera Digital Blue was from Digital Blue (Heckmondwike, West Yorkshire, UK). The CCD camera was the pinhole B/W CCD board Camera from RS components (Corby, Northamptonshire, UK) used with the Adaptec AVC 1100 Video Capture software (Milpitas, CA, USA). The UV light was the Mineralight lamp model UVG54 from Ultraviolet Prod. INC (Upland, CA, USA). The spectrophotometer USB2000 was from Ocean Optics, (Dunedin, FL, USA). The halogen light source was UV-VIS-NIR DH2000 from Mikropack, (Ostfildern, Germany).

Reagents:

Acrylamide, methacrylic acid (MAA), acrylamidomethylpropansulfonic acid (AMPSA), methylene bisacrylamide, Rhodamine B, Bromocresol Green and Meldola's Blue were from Sigma-Aldrich, (Gillingham, Dorset, UK). Ammonium persulphate (APS) was from Fisher Scientific UK (Loughborough, Leicestershire UK), *N*,*N*,*N*,*N*-tetramethylethylendiamine (TEMED), tris(hydroxymethyl)aminomethane, 2-propanol, dichlorodimethylsilane, methanol, hydrochloric acid (HCl) and acetic acid were from Acros Organics (Geel, Belgium). N-octane was from VWR, West Chester, Lutterworth, Leicestershire, UK The silicone elastomer 2-compound system QSil215S was from ACC Silicones (Bridgwater, Somerset, UK). The heat sink compound and the quick set epoxy adhesive were from RS components (Corby, Northamptonshire, UK). Water was purified by reverse osmosis with the Elgastat B224 water purification unit (Elga Ltd, Marlow, Buckinghamshire, UK).

5.2.1. Capillary T-junctions in Perspex

5.2.1.1. Millimetre T-junction

A T-junction (800 µm width) was drilled in Perspex at 50 % power, 150 mm/s Figure 54). The channels were 0.8 mm width and 26 mm long with the exception of the separation channel which was 1.8 mm long. The electrodes were inserted into the cavities designed to fit them.

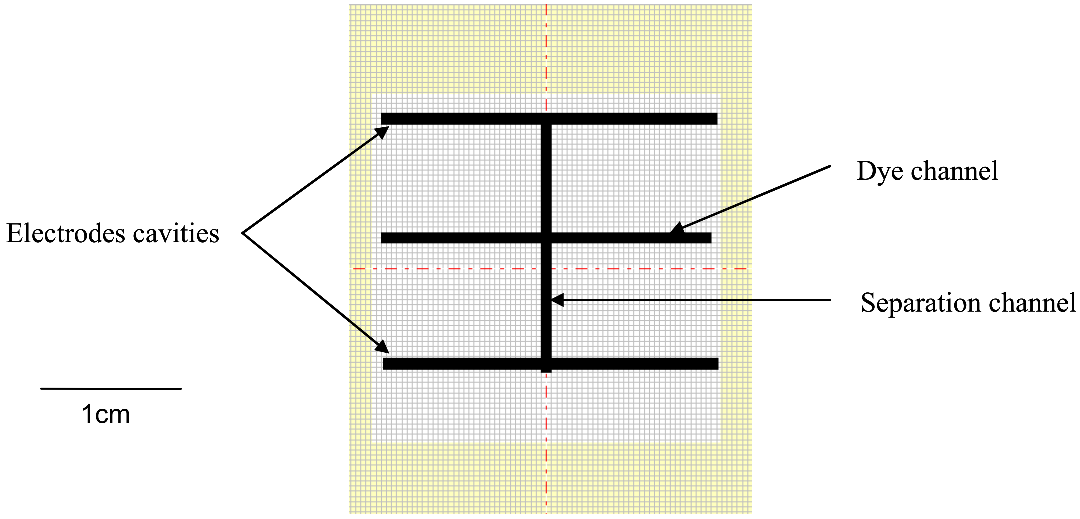

Figure 54: Design of the millimetre T-junction using Winmark software

5.2.1.2. Micro capillary T-junction

A micro capillary T junction (100 µm width channel) was drilled in Perspex at 50% power, 150 mm/s with the laser as shown in Figure 55. Two platinum electrodes were placed in 0.8 mm width, 26 mm long channels 2 cm apart. The dye and the separation channels were 100 µm wide. The separation channel was 1.8 mm long. The electrodes were as previously inserted into the specifically designed cavities.

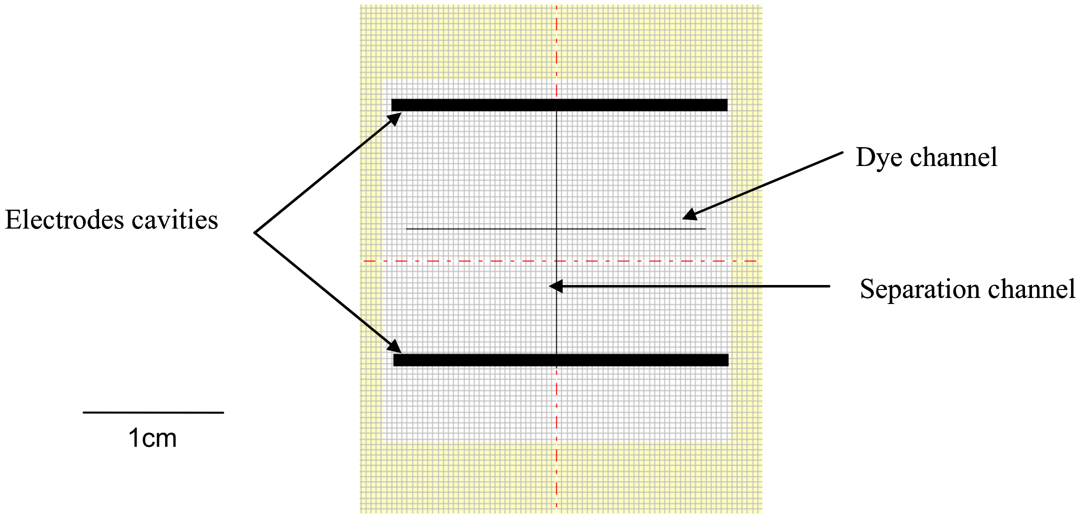

Figure 55: Design of the micro capillary T-junction using Winmark software

5.2.2. Cassettes

5.2.2.1. Cassette A allowing a specific area to be frozen.

The area of solution to be frozen in this cassette was delimited by the dimensions of an aluminium stage: 0.4 cm high, 2 cm width and 8 cm long. The aluminium stage was mounted onto a plastic plate (7.5 cm × 12.5 cm) with an aperture of the dimension suitable for the fitting of the aluminium stage (2 cm × 8 cm). A heat sink compound was rubbed into that plate. A plastic cassette (5 cm × 7 cm) was placed on top of the aluminium and the bigger plate as shown in Figure 56. The two platinum electrodes were glued onto that cassette, 4 cm apart from each other, with quick set epoxy adhesive. They were positioned to remain in the unfrozen part.

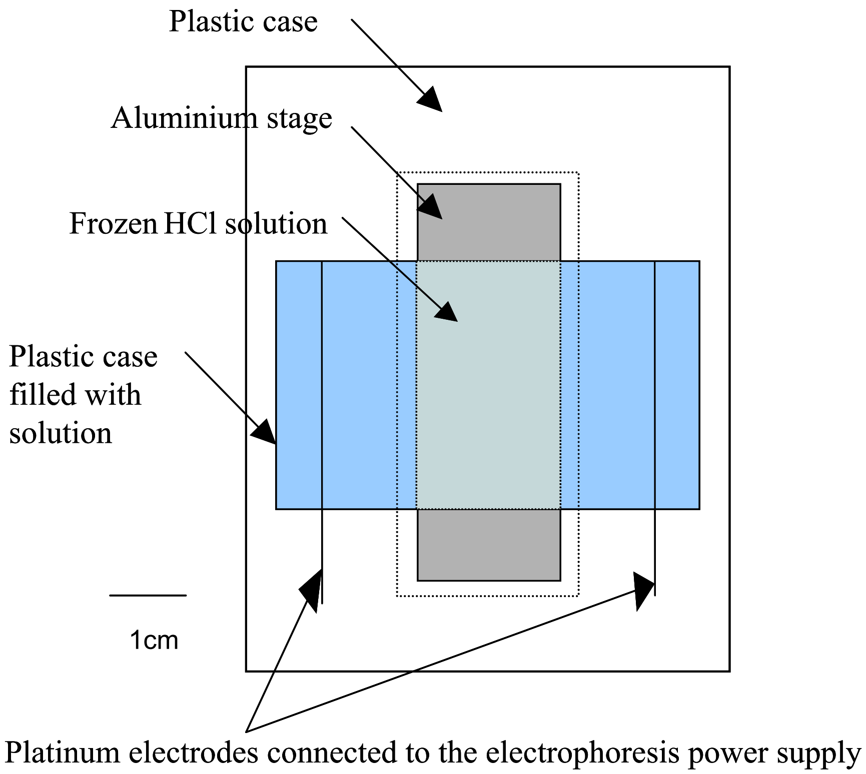

Figure 56: Schematic representation (top view) of Cassette A

5.2.2.2. Cassette B with masked electrodes

In order to define and precisely locate the region for the application of current and to allow the supply of electrophoretic solution for electrophoresis, the platinum electrodes were entirely masked except of a 4 mm area by insertion inside PEEK tubes of 0.5 mm interior diameter provided with a 4 mm aperture on their side. The apertures enable fresh electrophoretic solution buffer to be supplied for electrophoresis.

The two platinum electrodes inserted in the PEEK tubes were fixed 1.5 cm apart into a Petri dish as shown in Figure 57. They were passed through 1.5 mm holes in the Petri dish and fixed with epoxy glue.

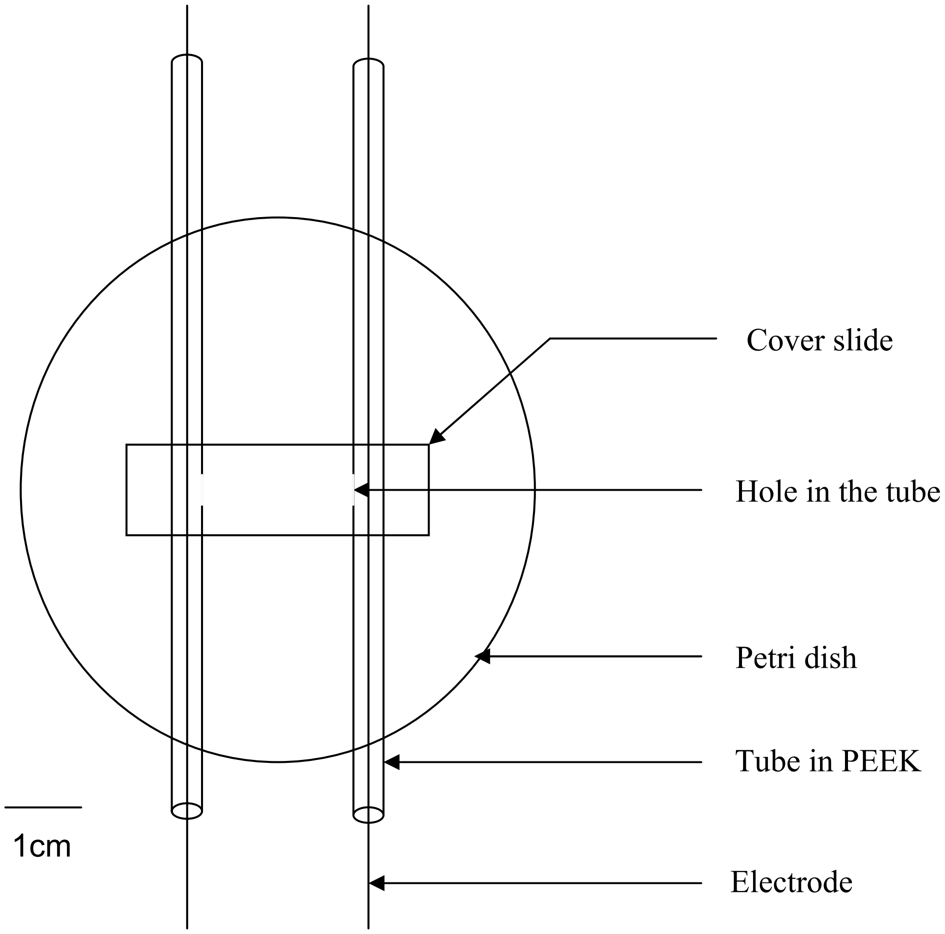

Figure 57: Schematic representation of the Cassette B

5.2.2.3. Cassette C

Cassette C was formed by a 2.4 cm × 2.4 cm × 2 mm frame made of PDMS attached onto a glass slide with epoxy glue and covered by a cover glass. To create the frame in PDMS, a mould of the frame as shown in Figure 58 was drilled into Perspex with the laser (150 mm/s, 50 %, 2 scans). The QSil215 silicone elastomer 2-compound system was mixed in the ratio of 1:10, poured into the mould and allowed to harden for 2 hrs.

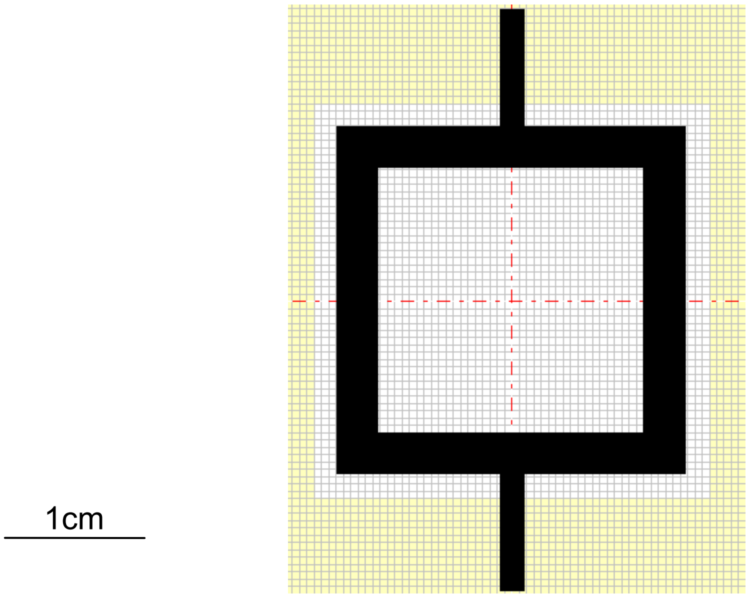

Figure 58: Design of Cassette C mould using Winmark software

In some experiments the cover glass covering the cassettes contained two apertures, as will be explained later: The 2 mm diameter apertures, 2 cm apart, were made in the glass cover with the laser (100 mm/s, 40 %, 2 scans) at the position of the intersection of the electrodes and the channel, to enable air bubbles to escape the medium. The electrodes, 1.5 cm apart, were passed through the PDMS frame close to the top. Initially the electrodes were inserted inside PEEK tubes with an aperture as described in Cassette B but as eventually the PEEK tubes were discarded and the final design of Cassette C is represented in Figure 59.

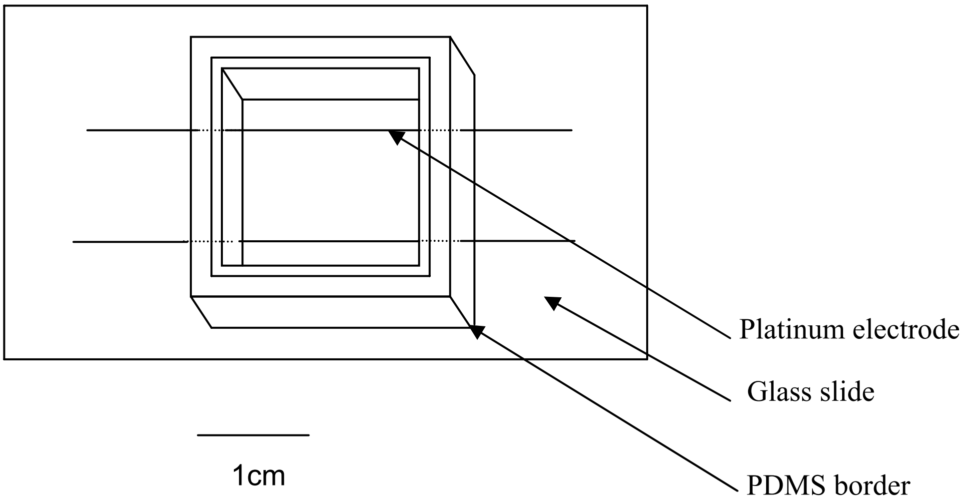

Figure 59: Schematic representation of Cassette C

5.2.3. Gels, polymer and solution frozen inside the cassettes

Polymers, gels and electrolytic solutions were successively frozen between the electrodes. A glass cover was put on top of the electrodes and 6 channels were scanned over the area covered (100 mm/s, 6 %, 50 scans).

5.2.3.1. Gels

A first gel was prepared by dissolving 0.2 g of acrylamide and 0.2 g of methacrylic acid in 5 mL of water and a second gel was prepared by dissolving 0.8 g of acrylamide and 0.205 g of AMPSA in 5 mL of water. The solution was sonicated for 10 min and degassed with argon. The initiators (5 µL of 1.7 M ammonium persulfate (APS) and 2.5 µL of 99 % TEMED) were added to the mixture and the polymerisation was carried out at 22 °C for 1 hr.

5.2.3.2. Polymers

3.33 mL of acrylamide/methylene bisacrylamide (stock solution containing 30% total monomer and 2.6% cross-linker) were placed in 16.67 mL of water. The solution was sonicated and mixed for 5 min and then placed in the fridge for another 5 min. Tris(hydroxymethyl)aminomethane was added to shift the pH to 7.5. The solution was then sonicated again for another 10 min. 5 µL of 99 % TEMED and 5 µL of 40 % APS were added into 5 mL of the polymer solution. The solution was mixed together and poured into a plate. The polymerisation was carried out in an oven at 60 °C for 30 minutes. A cover glass was placed on top of the polymer between the electrodes and the plate was frozen.

Short polymeric chains AMPSA/acrylamide and MAA/acrylamide were polymerised. 0.8 g of acrylamide were mixed with 0.459 g of AMPSA, 5.503 g of water and 0.786 g of 2-propanol for the former and 0.8 g of acrylamide were mixed with 0.2 g of MAA in 3.5 g of water and 0.5 g of 2-propanol for the latter. Both solutions where sonicated for 20 minutes.4 µL of 40 % APS and 4 µL of 99 % TEMED were added to them. The polymerisations were carried out in an oven at 80 °C for 2 hrs.

5.2.3.3. Solutions

The 10 mM HCl had a pH of 2.0 and a conductivity of 3.3×10^{-6} S at room temperature. The 100 mM acetic acid was mixed with 20 % sucrose to increase the density and had a pH of 3.6 and a conductivity of 6.7×10^{-7} S at room temperature.

The media were tested before carrying out electrophoresis. The media were frozen inside Cassette A. A glass cover covered the solution between the electrodes and

6 channels 22 mm long and 1.25 mm apart were scanned 50 times at 6% power and 100 mm/s over the area covered. The electrophoresis power supply was then switched on and the current was recorded.

5.2.4. Dye electrophoresis

The initial experiments of separation in channels were performed in Cassette A filled with 10 mM HCl. Cassette A was laid on the cooling platform at -20 °C. After 60 min, the middle area was frozen and the experiments for separation were undertaken as follows: a 2 mm diameter cavity was drilled with the laser (6%, 150 mm/s, 50 scans) in the frozen area 0.5 cm away from the liquid area (see Figure 60). The cavity was filled with 0.8 g/L Meldola's Blue, which was left to freeze for 2 min, covered with a cover glass and left for 5 more minutes until the cover glass became attached to the surface. The electrical conditioning with the power supply was set at 50 V, 20 mA and 3 W maximum. Channel A, as shown in Figure 60, was scanned with the laser (8 %, 150 mm/s, 50 scans) to allow the dye to fill the channel. The channel was allowed to refreeze for 4 minutes without any current before the current was reapplied. The separation channels (B) were scanned (8 %, 150 mm/s, 50 scans). Channels B were 4 cm long and 6 mm apart. The presence of dye in the separation channels was checked with a microscope and a spectrophotometer.

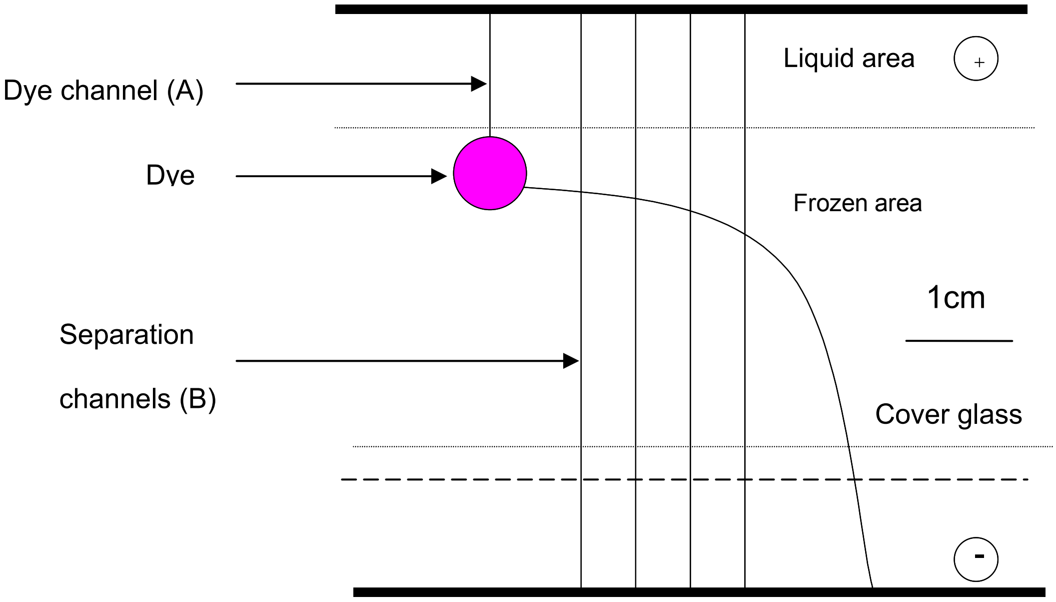

Figure 60: Electrophoresis design

5.2.5. Dye separation

The later experiments on dye separation were performed in Cassette C filled with 10 mM HCl. Cassette C was mounted on top of the cooling platform at -20 °C. After 25 min the 10 mM HCl solution was frozen. Two holes of 2 mm diameter, 2 cm apart, were drilled in the glass cover with the laser (100 mm/s, 40 %, 7 scans) at the position of the intersection of the electrodes and the channel, to enable air bubbles to escape the medium.

The electrophoresis conditions were 500 V, 10 mA and 3 W. The voltage was applied until the current was stable. The value of 0.5 mA remained stable for 5 minutes, then Channel A (see Figure 61) was scanned with the laser (6 %, 50 mm/s, 150 scans) and 2 µL of 2 mg/mL Rhodamine B was injected inside channel A with a micro syringe and left to freeze for 10 min, after which the separation channel (channel B) was scanned (5 %, 150 mm/s, 50 scans). The marking was unidirectional (from left to right).

The current was reapplied. The migration of the dye within the separation channel was observed with the Digital Blue camera.

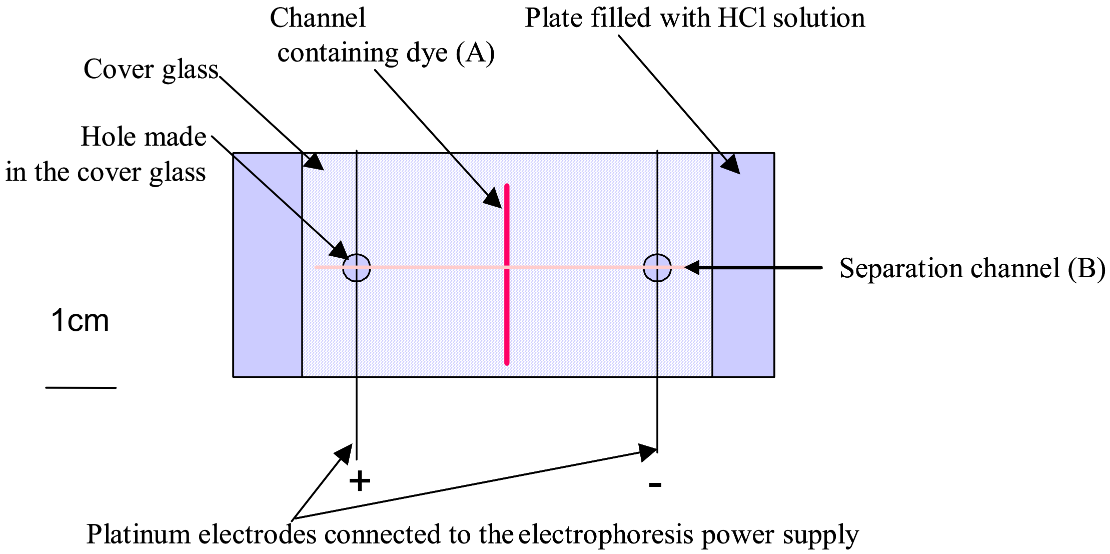

Figure 61: Experimental set-up for dye electrophoresis

A longer separation path was then tested. The first long path tested was a zigzag shaped channel as shown in the picture below on the left, then an s-shaped channel as on the right hand side.

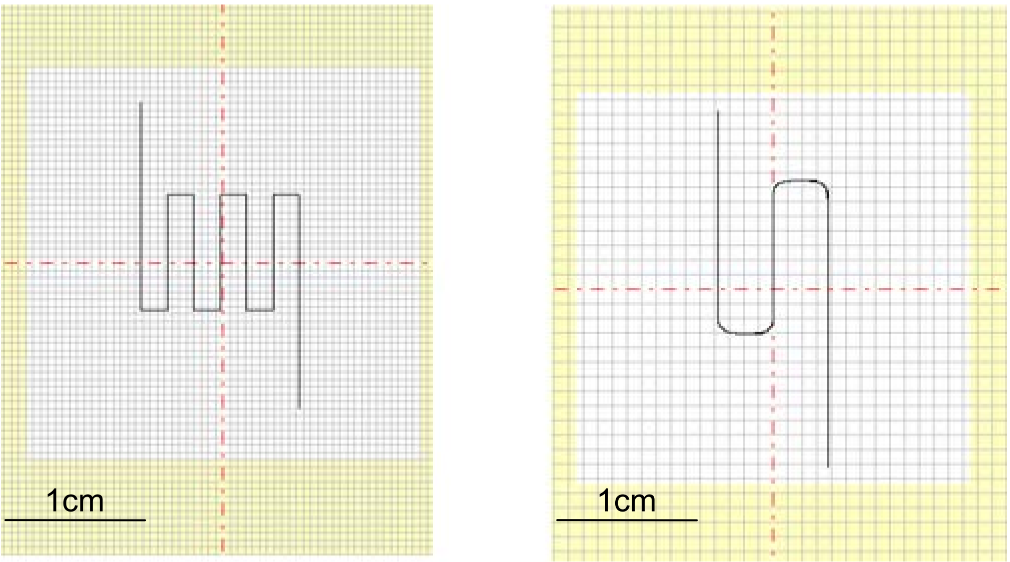

Figure 62: Long path separation channels

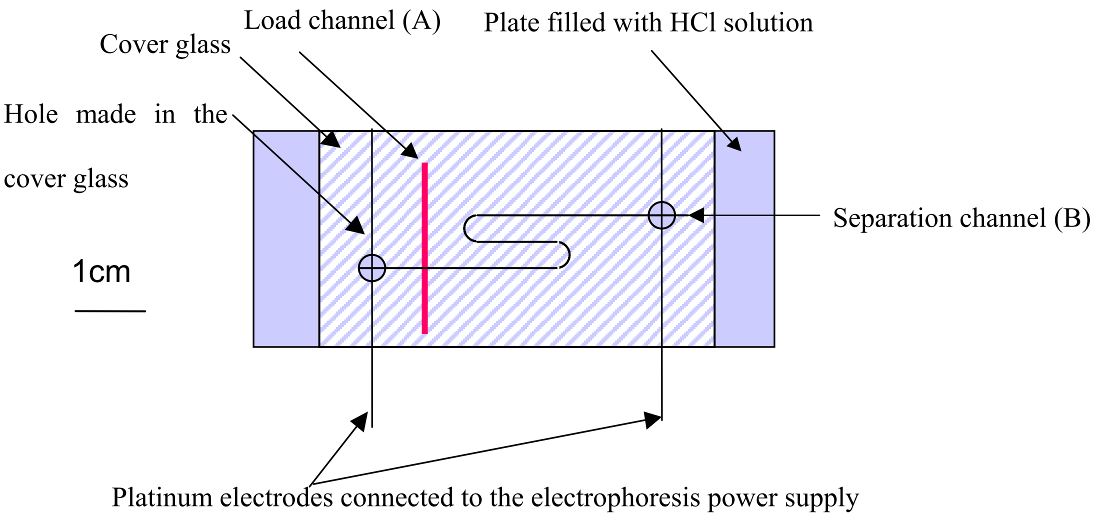

Figure 63: Experimental set-up for long path separation

The electric conditioning of the power supply set the value of the voltage supply and the limit values of current and power. The electric conditions were 100 V,0.1 mA tnd 3 W. The current reading was 0.3 mA. Rhodamine B dye was injected into channel A and the scanning of channel B was repeated 80 times at 6 % power and 50 mm/s. The electrophoresis was monitored with a CCD camera under UV light.

Following the protocol described in the previous section, we also tested a bi-directional beam (50 mm/s, 5% power, 50 scans in both directions).

To test the separation of a mixture, we used a mixture of 1 g/L Rhodamine B and 1 g/L Bromocresol Green (dissolved in glycerol). The same protocol as described in paragraph 5.2.5 was followed.

5.2.6. Separation in channels created by laser (no current applied)

In Cassette C mounted on top of the cooling platform at -20 °C, a 2 mm diameter hole was drilled in the 80 mM frozen acetic acid and filled with a mixture of 1 g/L Rhodamine B and 1g/L Bromocresol Green (dissolved in glycerol). The solution was allowed to freeze for 10 minutes and an s-shaped channel was scanned at 50 mm/s and 6 % across the frozen dye area.

5.3. Results

5.3.1. Cassettes

The freezing time of water inside the cassettes previously described was tested. The cassettes were filled with water and mounted on top of the cooling platform at -20 °C. The volume of each cassette and the time required to freeze the water solution in each cassette were recorded (Table 2).

Table 2: Volume and time of freezing of Cassettes A, B and C

Cassette	**Volume**	**Time of freezing** (cooler at -20ºC)
A	10 mL	60 min
B	10 mL	75 min
C	2 mL	25 min

Cassette B was discarded and replaced by Cassette C because freezing took too long and the contents melted very easily during manipulation.

In the initial design of Cassette C, the electrodes were masked in PEEK tubes with only a 4 mm aperture to restrict the area available for electrophoresis. However the solution inside the PEEK tube would freeze as well, no current was monitored and electrophoresis could not proceed. The use of PEEK tubes was therefore discarded.

Freezing and scanning were performed with and without a cover glass. In the absence of a cover glass, the ice surface was not flat and evaporation during laser marking would occur. A thin layer of mineral oil (N-octane) was spread on top of frozen HCl to enable a flat ice surface. However it melted the ice so the idea was discarded.

In the presence of a cover glass, shrinking and expansion of ice against the cover occurred as well as condensation on the glass cover (leading to poor imaging). In order to make the cover glass hydrophobic it was treated with a solution of 2% dichlorodimethylsilane in methanol. Also 1 mm diameter holes were drilled with the laser (100 mm/s, 90 %, 1 scan) in the cover glass to let the bubbles created during electrophoresis escape.

5.3.2. T-junction

Electrophoresis in ice capillaries is a very complex process and this holds mainly to the nature of ice which can melt or freeze very easily. Electrophoresis in capillaries made under low voltage was tested in T-junction capillaries made in Perspex. T-junctions were the first devices developed as injection tools inside capillaries by Verheggen *et al.* (1988) and they are common devices used for capillary electrophoresis nowadays.

5.3.2.1. Millimetre capillary T-junction

First, millimetre T-junction channels made in Perspex, as described in Figure 54, were filled with electrophoresis solution (Figure 65). The electrophoresis solution was 100 mM acetic acid (pH = 3.3) mixed with 20% sucrose. Acetic acid was preferred to an HCl solution, which generated too many bubbles in this study. Sucrose was added to increase the solution density and prevent the dye from moving freely inside the channels.

The electrophoresis power supply was switched on. The electrophoresis conditions were set to 500 V, 10 mA and 3W. The current value stabilised at 0.6 mA in 5 min. 2 μL of 1 mg/mL Rhodamine B (Figure 64) was injected into the dye channel (Figure 66) with a micro syringe and the voltage was applied (readings: 500 V and 0.6 mA). The dye moved towards the cathode (Figure 67). However due to the dimensions of the channel, the dye entered the separation channel before the voltage was applied, therefore it was decided to try this experiment with a micro capillary T-junction instead. The micro capillary T-junction had channels 8 times smaller than the millimetre T-junction.

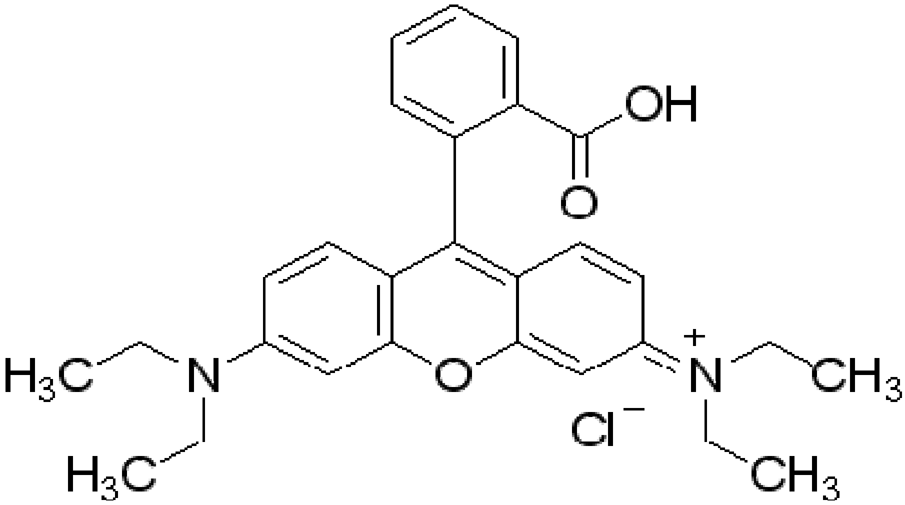

Figure 64: Rhodamine B structure

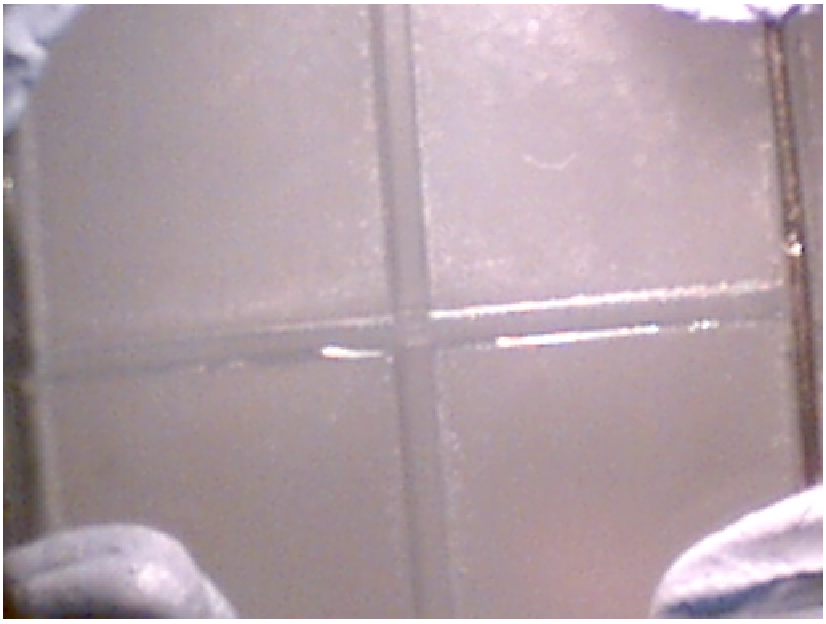

Figure 65: T-Junction drilled in Perspex

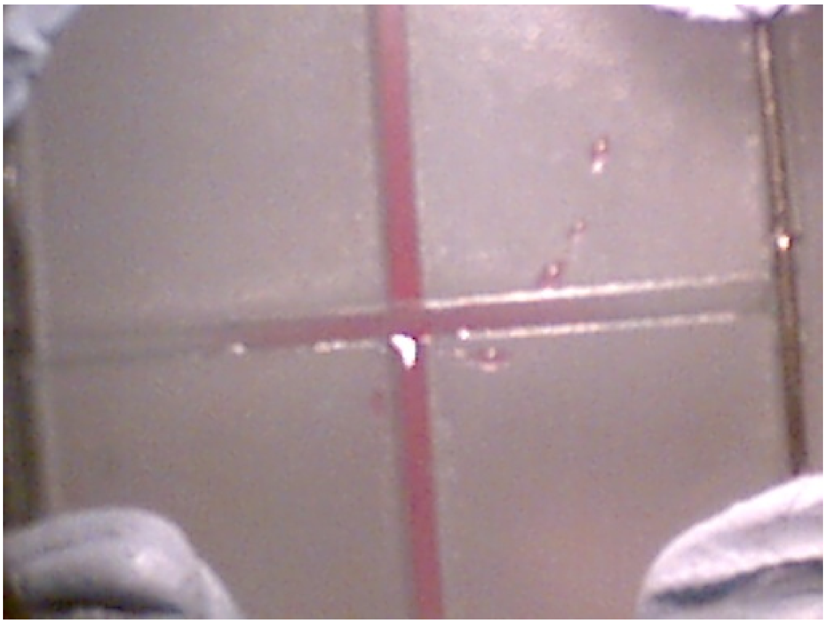

Figure 66: Injection of Rhodamine B dye

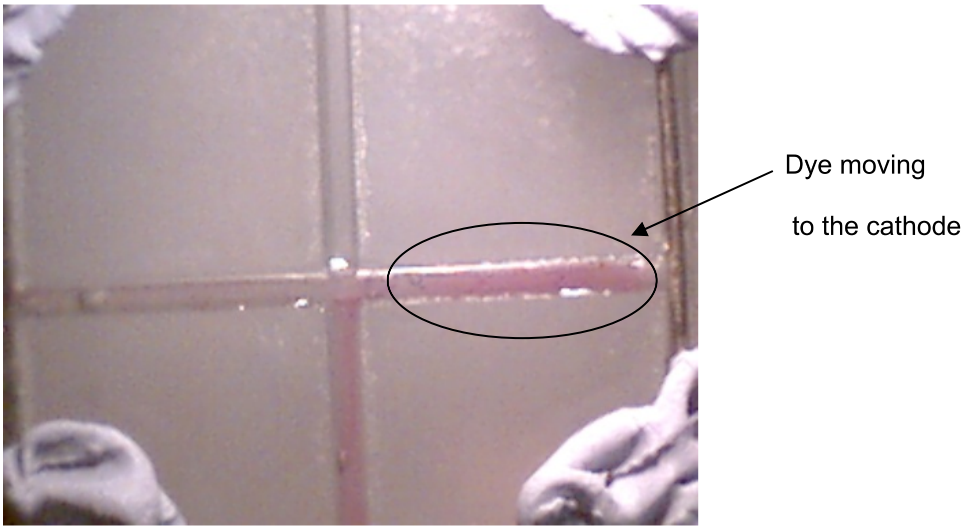

Figure 67: After application of a voltage between the electrodes the dye moves to the cathode.

5.3.2.2. Micro capillary T-junction

The micro capillary T-junction was described in Figure 55. As previously, the channels were filled with a solution of 100 mM acid acetic (pH=3.3) containing 20 % sucrose (Figure 68). The electrophoresis conditions were 500V, 10 mA and 3 W. The voltage was applied until the current was stable and reached a value of 0.4 mA. It stayed stable for two minutes and then dropped to a value below 100 µA. 2 µL of 1 mg/ Rhodamine B was injected into the dye channel with a micro syringe (Figure 69) and the voltage was applied (readings: 500 V and 100 µA). The dye moved again towards the anode electrode in approximately 60 s (Figure 70).

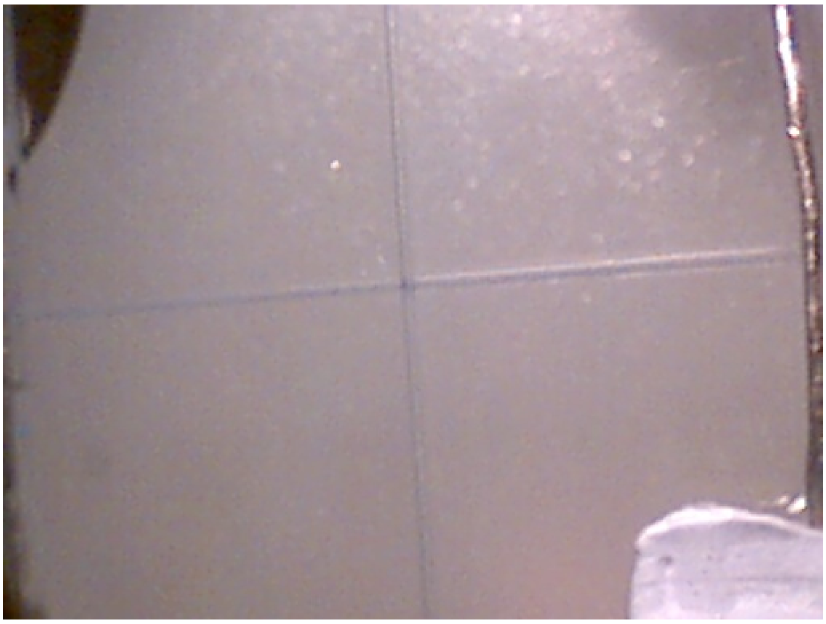

Figure 68: Capillary T-junction in Perspex.

Figure 69: Injection of Rhodamine B into the dye channel.

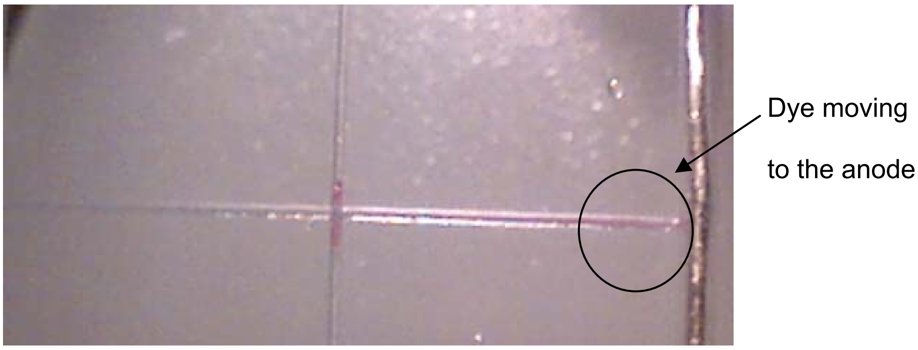

Figure 70: After appliance of voltage between the electrodes the dye moves to the anode.

The same experiment was conducted in the dark under illumination from a UV lamp. Pictures were taken with the CCD camera before and during the application of the voltage between the electrodes to follow the movement of the dye inside the junction. The sequence is shown in Figure 71

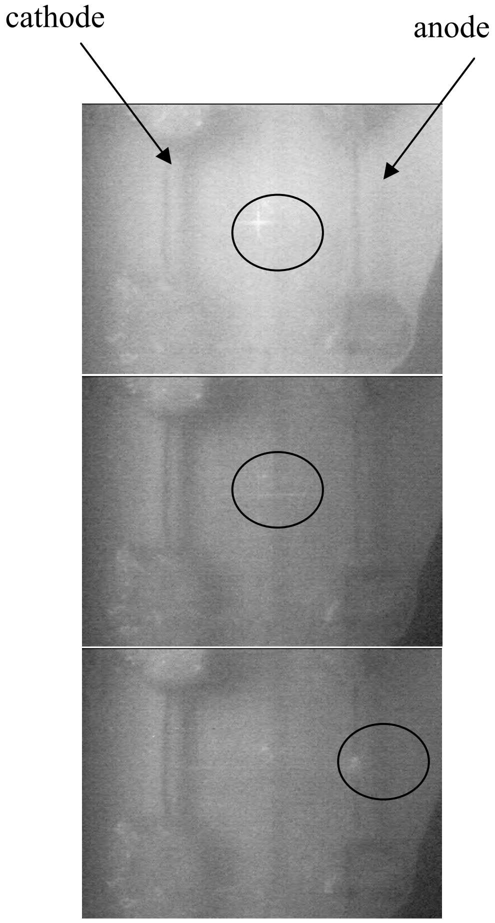

Figure 71: Sequence of pictures taken with a CCD camera under the illumination of a UV lamp showing the flow of Rhodamine B in the microcapillary junction when a voltage of 500 V was applied between the electrodes.

The first image (Figure 71, top) was taken after the Rhodamine B dye was deposited in the centre of capillary junction, initially filled with 100 mM acid acetic (pH=3.3) containing 20 % sucrose. The dye can be spotted as the lighter cross-shape in the middle of the T-junction. The second picture was taken 5 s after the power supply linked to the electrodes was switched on to deliver 500 V. The dye can be seen to have spread inside the channel. The last picture was taken after one minute and shows that the most of the dye had concentrated at the anode.

5.3.3. Electrophoresis in various frozen media

The first media tested was a solution of 10 mM HCl frozen on the cooler at -20 °C and covered with a glass cover. The voltage was applied between the electrodes (50 V, 10 mA, 3 W). The channels were scanned (150 mm/sec, 8 %, 50 scans) over the frozen HCl solution and then stopped. The scanning was repeated 4 times. The current changes were recorded in Figure 72.

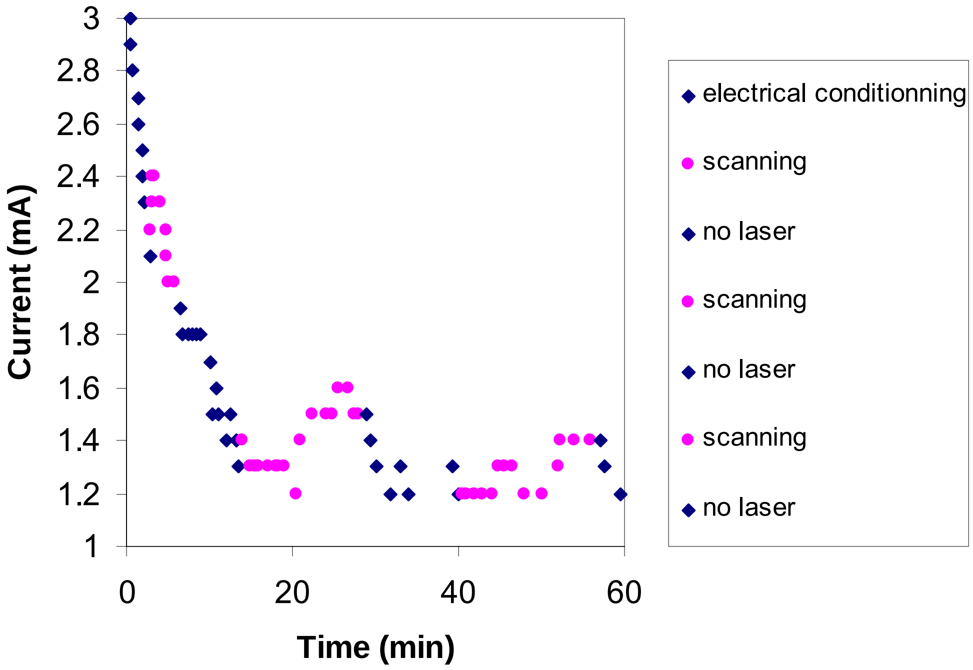

Figure 72: Changes is current passing through the channels created in frozen HCl frozen solution, at 50 V, when 5 channels were scanned (150 mm/s, 8 %, 50 scans).

After each successive opening of the channel, the increase in the current was smaller after each scan; a possible explanation for this was that the solution was depleted in ions from ice.

To prevent this from happening we tried to use anticonvective media which are commonly used for electrophoresis, since the early work done by Tiselius (1937). The passage of current in anticonvective media does not produce heat. Therefore anticonvective media prevent heat-induced modification in the separation process. A representative of this type of support was the MAA gel polymerised as described in section 5.2.3.1. It was poured between the electrodes set 2 cm apart and frozen on top of the cooler at -20 °C. When the voltage was applied (50 V, 10 mA, 3W) between the electrodes and the channels were scanned (6 %, 100 mm/sec, 50 scans) over the frozen MAA without cover glass, an increase in current was recorded. However we noticed issues with the marking of channels in the frozen MAA. Thus scanning resulted in uneven channels, which were impossible to correct. It was decided to discard the use of MAA gel.

Another gel based on AMPSA was also tested. Its polymerisation was described in section 5.2.3.1. It was poured between the electrodes set 2 cm apart and frozen on top of the cooler at -20 °C. Two holes of 2 mm diameter, 2 cm apart were made in the glass cover with the laser (100 mm/s, 90 %, 1 scan) at the position of the intersection of the electrodes and the channel, to enable air bubbles to escape the media. Despite this precaution, too many bubbles were formed on the electrodes when the difference of potential was applied (50 V, 10 mA, 3 W) between the electrodes and the channels were scanned (6 %, 100 mm/sec, 50 scans). Because of the high conductivity of AMPSA, the current was too high and a lot of bubbles were generated. No significant results were obtained with AMPSA gel. As a result of this the work on gels was not continued.

Subsequently short chains were tested. Short chains of relatively low viscosity increase the resolution of separation and have been developed for electrophoresis by Gelfi *et al.* (1995). First, short chain MAA was polymerised as described in section 5.2.3.2. The difference of potential was applied (50 V, 10 mA, 3W) between the electrodes and the channels were scanned (6 %, 100 mm/sec, 50 scans). A net increase of current between the electrodes when 6 channels were scanned was recorded. MAA short chain polymer was a suitable electrophoretic medium for electrophoresis: not many bubbles were generated and the channels scanned were even. AMPSA short chain polymer polymerised as described in section 5.2.3.2 was also tested but too many large bubbles were generated at the electrodes to give any result.

5.3.4. Dye electrophoresis

Figure 74 shows the cavity filled with frozen dye and the separation channels as described in section 5.2.4. This was the first set up tested to investigate the mobility of dye in ice capillary electrophoresis. Meldola’s Blue, which is positively charged (Figure 73), should migrate towards the cathode. The dye moved from the hole inside the s-shaped channel, but when the difference of potential was switched on between the electrodes and the separation channel was scanned, no evidence of the presence of dye in the separation channel was found. This can be explained by the dissolution of dye when it flows from the hole of dye into channel A and then from channel A into the separation channels B. It was very diluted by the time it arrived into channels B and even more by the time the picture was taken – since taking the picture required removal of the cassette from the cooling platform under the laser to place it under the microscope, which allowed the channels to melt and the dye to sink to the bottom of the ice, meaning that it was impossible to photograph this. This set up was not continued and it was preferred to inject dye directly into channel A as was done in the next section.

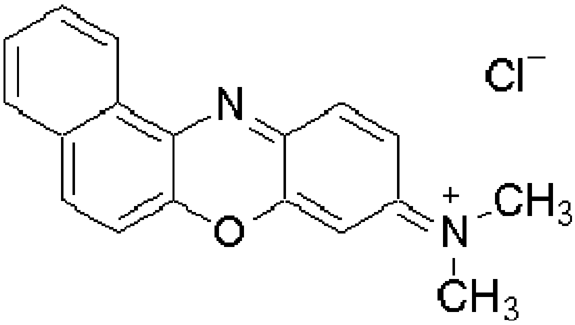

Figure 73: Meldola's Blue structure

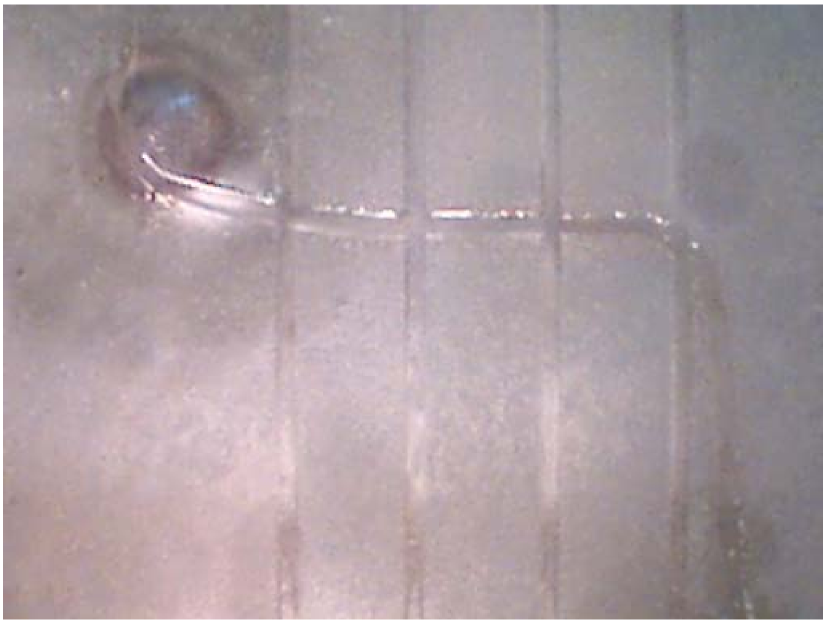

Figure 74: Microfluidic set up created for investigation of mobility of Meldola's Blue in ice capillaries scanned by the laser (8 %, 150 mm/s, 50 scans)

5.3.5. Dye separation

The set up described in section 5.2.5 was tested for dye mobility as well as dye separation. Figure 75 was taken when the Rhodamine B dye was injected into channel A and Figure 76 was taken after the separation channel was marked across channel A and the electrodes, before the voltage was applied. A migration of dye in the separation channel towards the cathode can be seen in Figure 76. To make the following pictures (Figure 75 to 77) the cassettes were removed from the cooling platform and put under the microscope. This would involve partial melting of the surface of the ice and the capillaries and the migration of dye outside the channels, which explains the presence of dye outside the channels on some of the following pictures and the poor imaging.

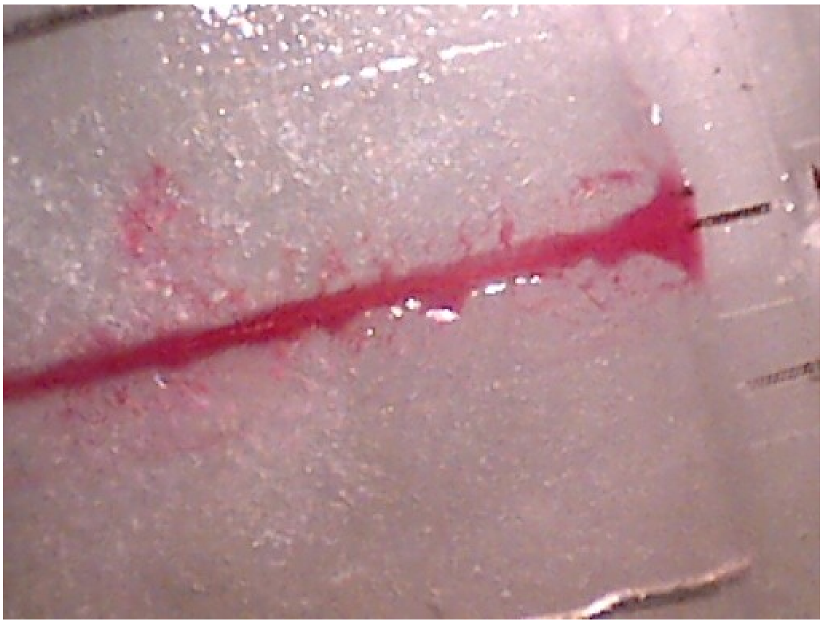

Figure 75: Rhodamine B load

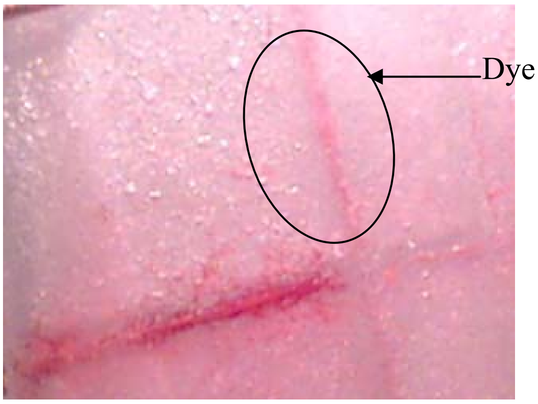

Figure 76: Flow of Rhodamine B inside the separation channel. Image made after letting the channel freeze for 1 minute.

In case of a bi-directional scanning, the dye also moved towards the cathode as shown in Figure 77.

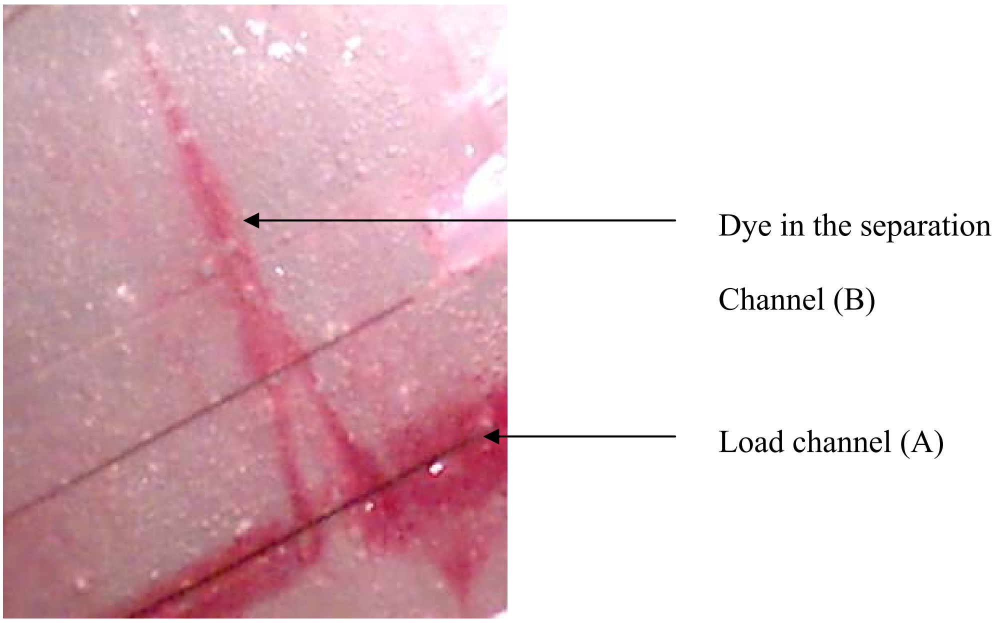

Figure 77: Electrophoresis result when the separation channel was scanned in both directions.

5.3.6. Mixture of dye separation

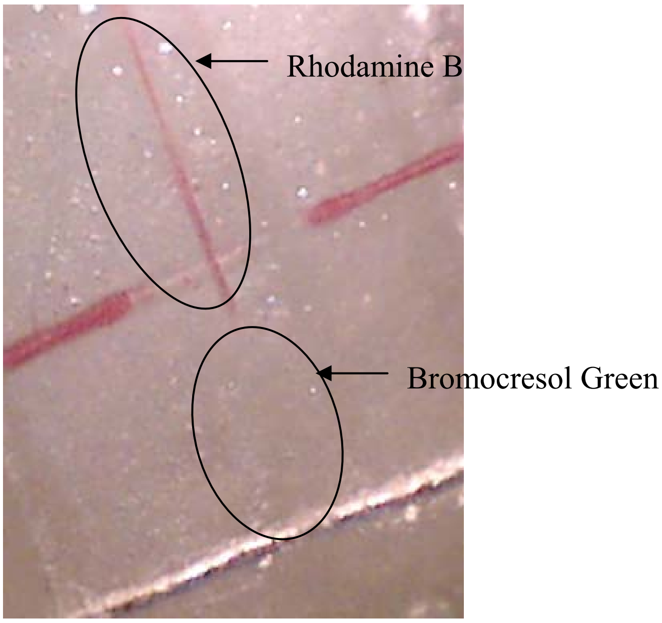

Figure 78: Electroseparation of Rhodamine B and Bromocresol Green.

In the picture above, Rhodamine B migrated towards the cathode and Bromocresol Green towards the anode. Bromocresol Green was only very slightly visible in the channel towards the anode. Some Rhodamine B was visible in the previous picture in the separation channel in the direction of the anode. This is due to the partial melting of the ice when the picture was taken and the moving of dye that it provoked.

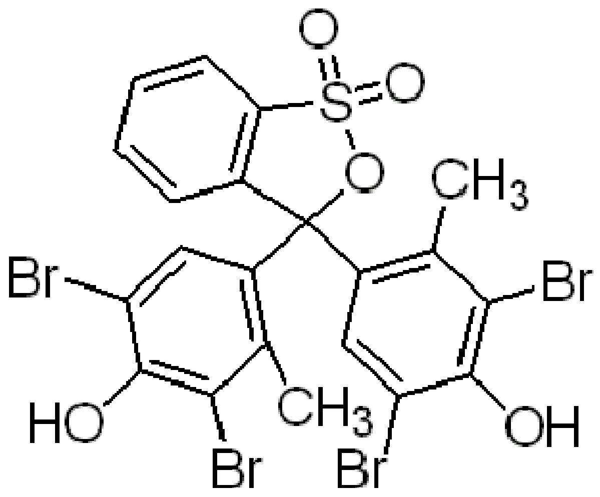

Figure 79: Bromocresol Green structure

5.3.7. Long path channel

The dye was not moving along the whole zigzag path described in section 5.3.7 which was too long and too angular to let the dye move along the whole path. It was modified to become an S-shaped path with rounded angles. In this path, the moving of the dye through electrophoresis can be seen in Figure 80 demonstrating that the separation path does not have to be rectilinear and perpendicular to the electrodes to observe movement of the dye and, within certain limits, it can have various shapes and length.

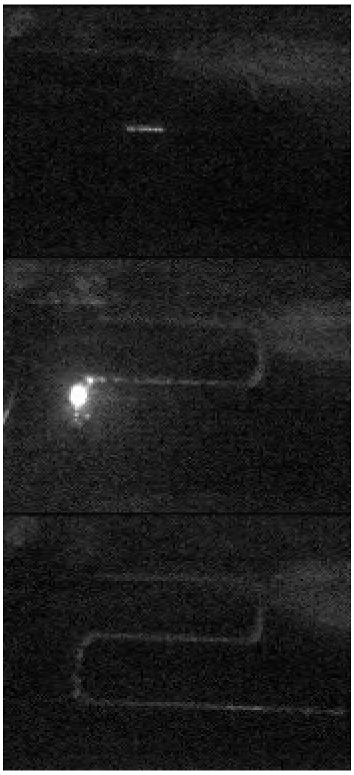

Figure 80: Successive images taken with a CCD camera in the dark under the illumination of a UV light during the scanning of an S-shaped channel in which Rhodamine B flows

5.3.8. Mobility of dye in the channel when no current was applied

This experiment was to done to investigate the effect of laser scanning on dye mobility inside the channels when no voltage was applied.

The dye moved along the channel in the direction of scanning although no voltage was applied.

The results of this series of experiments showed that dye can move inside channels during scanning alone as well as during electrophoresis and that both scanning and the applied current have an effect on the movement of the dye.

5.4. Conclusion

This work is similar to early stages capillary electrophoresis development where basic parameters (i.e. capillary dimensions and voltage conditions) have to be optimized first. The objective of the experiments done here was primarily to investigate the optimum parameters in which electrophoresis could be successful in ice capillaries.

This series of experiments on electrophoresis in ice capillaries demonstrates the following points:

- It is possible to provide electrophoretic transport in an ice capillary.
- It is possible to obtain electroseparation of 2 dyes (Rhodamine B and Bromocresol Green) in ice capillaries.

Those results were however not obtained without difficulties. First, because high voltages provoked ice to melt quickly, early experiments made in ice capillaries showed the necessity to use low voltage instead of the high voltage in the order of 3000 V usually used in capillary electrophoresis (Su *et al*., 2003). Secondly the dye flowed freely inside the capillaries and the electrophoresis did not result in sharp bands. Finally, the recording of images brought extra difficulties, since it was necessary to move the cassettes from the cooling platform placed under the laser to the microscope, provoking the partial melting of the ice surface and the migration of dye outside the channels.

It can be noted that microcapillaries made in ice are wider than those used for electrophoresis on chips made of traditional material (100 µm instead of 25 µm): smaller channels would freeze instantaneously and dye would not be able to flow.

6. Conclusions and suggestions for future work

The current project was pioneering in the sense that nobody has been using ice as a material for separation before, which made this project very challenging. Despite this some successful results have been obtained which show that the idea of making a microfluidic device in ice was not unrealistic.

It was possible to use a CO_2 laser for rapid creation of channels in ice and various design geometries with dimensions and inner temperature controlled by the laser parameters. The conditions for freezing, and laser scanning were studied in conjunction with the effect they have on ice/channels properties. The optimal range of power/velocity of the laser for the creation of channels was identified as 0.4 to 20 W/m. In this range of settings, the channels with 300 µm wide stayed open for 2 s and could be kept open by successive scanning.

The conductivity measurements in ice confirmed that we can create open and closed channels which can transport ions, analytes and liquid flow in general. Transport inside the channels can be obtained by pressure gradient, by applied current or by the laser marking process alone thanks to the sheer surface tension within the melted area created by the temperature gradient within. The rate of transport observed inside the channels was of the order of 1 mm/s.

We have demonstrated that electrophoresis can be used not only for transport but also for separation of analytes such as Rhodamine B and Bromocresol Green in ice capillaries.

The freezing and melting of ice can be used as a valve in microfluidic systems. The opening of the area depends only on the power and the speed of the laser scanning while the closing by freezing depends on the temperature of the cooling device.

A fibre-optic spectrophotometer was used successfully for measuring dye concentration inside ice channels.

The preconcentration of analytes in ice-based microfluidic devices by laser-assisted zone melting has been demonstrated using Meldola's Blue as a model analyte. This technique can be used for preconcentrating samples inline in a microfluidic device created in ice for both sensing and separation purposes.

The results achieved so far are in line with early development work of traditional microfluidic devices created in glass, plastic or ceramic. More efforts are required to transform the current feasibility study into a successful commercial project. We believe however that the present work provides confidence that this is possible.

The future work can include application of ice-based microfluidic devices for cell growth and for DNA amplification. It is also desirable to achieve miniaturisation of the instrument using Pelletier bridges and a portable laser. The development of a laser resistant container would be also essential for further developments of this microfluidic platform.

7. References

Abbott, N.L. & Skaife, J.J. inventors (3 September 2004) Method and apparatus for detection of microscopic pathogens. US 2005/0106562 A1.

Adamson, A.W. & Gast, A.P. (1997) *Physical Chemistry of Surfaces*. Wiley, New York.

Ashby, M.F. & Easterling, K.E. (1982) A first report on diagrams for grain growth in welds. *Acta Metallurgica*, 30, 1969-1978.

Aubry, N., Batton, J.L. & El Moctar, A.O inventors (9 December 2004) Electrohydrodynamic microfluidic mixer using transverse electric field. WO/2004/105923.

Auroux, P.-A., Iossifidis, D., Reyes, D.R. & Manz, A. (2002) Micro total analysis systems. 2- analytical standard operations and applications. *Analytical Chemistry*, 74, 2637-2652.

Bart, S.F, Mehregany, M., Tavrow, L.S. & Lang, J.H. (1990) Microfabricated electrohydrodynamic pumps. *Sensors and Actuators A*, 21, 193-197.

Bertie, J.E., Labbe, H.J., Whalley, E., Absorptivity of ice I in the range 4000-30cm^{-1}, *Journal of Chemical Physics*, 50 (10), 4501-4520.

Bevan, C.D. & Mutton, I.M. (1995) Use-of freeze-flow management for controlling and switching fluid flow in capillary tubes. *Analytical Chemistry*, 67 (8), 1470-1473.

Bass, M. (1995) *Handbook of optics volume I – Fundamentals techniques and designs.* 2nd Edition. McGraw-Hill. Optical Society of America, New York.

Bourouina, T, Bosseboeauf, A & Grandchamp, J.-P. (1997) Design and simulation of an electrostatic micropump for drug delivery applications. *Journal of Micromechanics and Microengineering*, 7, 186-188.

Brittain, S., Paul, K., Zhao, X.-M. & Whitesides, G. (1998) Soft lithography and microfabrication. *Physics World,* 11, 31-36.

Chan, C., Mazumder, J. & Chen, M.M. (1984) A two-dimensional transient model for convection in laser melted pool. *Metallurgical Transactions A*, 15, 2175-2180.

Chaplin, M.F. (2001) Water: its importance to life. *Biochemistry and Molecular Biology Education,* 29, 54-59.

Chu. .B., Chen, J.T., Yeh, R, Lin, G, Huang, J.C.P, Warneke, B.A. & Pister K.S.J. (1997) Controlled pulse-etching with xenon difluoride. IEEE Proceedings of the Ninth International Conference on Solid-State Sensors and Actuators, Transducers'97, Chicago, Il, USA, 16-19 June 1997, 665-667.

Clark, A.F., Moulder, J.C. & Reed, R.P. (1973) Ability of a CO_2 laser to assist ice breakers. *Applied Optics*, 12 (6), 1103-1104.

Cline, H.E. & Anthony, T.R. (1977) Heat treating and melting material with a scanning laser or electron beam. *Journal of Applied Physics*, 48 (9), 3895-3900.

Da Yong, C., Adelhelm, K, Xiao, L.C. & Dovichi, N.J. (1994) A simple laser-indced fluorescence detector for sulforhodamine 101 in a capillary electrophoresis system: detection limits of 10 yoctomoles or six molecules. *Analystical Chemistry*, 119 (2), 349-352.

Dario, P., Croce, N., Carrozza, M.C. & Varallo, G. (1996) A fluid handling system for a chemical microanalyzer. *Journal of Micromechanics and Microengineering*, 6, 95–98.

Dasgupta, P.K. & Liu, S. (1994) Auxiliary electroosmotic pumping in capillary electrophoresis. *Analytical Chemistry*, 66, 3060-3065.

Dean, J.A. (1999) Lange's Handbook of Chemistry (15th Edition) Mc Graw-Hill, New York.

Dolnik, V., Liu, S. & Jovanovitch, S. (2000) Capillary electrophoresis on microchip. *Electrophoresis,* 21, 41-54.

Duley W.W. (1999) *Laser welding.* John Wiley & Sons, Inc, New York.

Emmony, D.C., Howson R.P. & Willis L.J. (1973) Laser mirror damage in germanium at 10.6 μm. *Applied Physics Letters*, 23, 597-601.

Effenhauser, C.S., Paulus, A., Manz, A. & Wildmer, H.M. (1994) High-speed separation of antisense oligonucleotides on a micromachined capillary electrophoresis. Analytical Chemistry, 66, 2949-2953.

Ewing, G.E., Foster, M., Cantrell, W. & Sadtchenko, V. (2003) Thin film water on insulator surfaces. *In*: Buch, V., Devlin, J.P., *Water in confining Geometries*. Springer-Verlag, Berlin, 179-211.

Fournier, J.T. & Snitzer, E., (1974) The non-linear refractive index of glass. *IEEE Journal of Quantum Electronics*, 10 (5), 473-476.

Gavin, P.F. & Ewing, A.G. (1996) Continuous separatons with microfabricated electrophoresis-electrochemical array detection. *Journal of the American Chemical Society*, 118, 8932-8936.

Gelfi, C., Orsi, A., Leoncini, F. & Righetti, P.G., (1995) Fluidified polyacrylamides as molecular sieves in capillary zone electrophoresis of DNA fragments. *Journal of Chromatography A*, 689, (1), 97-105.

Gravesen, P., Branebjerg, J. & Jensen, O.S. (1993) Microfluidics - a review. *Journal of Micromechanics and Microengineering*, 4, 168-182.

Griffiths, D.J. (1999) *Introduction to Electrodynamics*. 3rd edition. Prentice-Hall, Upper Saddle River, NJ.

Gui, L. & Liu, J. (2004) Ice valve for a mini/micro flow channel. *Journal of Micromachined Microengineering*, 14, 242-246.

Guo, T., Nikolev, P., Rinzler, D., Tomanek, D.T., Colbert, D.T. & Smalley, R.E. (1995) Self assembly of tubular fullers. *Journal of Physical Chemistry*, 99, 10694-106947.

Gurney, H.P., & Lurie, J., (1923) Charts for estimating temperature distributions in heating or cooling solid shapes. *Industrial Engineering & Chemistry*, 15, 1170-1172.

Haneveld, J., Jansen, H., Berenschot, E, Tas, N & Elwenspoek, M. (2003) Wet anisotropic etching for fluidic 1D nanochannels *Journal of Micromechanis and Microengineering*, 13, S62-S66.

Hannig, K. (1982) New aspects in preparative and analytical continuous free-flow cell electrophoresis. *Electrophoresis*, 3, 235-242.

Harrison, D.J., Manz, A., Fan, Z.H., Ludi, H & Wildmer, H.M. (1992) Capillary electrophoresis and sample injection systems integrated on a planar glass chip *Analytical Chemistry*, 64, 1926-1932.

Hawks, I.C., Lamb, M. & Steen, W.M. (1983) Surface topography and fluid flow in laser surface melting. *3rd International Colloquium on welding and melting by electrons and laser beam*, Lyon, France, 5-9 September 1983, 125-131.

Hayden, S.H. (1995) Resistance to laser radiation. *In*: Bach H. & Neuroth N. *The Properties of Optical Glass* Schott series on Glass and Glass ceramics, Science, Technology and Applications, Sringer-Verlag, Berlin, 139-142.

Heckele, M., Bacher, W. & Muller, K.D. (1998) Hot embossing-the molding technique for plastic microstructures. *Microsystems Technology*, 4, 122–4.

Heckele, M. & Schomburg, W.K. (2004) Review on micro molding of thermoplastic polymers. *Journal of Micromechanics and Microengineering*, 14, R1–R14.

Helmohltz, H. (1953) Ueber einige Gesetze der vetheiling elektrisher strome in korperlichen leiten mit anwendung auf die thierishen elektrishen versuche. *Annalen der Physik und Chemie*, 89 (211), 353-377.

Hjerten, S. (1961) Agarose as an anticonvection agent in zone electrophoresis. *Biochimica Biophysica Acta* 53, 514-517.

Hutmacher, D. W., Sittinger, M. & Risbud, M.V. (2004) Scaffold-based tissue engineering: rationale for computer-aided design and solid free-form fabrication systems. *Trends in Biotechnology,* 22 (7), 354-362.

Ion, J.C. (2005) *Laser processing of engineering materials.* Elsevier Butterworth-Heinemann, Oxford.

Irvine, W. & Pollack, J.B. (1968) Infrared optical properties of water and ice spheres. *Icarus*, 8, 324-360.

Jacobson, S.C., Hergenroder, R., Koutny, L.B. & Ramsey J.M. (1994), High-Speed separations on a microchip. *Analytical Chemistry*, 66, 1114-1118.

Jennison, M. & Gibala, J. inventors (30 November 2006) Laser ice etching system and method. WO/2006/127867.

Johari, G.P. (1981) The spectrum of ice. *Contemporary Physics*, 22 (6), 613-642.

Johnson, T.J., Ross, D. & Locasio, L.E. (2002) Rapid Microfluidic Mixing. *Analytical Chemistry*, 74 (1), 45-51.

Jorgensen, J.W. & Lukacs, K.D.A (1981) Zone-electrophoresis in open-tubular glass capillaries. Analytical Chemistry, 27 (9), 1551-1553.

Judy, J., Tamagawa, T. & Polla, D.L. (1991) Surface-machined micromechanical membrane pump. *Proceedings of the MEMS '91.* Nara, Japan, 30 January–2 February 1991, 182–186.

Katrusiak, A. (1996) Rigid H_2O molecules model of anomalous thermal expansion of ices. *Physical Review Letters,* 77 (21), 4366-4369.

Kim, E., Xia, Y. & Whitesides, G.M. (1995) Polymer microstructures formed by moulding in capillaries. *Nature*, 376, 581-584.

Kim, J. & Xu, X. (2003) Excimer laser fabrication of polymer microfluidic devices. *Journal of Laser Applications*, 1 (4), 255-261.

King, E., Xia, Y., Zhao, X.-M. & Whitesides, G.M. Solvent-assisted mocrocontact molding: A convenient method for fabricating three-dimensional structures on surfaces of polymers. *Advanced Materials*, 9 (8), 651-654.

Koch, M., Chatelain, D., Evans, A., & Brunnschweiler, A. (1998) Two simple micromixers based on silicon. *Journal of Micromechanics and Microengineering*, 8, 123-126.

Koch, M., Evans, A. & Brunnschweiler, A. (2000) *Microfluidic Technology and Applications*. Research Studies Press, Baldock.

Konrad, R., Ehrfeld, W., Freimth, H., Pommersheim, R., Schenk, R. & Weber, L. (1997)

Miniaturization as a demand of high-throughput synthesis and analysis of biomolecules. *Proceedings of the 1st International Conference on Microreaction Technology*. 23-25 February 1997, Frankfort, Germany.

Kowalewski, T.A. & Rebow, M. (1999) Freezing of water in the differentially heated cubic cavity. *International Journal of Computational Fluid Dynamics*, 11, 193-210.

Kundu, P.K. (2007) *Fluid Mechanics*, 4th edition. Academic Press, London.

Kunkel, H.G. & Tiselius, A. (1952) Electrophoresis of proteins on filter paper. *Journal of General Physiology*, 35, 89-118.

Laptewicz, J.E. & Bauer, R. inventors (6 May 1985). Laser beam resistant material. US 4611588.

Laser, D.J. & Santiago, J.G (2004) Review of micropumps. *Journal of Micromechanics and Microengineering*, 14, R35-R64.

Lauks, I.R. (1998) Microfabricated biosensors and microanalytical systems for blood analysis. *Accounts of Chemical Research*, 31, 317-24.

Lee, L.P., Berger, S.A., Liepmann, D. & Pruitt, L. (1998) High aspect ratio polymer microstructures and cantilevers for bioMEMS using low energy ion beam and photolithography. *Sensors and Actuators A*, 71, 144-149.

Leloux, L.S. (1999) The influence of macromolecules on the freezing of water. *Journal of Macromolecules Science, Part C - Reviews in Macromolecular Chemistry and Physics,* 39 (1), 1-16.

Li, P.C.H. & Harrison, D.J. (1997) Transport, manipulation, and reaction of biological cells on-chip using electrokinetic effects. *Analytical Chemistry*, 69, 1564-1568.

Liu, S.R., Shi, Y.N., Ja, W.W. & Mathies, R.A. (1999) Optimization of high-speed DNA sequencing on microfabricated capillary electrophoresis channels. *Analytical Chemistry*, 71, 566-573.

Long, P. inventor. (10 august 1999) Methods for removing ice by using laser beam radiation. CA2222881.

Luck, W.A.P. (1985) *Water and ions in biological systems*. Plenum: New York.

Luckey, J.A., Drossman, H., Kostichka, A.J., Mead, D.A., D'Cunha, J., Norris, T.B & Smith, L.M. (1990) High speed DNA sequencing by capillary electrophoresis. *Nucleic Acid Research*, 18 (15), 4417-4421.

Maiman, T.H. (1960) Stimulated optical radiation in ruby. *Nature*, 187, 493-394.

Manz, A., Gettinger, J.C., Verpoorte, E., Ludi, H., Wildmer, H.M. & Harrison, D.J. (1991) Micromachining of monocrystalline silicon and glass for chemical analysis systems. A Look into next century's technology or just a fashionable craze? *Trends in Analytical Chemistry*, 10 (5), 144-149.

Manz, A., Graber, N. & Widmer, H.M. (1990) Miniaturized total chemical systems: a novel concept for chemical sensing. *Sensors and Actuators B,* 1 (1-6) 244-248.

Manz, A., Miyahara, Y., Miura, J., Watanabe, Y., Miyagi H. & Sato, K. (1990) Design of an open-tubular column liquid chromatograph using silicon chip technology. *Sensors* *and Actuators B,* 1 (1-6) 249-255.

Manz, A., Harrison, D.J., Verpoorte, E.M.J., Fettinger, J.C., Paulus, A., Ludi, H. & Widmer, H.M. (1992) Planar chips for miniaturization and integration of separation techniques into monitoring systems. *Journal of Chromatography*, 593, 253-258

McDonald, J.C., Duffy, D.C., Anderson, J.R., Chiu, D.T., Wu, H., Schueller, O.J.A. & Whitesides, G.M. (2000) Fabrication of microfluidic systems in poly(dimethylsiloxane). *Electrophoresis,* 21, 27-40.

McLean, W., Balooch, M. & Siekhaus, W.J. inventors (2 November 1997) Laser ablated hard coating for microtools, US 5747120.

McNight, T.E., Culbertson, C.T., Jacobson, S.C. & Ramsey, J.M. (2001) Electroosmotically induced hydraulic pumping with integrated electrodes in microfluidic devices. *Analytical Chemistry*, 73, 4045-4049.

Meglinsky, I.V., Varejka M., Woodman, A.C., Piletsky, S.A. & Turner, A.P.F. (2005), Laser ice scaffolds modeling for tissue engineering. *Laser Physics Letters,* 2 (9), 465-467.

Melcher, J.R. (1981) *Continuum Electromechanics*. MIT Press, Cambridge, MA.

Moreau, W.M. (1988) *Semiconductor Lithography*. Plenum Press, New York.

Meinhart, C.D., Wereley, S.T. & Santiago, J.G. (1999) PIV measurements of a microchannel flow. *Experiments in Fluids*, 27, 414-119.

Moroney, R.M., White, F.M. & Howe, R.T. (1991) Microtransport induced by ultrasonic Lamb waves. *Applied Physics Letters*, 59 (71), 774-776.

Nobuo, K., Tatsu. O. & Takashi, N. inventors (4th December 1979) Method and apparatus for laser zone melting.US 4177372.

OceanOptics *USB2000 Fiber Optic Spectrometer Operating Instructions.* Available at: http://www.oceanoptics.com/technical/usb2000.pdf.

Olssen, A. Stemme & G, Stemme, E. (1995) A valve-less planar fluid pump with two pump chambers. *Sensors and Actuators A*, 46-47, 549-556.

Oughton, J. & Xu, S. (2001) The purification of water by freeze-thaw or zone melting. *Journal of Chemical Education*, 78 (10).1373-1374.

Pauling, L. (1935) The Structure and Entropy of Ice and of Other Crystals with Some Randomness of Atomic Arrangement. *Journal of American Chemical Society,* 57, 2680-2684.

Pfann W.G. (1952) Principles of Zone-Melting, *Journal of Metals*, 4, 757-753.

Pfann W.G. & Olsen K.M. (1952) Purification and prevention of segregation in single crystals of gemanium. *Physical Review*, 89 (1) 322-323.

Piletsky, S.A., Piletska, E.V., Karim, K., Turner, A.P.F. & Bossi, A., inventors (11th April 2002) Selective Binding Materials. WO02/29412 A2.

Purcell, E.M. (1977) Life at low Reynolds numbers. *American Journal of Physics*, 45 (1) 3-12.

Qin D., Xia Y., Rogers J.A., Jackman R.J., Zhao X.-M. & Whitesides G.M. (1999) Microfabrication, microstructures and microsystems. *In*: Manz, A. and Becker, H., *Microsystem Technology in Chemistry and Life Science*. Springer-Verlag, Berlin, Germany. 1-20.

Reinhardt, H., Kriews, M., Miller, H., Schrems, O., Ludke, C., Hoffmann, E. & Stroke, J. (2001) Laser ablation inductively coupled plasma mass spectrometry: a new tool or trace element analysis in ice cores. *Fresenius Journal of Analytical Chemistry*, 370, 629-636.

Reuss, F.F. Charged-induced flow (1809). *Proceedings of the Imperial Society of Naturalists of Moscow*, 3, 327-344.

Reyes, D.R., Iossifidis, D., Auroux, P.-A. & Manz, A. (2002) Micro Total Analysis Systems. 1. Introduction, theory, and technology. *Analytical Chemistry,* 74, 2623-2636.

Richter, R., Plettner, A., Hoffmann, K.A. & Sandmaier, H. (1991) A micromachined electrohydrodynamic (EHD) pump. *Sensors and Actuators A,* 29, 159-168.

Roberts, M.A., Rosiers, J.S., Bercier, P. & Girault H. (1997) UV laser machined polymer substrates for the development of microdiagnostic systems. *Analytical Chemistry*, 69, 2035-2042.

Robbins, H. & Schwatz, B. (1960) Chemical etching of Silicon II. The system HF, HNO_3, H_2O and $HC_2H_3O_2$. *Journal of the Electrochemical Society*, 107 (2), 108-111.

Rosenthal D. (1946) The theory of moving sources of heat and its application to metal treatments. *Transactions of the American Society of Mechanical Engineers*, 68, 849-866.

Runyon, M.K., Johnson-Kerner, B.L. & Ismagilov, R.F. (2004) Minimal functional model of hemostasis in a biometic microfluidic system. *Angewandte Chemie International Edition*, 43 (12), 1531-1536.

Santiago, J.G., Wereley, S.T., Meinhart, C.D., Beebe, D.J. & Adrian, R.J. (1998) A micro particle image velocimetry system. *Experiments in Fluids*, 25, 316-319.

Scales, N. & Tail, N. (2004) Modelling electroosmotic flow in porous media for microfluidic applications. *Proceeding of the 2004 International Conference on MEMS, NANO and Smart Systems,* Alberta, Canada, 25-27 August 2004, 571-577.

Shahba, N. & Rockett, T.J. (1992) Infrared absorption coefficient of silica glasses. *Journal of the American Ceramics Society*, 75 (1), 209-212.

Shen, X.J. & Lin, L. (2002) Microplastic embossing process: experimental and theoretical characterizations. *Sensors and Actuators A*, 97-98, 428-433

Shoji, S. & Esashi, M. (1994) Microflow devices and systems. Journal of *Micromechanics and Microengineering*, 4 (4), 157-171.

Schulz, H., Lyebyedyev, D., Sheer, H.-C., Pfeiffer, K., Bleidiessel, G., Grutzner, G. & Ahopelto, J. (2000) Master replication into thermosetting polymers for nanoimprinting. *Journal of Vacuum Science and Technology B*, 18 (6), 3582-2585.

Seiler, K, Harrison, D.J. & Manz, A. (1993) Planar glass chips for capillary electrophoresis: repetitive sample injection quantitation and separation efficiency. *Analytical Chemistry*, 65 (10), 1481-1488.

Smith, H.A. & Thomas, C.O. (1959) The separation of mixtures of ordinary and heavy water by zone refining. *Journal of Physical Chemistry*,63 (3), 445-447.

Smits, J.G. inventor (4 February 1988) Piezoelectric micropump with microvalves US 4938742.

Spencer, W.J., Corbett, W.T., Dominguez, L.R. & Shafer, B.D. (1978) An electronically controlled piezoelectric insulin pump and valves. *IEEE transactions on sonics and ultrasonics*, 25 (3), 153-157.

Steen, W.M. (2005) *Laser Materials processing*, 3rd edition. Springer-Verlag, London.

Stuart, B. C., Perry, M.D., Feit, M.D., Da Silva, L.B., Nevrubenschik, A.M., Herman, S., Nguyen, H. & Armstrong, P. (1997) Femtosecond laser processing. *Conference on Lasers and Electro-optics OSA Technical Digest Series*, Baltimore, USA, 18-23 May 1997, 11, 159-160.

Stjernstrom, M & Roeraade, J. (1998) Method for fabrication of microfluidic systems in glass. *Journal of Micromechanics and Microengineering*, 8 (1), 22-38.

Su, R., Lin, J.-M., Qu, F., Gao, Y. & Yamada, M. (2004) Capillary electrophoresis microchip coupled with on-line chemiluminescence detection. *Analytica Chimica Acta*, 508 (1), 11-15.

SYNRAD (2001) Fenix^{TM} Laser data sheet. . Available at: http://www.synrad.com/fenix/.

Sze, S.M. (1988) VLSI Technology, 2nd edition. McGraw-Hill, New-York.

Terry, S.C., Jerman, J.H & Angel, J.B. (1979) A gas chromatographic air analyzer fabricated on a silicon wafer. *IEEE Transactions on Electron Device*, 26 (12), 1880-1886.

Tiselius, A. (1937) A new apparatus for electrophoretic analysis of colloidal mixtures. *Transactions of the Faraday Society*, 33, 524-531.

Tokarev, V.N. & Kaplan, A.F.H (1999) Suppression of melt flows in laser ablation: application to clean laser processing. *Journal of Physics D: Applied Physics*, 32, 1526-1538.

Van de Pol, F.C.M., Van Lintel, H.T.G., Elvenspoek, M. & Fluitman, J.H.J. (1990) A thermopneumatic micropump based on micro-engineering techniques. *Sensors and Actuators A,* 21–23, 198–202.

Van den Berg, A., Grisel, A., Verney-Norberg, E., Van der Schoot, B.H., Koudelka-Hep, M. & De Rooij, N.F. (1993) An on wafer fabricated free-chlorine sensor with ppb detection limit for drinking water monitoring. *Sensors and Actuators B*, 13, 396-399.

Van den Berg, A. & Lammerink, T.S.J. (1999) Micro total analysis systems: microfluidic aspects, integration concept and applications. *In*: Manz, A. and Becker, H., *Microsystem Technology in Chemistry and Life Science*. Springer Verlag, Berlin Heilderberg, 21-49.

Van Lintel, H.T.G., Van de Pol, F.C.M. & Bouwstra, S. (1988) A piezoelectric micropump based on micromachining of silicon. *Sensors and Actuators*, 15, 153-167.

Vegas, R. & Vegas, M. inventors (13 February 1990) Laser ice removal system. US 4900891

Verheggen, P.E.M., Beckers J.L. & Everaerts, F.M. (1988) Simple sampling device for capillary isotachophoresis and capillary zone electrophoresis. *Journal of Chromotography*, 452, 615-622.

Waddell, E.A. (2006) Laser ablation as a fabrication technique for microfluidic devices. *In:* Minteer, S.D., *Microfluidic techniques reviews and protocols*, Humana Press, Totowa, New Jersey, 27-38.

Waters, L.C., Jacobson, S.C., Kroutchinia, N, Khandurina, J., Foote, R.S & Ramsey, J.M. (1998) Microchip device for cell lysis, multiplex PCR amplification, and electrophoretic sizing. *Analytical Chemistry*, 70, 5172-5176.

Whitesides, G.M. (2006) The origins and the future of microfluidics. *Nature*, 442, 368-374.

Woias, P. (2005) Micropumps—past, progress and future prospects. *Sensors and Actuators B,* 105, 28–38.

Wolbarsht, M.L. (1991) *Laser applications in medicine and biology*. Plenum Press, New York.

Woolley, A.T. & Mathies, R.A. (1995) Ultra-high-speed DNA sequencing using capillary electrophoresis chips. *Analytical Chemistry*, 67, 3676-3680.

Woolley, A.T. Sansabaugh, G.F. & Mathies, R.A. (1997) High-speed DNA genotyping using microabricated capillary array electrophoresis chips. *Analytical Chemistry*, 69 (11), 2181-2186.

Xia, Y., Kim, E., Zhao, X.-M., Rogers, J.A., Prentiss, M. & Whitesides, G.M. (1996) Complex optical surfaces formed by replica molding against elastomeric masters. *Science*, 273, 347-349.

Yang, Z., Goto, H., Matsumoto, M. & Madea, R. (1999) Active micromixer for microfluidic systems using lead-zirconate-titanate (PZT)-generated ultrasonic vibration. Electrophoresis, 21 (1), 116-119.

Yao, S.H. Hertzog, D.E. Zeng, S.L, Mikkelsen, J.C. & Santiago, J.G. (2003) Porous glass electroosmotoic pumps: design and experiments. *Journal of Colloid and Interface Science*, 268 (1), 143-153.

Zeller, E., Drescchoff, G & Laird, C.M. (1991) Development of laser ice-cutting apparatus. *Antarctic Journal of the United States*, 25 (5), 89-91.

Zengerle, R., Kluge, S., Richter, M. & Richter A. (January 29- February 2 1995) A bidirectional silicon micropump. *Proceedings of the MEMS '95*, Amsterdam, The Netherlands, 29 January – 2 February 1995, 19-24.

Zhao, X.M., Xia, Y.N. Whitesides, G.M. Fabrication of Three-Dimensional Micro-Structures. -. Microtransfer Molding. (1996) *Advanced Materials*, 8, 837-840.

Zhang, B., Liu, H., Karger, B.L. & Foret, F. (1999) Microfabricated devices for capillary electrophoresis-electrospray mass spectrometry. *Analytical Chemistry*, 71 (15), 3258-3264.

Zhou, B.H. & Mahdavian S.M. (2003) Experimental and theoretical analyses of cutting non metallic materials by low power CO_2 laser. *Journal of Materials Processing Technology*, 146, 188-192.